Electrospinning of Ceramic Solid Electrolyte Nanowires for Lithium-Ion Batteries with Enhanced Ionic Conductivity

by

Ting Yang

A Dissertation Presented in Partial Fulfillment
of the Requirements for the Degree
Doctor of Philosophy

Approved November 2016 by the
Graduate Supervisory Committee:

Candace K. Chan, Chair
Peter Crozier
Jerry Y.S. Lin

ARIZONA STATE UNIVERSITY

May 2017

ABSTRACT

Solid electrolytes have great potential to address the safety issues of Li-ion batteries, but better synthesis methods are still required for ceramics electrolytes such as lithium lanthanum titanate (LLTO) and lithium lanthanum zirconate (LLZO). Pellets made from ceramic nanopowders using conventional sintering can be porous due to the agglomeration of nanoparticles (NPs). Electrospinning is a simple and versatile technique for preparing oxide ceramic nanowires (NWs) and was used to prepare electrospun LLTO and LLZO NWs. Pellets prepared from the electrospun LLTO NWs had higher density, less void space, and higher Li^+ conductivity compared to those comprised of LLTO prepared with conventional sol-gel methods, which demonstrated the potential that electrospinning can provide towards improving the properties of sol-gel derived ceramics. Cubic phase LLZO was stabilized at room temperature in the form of electrospun NWs without extrinsic dopants. Bulk LLZO with tetragonal structure was transformed to the cubic phase using particle size reduction via ball milling. Heating conditions that promoted particle coalescence and grain growth induced a transformation from the cubic to tetragonal phase in both types of nanostructured LLZO. Composite polymer solid electrolyte was fabricated using LLZO NWs as the filler and showed an improved ionic conductivity at room temperature. Nuclear magnetic resonance studies show that LLZO NWs partially modify the polymer matrix and create preferential pathways for Li^+ conduction through the modified polymer regions. Doping did not have significant effect on improving the overall conductivity as the interfaces played a predominant role. By comparing fillers with different morphologies and intrinsic conductivities, it was found that both NW morphology and high intrinsic conductivity are desired.

ACKNOWLEDGEMENTS

I would like to thank my advisor, Prof. Candace Chan, for her instructions, and all the Chan group members.

I would like to thank my committee members, Prof. Peter Crozier and Prof. Jerry Lin, for their time and suggestions.

We gratefully acknowledge the use of facilities within the LeRoy Eyring Center for Solid State Science and Goldwater Environmental Laboratory at Arizona State University, and all the staff for their kind assistance. Funding from the National Science Foundation (DMR-1553519) is greatly appreciated.

We gratefully thank Jin Zheng and Prof. Yan-Yan Hu at Florida State University and the National High Magnetic Field Laboratory for performing the NMR measurements and ^{6}Li symmetric cell cycling, as well as the valuable discussion.

I would like to thank all my friends for their help, understanding and encouragement.

Most importantly, I would like to thank my parents for their love and support.

TABLE OF CONTENTS

Page

LIST OF TABLES vi

LIST OF FIGURES vii

CHAPTER

I: BACKGROUND 1

1.1. Introduction 1

1.2. Lithium-ion Batteries 2

1.2.1. Safety Issues with Lithium-ion Batteries 4

1.3. Solid Electrolytes for Lithium-ion Batteries 6

1.3.1. Inorganic Solid Electrolytes 7

1.3.2. Polymer Solid Electrolytes 8

1.3.3. Composite Solid Electrolytes 9

1.3.4. Parameters for Evaluating Solid Electrolytes 9

1.4. One-Dimensional Nanomaterials as Solid Electrolytes 17

1.5. Characterization Techniques 19

1.5.1. X-ray Diffraction 19

1.5.2. Scanning Electron Microscopy 21

1.5.3. Transmission Electron Microscopy 22

1.5.4. Inductively Coupled Plasma Optical Emission Spectrometry 23

1.6. Electrochemical Measurement Technique 23

1.6.1. Electrochemical Impedance Spectroscopy 24

CHAPTER Page

1.7. Electrospinning 28

1.7.1. Electrospinning of Oxide Materials 32

II: ELECTROSPINNING OF LITHIUM LANTHANUM TITANATE 34

2.1. Introduction 34

2.2. Experimental 35

2.2.1. Synthesis of LLTO 35

2.2.2. Materials Characterization 36

2.2.3. Ionic Conductivity Measurements 37

2.3. Results and Discussion 38

2.4. Conclusions 51

III: ELECTROSPINNING OF LITHIUM LANTHANUM ZIRCONATE 53

3.1. Introduction 53

3.2. Experimental 55

3.2.1. Synthesis of LLZO Nanowires 55

3.2.2. Synthesis of Bulk LLZO 56

3.2.3. Materials Characterization 57

3.3. Results and Discussion 57

3.4. Conclusions 73

IV: COMPOSITE POLYMER ELECTROLYTE WITH LLZO NANOWIRE FILLERS 74

4.1. Introduction 74

4.2. Experimental 76

CHAPTER Page

4.2.1. Preparation of LLZO Sol-gel Precursor 76
4.2.2. Electrospinning of LLZO Nanowires 77
4.2.3. Preparation of LLZO Nanoparticles 77
4.2.4. Preparation of Composite Electrolyte....78
4.2.5. Materials Characterization....79
4.2.6. Electrochemical Characterization....79
4.2.7. Galvanostatic Cycling....80
4.2.8. NMR Characterization....80
4.3. Results and Discussion.... 81
4.4. Conclusions.... 97
V: SUMMARY.... 99
REFERENCES 100
APPENDIX
A: PERMISSIONS FROM ALL CO-AUTHORS.... 114
B: LIST OF PUBLICATIONS 116

LIST OF TABLES

Table Page

1. Impedance Analysis Results of Both Conventional Sol-Gel and Electrospun LLTO Samples…….. 45

2. Ionic Conductivities (S/cm) Calculated from Fitted Impedance Data of Two LLTO Samples…….. 46

3. Ionic Conductivity of Different Samples at 20 °C…….. 89

LIST OF FIGURES

Figure Page

1. Schematic of the Brick-Layer Model..... 25
2. (a) Schematic of an Ideal Nyquist Plot for Solid Electrolyte. (b) An Equivalent Circuit of (a)..... 27
3. (a) Equivalent Circuit for a Typical Polycrystalline Sample. (b) Simplified Equivalent Circuit of (a)..... 27
4. Schematic of an Electrospinning Setup 31
5. Electrospinning Setup Used in This Work..... 32
6. Crystal Structure of LLTO..... 35
7. Photographs of (a) As-Spun LLTO NW Mat Being Removed from the Collector, (b) Free-Standing As-Spun LLTO Mat with Good Flexibility. SEM Image of LLTO NWs (c) As-Spun, (d) After Calcination. (e) A Higher Magnification of (d) Showing the NW Surfaces. (f) XRD Pattern of Electrospun LLTO NWs After Calcination with *P*4/*mmm* Tetragonal Structure. 39
8. XRD Pattern with Calculated Pattern from Rietveld Refinement of (a) Electrospun LLTO NWs and (b) Conventional Sol-gel LLTO; (c) XRD Pattern Comparison of Conventional Sol-gel LLTO *vs*. Electrospun LLTO NWs After Calcination. 41
9. TEM Image of Calcined Electrospun LLTO NWs at (a) Low Magnification; (b) High Magnification Showing Individual Grains. Inset Shows the Corresponding SAED Pattern. HRTEM Image of (c) The Lattice Fringes and (d) GB Between Two Grains. The Upper and Lower Inset Shows the FFT of the Upper and Lower Grain, Respectively..... 42

Figure Page

10. Nyquist Plots of LLTO Pellets Derived from Conventional Sol-gel *vs*. Electrospun NWs, Normalized by Pellet Thickness in the (a) High Frequency Range and (b) Full Frequency Range with Fitted Curves; Inset Shows the Equivalent Circuit Used for Fitting. 44

11. (a) SEM Image of Bulk LLZO Powder. (b) SEM Image of the Same Powder in (a) After Being Ball Milled. 49

12. Schematic Showing Agglomeration in NPs 49

13. Schematic Showing the Pellet Making Process with Different Starting Morphologies 50

14. Cross-sectional SEM Image of Pellet Made of (a) Conventional Sol-gel LLTO and (b) Electrospun LLTO. 50

15. Crystal Structure of (a) Cubic Phase LLZO and (b) Tetragonal Phase LLZO 55

16. SEM Image of (a) As-spun LLZO NWs and the NWs After Calcination at 700 °C for (b) 1.5 h, (c) 2 h, (d) 2.5 h, (e) 3 h, (f) & (g) 5 h. (h) XRD Patterns Showing the Effect of Calcination Time on the Product. ●: Unidentified Intermediate Phase; *: $La_2Zr_2O_7$; Light Blue: c-LLZO Phase; Dark Blue: Mixture of Tetragonal + Cubic LLZO Phases. (i) Zoom-in of XRD Patterns Around 31°, Showing the Emergence of Peak Doublet During Heating from 2.5 h to 5 h. 59

Figure Page

17. LLZO NWs from Nitrate-based Precursor. (a) Photograph of an As-spun LLZO Fiber Mat. (b) SEM Image of As-spun LLZO NWs. (c) SEM Image of LLZO NWs After 3 h of Calcination at 700 °C. (d) XRD Patterns of LLZO NWs Calcined in Alumina and Quartz Crucibles, Matching the HT-cubic LLZO Phase Shown as Reference. (●: La_2O_3; *: $La_2Zr_2O_7$) 60

18. (a) TEM Image of the Acetate-based NWs Calcined for 2.5 h, Showing One of the Morphologies. Inset Is a Zoomed-in View Showing the $La_2Zr_2O_7$ Crystals. (b) TEM Image of One Branch in (a) Areas Indicated by Arrows Are Considered to Be a Li-containing Amorphous Phase. Inset Is an HRTEM Image Showing the Lattice Fringes. (c) TEM Image of the Same Sample Calcined for 2.5 h, Showing the Other Morphology (LLZO Crystals). Inset Shows the HRTEM Image with Lattice Fringes. 62

19. XRD Pattern of Bulk LLZO Calcined at 700 °C for 3 h, Showing a Mixture of Cubic and Tetragonal LLZO. (●: La_2O_3) 64

20. XRD Pattern of c-LLZO Derived from Electrospun NWs After 14-month Storage.. 67

21. XRD Patterns of Bulk LLZO Prepared from Nitrate-based Sol-gel (a) After Calcining at 700 °C for 5 h, (b) After Ball Milling, (c) After 4-month Storage, (d) After Annealing at 700 °C for 12 h. The Bulk LLZO Changed from Tetragonal to Cubic after Ball Milling with the Re-emergence of t-LLZO After Heating. Tetragonal Peak Doublets Are Marked with Arrows. (Dark Blue: t-LLZO; Light Blue: c-LLZO; ●: La_2O_3; *: Artifact Peaks from Instrument) 67

22. EDS Spectrum Obtained in an SEM of the c-LLZO NW Sample..... 68

Figure Page

23. Schematic of EIS Measurement in Oven 80

24. (a)-(h): SEM Images of Electrospun NWs. All Calcinations Were Performed at 700 °C (a) As-spun NWs. (b) c-LLZO NWs Prepared Using Water-based Precursor and Calcined for 3 h. (c)-(h): c-LLZO NWs Prepared Using DMF-based Precursor and Calcined for (c),(e),(g) 1 h or (d),(f),(h) 3 h. (c)-(d): Undoped LLZO; (e)-(f): Al-LLZO; (g)-(h): Ta-LLZO. (i) TEM Image and (j) HRTEM Image of Undoped c-LLZO NWs Prepared from DMF-based Precursor and Calcined for 1 h. Inset Is the Corresponding SAED Pattern. 83

25. (a) Diameter Distribution of the 1 h Calcined Undoped LLZO NWs. EDS Spectra of (b) Al-LLZO and (c) Ta-LLZO, Both Calcined at 700 °C for 1 h. 84

26. XRD Patterns of LLZO NW Samples After Calcination for (a) 1 h and (b) 3 h at 700 °C; (c) Zoomed-in Patterns at the Region Around 52°. (*: $La_2Zr_2O_7$; ●: La_2O_3)..... 85

27. (a) SEM Image (Top-down View) of a CPE Film with 5 wt% Undoped LLZO NWs. (b) Schematic of the EIS Test Setup. (c) Equivalent Circuit Used for EIS Data Fitting. (d) Representative Nyquist Plots of CPEs Embedded with 5 wt% of Different Filler Materials, All Tested at 20 °C and Normalized by Film Thickness. (e) Zoomed-in View of the Region Marked by Dashed Lines in (d). (f) Ionic Conductivity Comparison of CPEs Embedded with Different wt% of Undoped LLZO NWs at 20 °C, with the Conductivity of a Blank Sample for Reference. Each Point is the Average of Three Measurements and the Error Bars Indicate the Standard Deviation. (g) Arrhenius Plot of CPE with 5 wt% Undoped LLZO NWs. Each Point is the Average of Two Measurements. 87

Figure Page

28. (a) Nyquist Plot of a Blank Sample Composed of 66.7 wt% PAN and 33.3 wt% $LiClO_4$, Tested at 20 °C. (b) Nyquist Plots of CPEs Embedded with Different wt% of Undoped LLZO NWs, Tested at 20 °C and Normalized by Film Thickness. (c) Nyquist Plots of Samples Embedded with 5 wt% Undoped LLZO NWs, Tested at Different Temperatures and Normalized by Film Thickness. Inset Shows a Zoomed-in View of the Region Marked by Dashed Lines. 88

29. Bulk Undoped LLZO After Ball Milling (BM-LLZO NPs): (a) SEM Image; (b) XRD Patterns with c-LLZO Reference. The LLZO Adopted the c-LLZO Structure After Ball Milling and Could Maintain this Structure Even After 4-month Storage. (*: Artifact Peaks from Instrument) 90

30. (a) Schematic Showing Possible Li^+ Transport Pathways in the CPE. (b) ^6Li NMR Spectra of CPE Sample Containing 5 wt% Undoped LLZO NWs, Blank Sample with Only PAN and $LiClO_4$, and Undoped LLZO NW Powder. (c) ^6Li NMR Spectra Comparison Between the As-made (Pristine) and Cycled CPEs Containing 5 wt% Undoped LLZO NWs. The Cycled CPE Had Undergone 10 Galvanostatic Charge/discharge Cycles in a Symmetric ^6Li Cell Using 7.2 $\mu A/cm^2$ 93

31. Galvanostatic Cycling Data of a Symmetric ^6Li Foil/CPE/^6Li foil Cell. The Area of ^6Li Electrodes Is 1.5386 cm^2. The CPE Contains 5 wt% Undoped LLZO NWs. 93

32. XRD Patterns of Blank Sample (PAN with 33.3 wt% $LiClO_4$) and CPE Containing 5 wt% Undoped LLZO NWs, with c-LLZO for Reference. (*: Artifact Peaks from Instrument) 95

Figure Page

33. (a) Li Symmetric Cell Galvanostatic Cycling Data of a CPE Sample Containing 5 wt% Undoped LLZO NWs. (b) The Tail Region of (a), Showing the Sudden Voltage Drop. (c) Li Symmetric Cell Galvanostatic Cycling Data of a Blank Sample. (d) The Tail Region of (c), Showing the Sudden Voltage Drop. 97

34. Galvanostatic Cycling Data of a Blank Sample (PAN with 33.3 wt% $LiClO_4$), Showing the Cell Voltage and Current. 97

I: BACKGROUND

1.1. Introduction

Electrical energy can be stored in many forms, such as mechanical, chemical, thermal, nuclear, *etc*. In modern society, there has been a booming development and popularity of portable electronics, and a rising trend for device miniaturization, posing a high demand on batteries, which is the chemically stored form of electrical energy. Laptop computers, cell phones, smart watches, Bluetooth devices… almost every gadget is powered by batteries. Even for motor vehicles that are propelled by internal combustion engines, batteries are needed to start the engine and to maintain the operation of various electronic circuits within, and lead-acid batteries are still the dominant type being used. Not to mention the growing production of all-electric cars, which drive entirely on batteries. Technically speaking, cells are the building blocks of batteries, and a battery is made by stacking two or more cells together, which is also why this device is called a 'battery'. A cell has three fundamental components: anode, cathode and electrolyte. The materials chosen for the anode and cathode (the two electrodes) have the property such that when they are in contact, a reduction-oxidation (redox) reaction will take place spontaneously between them. In a redox reaction, the anode material is oxidized, giving away electrons, and the cathode material accepts these electrons and becomes reduced. However, by doing that alone does not provide us with electricity, as all the electrons in the materials participated directly in the redox reaction. But if the two electrodes are separated by a medium in which only ions can move across (electronically insulating), and another electron-only connection is established between the two

electrodes, then the flow of electrons can be extracted and used by an external circuit, *i.e.* chemical energy is converted to electrical energy. Such a medium is called the electrolyte, which serves as an ion reservoir, ensuring charge balance and supplying reaction species. When the cell is not in use, the two electrodes should be electronically disconnected to prevent power dissipation.

Batteries are categorized into primary batteries and secondary batteries. Primary batteries are of single-use and cannot be recharged after all the chemically stored energy is depleted. Secondary batteries are also called rechargeable batteries, which means that their charged state can be restored. This is done by selecting appropriate material combinations with reversible redox reactions. To recharge the battery, an electrical bias (voltage) is applied between the two electrodes, providing sufficient electrochemical potential and electrons to reverse the redox reaction until the initial state is reached. It should be pointed out that a good number of the redox reactions in the primary batteries can actually be reversed as well. But doing that is either too expensive, or practically not feasible. Among all the commercially available rechargeable batteries, our research is focused on the electrolyte materials for lithium-ion batteries.

1.2. Lithium-ion Batteries

Lithium is the lightest metal and exhibits the highest oxidation potential, which makes it an ideal material for batteries with the highest energy density.[1] In 1976, Whittingham reported the intercalation chemistry of lithium into a layered compound (TiS_2) and conceived a new type of reversible battery with high energy density[2]. Because lithium metal was used as the anode, this type of battery can only be called a lithium

(metal) battery, but it nonetheless laid the very foundation for the development of lithium-ion batteries. However, it was found out later that upon charging, lithium was essentially being electrodepositing onto the anode non-uniformly, resulting in the formation of lithium dendrites.[3] The dendrites could keep growing after each charge-discharge cycle, and at some point they could pierce through the separator (an electronically insulating but ionically conducting material), putting the cathode and anode in direct electrical contact and causing a short circuit to the battery. As the name suggests, a short circuit means that it is the 'shortest' path for the electric current (electrons) to run through. Therefore, the battery would discharge with a large current, generating a large amount of heat due to Joule heating. This is extremely dangerous as the organic liquid electrolyte and lithium metal in the battery are highly flammable, which could lead to fire or even explosion.

It was discovered later that graphite, which is also a material with layered structure, could also act as a host for Li^+ intercalation.[4] This means that the highly reactive lithium metal can be replaced by graphite, leaving only Li^+ in the system to 'rock' back and forth between the two electrodes. This type of battery is called a lithium-ion batteries, and hence the term 'rocking chair' batteries. After that, some layered oxide materials (*e.g.* $LiCoO_2$) were also found to have intercalation chemistry, and much higher operation voltage (electrochemical potential) than sulfides when used as the cathode, allowing for higher energy density to be achieved.[5,6] In 1991, Sony released the first commercial lithium-ion battery, using graphite anode and $LiCoO_2$ cathode.[7] Nowadays, a typical commercial lithium-ion battery still uses graphite as the anode, and lithium transition metal oxides as the cathode. The most commonly used electrolyte is 1 M $LiPF_6$

dissolved in a mixture of ethylene carbonate (EC, $C_3H_4O_3$) and diethyl carbonate (DEC, $C_5H_{10}O_3$). The separator, usually a porous polymeric material, is placed in the electrolyte between the anode and cathode. As mentioned earlier, the purpose of this separator is to prevent short circuits caused by electrical contact between the two electrodes, while allowing ions to pass through.[8] Because of its light weight and high energy density, the lithium-ion battery has become the prevailing battery type on the market, thanks to the fast development and popularization of portable electronic devices. Most consumer electronic devices today, such as cell phones, laptop computers, personal medical devices, *etc*., are powered by lithium-ion batteries. Modern electric and hybrid vehicles also utilize lithium-ion batteries as their primary source of energy.

1.2.1. Safety Issues with Lithium-ion Batteries

Although the lithium-ion battery has so many advantages and applications, some inherent safety issues associated with the current design and material selection have already caused a series of accidents. The two organic solvents (EC and DEC) used in the liquid electrolyte are highly flammable by themselves, and their mixture has a flash point lower than 30 °C.[9,10] The flash point is the lowest temperature at which the vapor of a flammable liquid can ignite in air. 30 °C is merely above room temperature, not to mention that the device will heat up to even higher temperature during operation. As the temperature rises, the internal vapor pressure builds up, sometimes causing the battery to swell or bulge. When the battery's external casing is no longer able to hold the pressure, it will be ruptured and release the flammable gases. These high-temperature gases, upon contact with air, can then catch fire and the whole battery will burn, or even explode in

some extreme cases. Another common fire hazard is a short circuit in the battery, which is usually due to the failure of the separator. As already mentioned, short circuits generate a large amount of heat, which accelerates the exothermic chemical reactions and generates even more heat. This process is called thermal runaway and is analogous to a chain reaction. Separator failure is typically caused by mechanical damage. For example, if the battery is overcharged, lithium dendritic growth can take place, and continues as the battery cycles, eventually breaching the separator. In some rare cases, the quality control of the battery manufacturing is poor and some hard particles are accidentally introduced into the battery, which can also puncture the separator after a certain number of cycles as the battery expands and shrinks. Overheating is another major cause of separator failure, which either softens the separator so that its mechanical strength is reduced and the lithium dendrites take less effort to break through, or causes deformation of the separator to widen some pores, providing extra room for the dendrites to grow.

According to the U.S. Consumer Product Safety Commission, almost all major computer companies, especially Dell and HP, have recalled millions of laptop computer batteries due to fire and burn hazard. In 2006, Sony recalled over 7 million defective batteries that could lead to sudden ignition.[11] Tesla Motor's all-electric cars, which use standard 18650 lithium-ion cells in the battery pack, have encountered multiple fire accidents after running over debris.[12] In 2013, the entire Boeing 787 Dreamliner fleet was grounded due to problems caused by lithium-ion battery thermal runaway in the electrical system.[13] On October 10 2016, Samsung recalled all of its Galaxy Note7 cell phones due to potential overheating and fire risk of the phone's lithium-ion battery, which was less than two months from the release date.[14] Numerous (more than 40) incidents of phones

catching fire or even exploding were reported during that short period of time. Preliminary investigations stated that the phone's battery was faulty and caused the insulation to fail, resulting in a short circuit and consequently rapid heating. Approximately one million sold devices were affected, while about 2.5 million were manufactured. All these incidents are pointing to the same demand – a safer design and material selection for safer lithium-ion batteries.

1.3. Solid Electrolytes for Lithium-ion Batteries

There are many different approaches to deal with the flammability problem for liquid electrolytes, but none of them can completely solve it so far. For instance, adding flame retardant additives into the liquid electrolyte can make it less vulnerable to catching fire, but often the performance is compromised as a trade-off. The viscosity of the liquid electrolyte can be increased to lower the ion transfer speed, and hence the current density is decreased in the external circuit to reduce heating, but this also means less overall power. The electrochemical instability of the additives may also cause the capacity to fade.[10] Alternatively, this issue can be addressed by replacing the liquid electrolyte with solid electrolyte, forming an all-solid-state battery.

Compared to liquid electrolytes, solid electrolytes generally offer reduced flammability, better thermal and mechanical stability, and broader electrochemical window. Additionally, most of them are electronic insulators, eliminating the need for a separator.[15–17] However, solid electrolytes typically suffer from low room temperature ionic conductivity, which is an inherent issue due to the nature of solid-state ionic motion. In order to be usable practically, the ionic conductivity of solid electrolytes have to be

comparable to that of the liquid electrolytes (~10^{-2} S/cm)[18], or at least on the order of 10^{-3} S/cm.[15] This criterion narrows the material selection down to a small number of candidates, which will be briefly discussed in the following sections. Solid electrolytes can be classified into inorganic solid electrolytes, polymer solid electrolytes and composite solid electrolytes.[17,19,20]

1.3.1. Inorganic Solid Electrolytes

Inorganic solid electrolytes generally have better mechanical and thermal stability over organic (polymer-based) electrolytes.[21] Also, since many of them are electronic insulators, they have the potential to completely eliminate the need for a separator, and hence lower the total cost of batteries as the separator's cost contributes nearly 25%.[22,23] Nevertheless, there are still drawbacks with inorganic solid electrolyte materials, such as low room temperature conductivity, and energy-consuming synthesis or processing conditions. For example, the ionic conductivity of solid electrolytes is usually in the range of 10^{-6} to 10^{-3} S/cm at room temperature.[9] Some materials, especially oxides, require high temperature synthesis, and some other materials need vacuum deposition techniques. A number of different material classes have been studied, including sulfides, oxides, oxynitrides (*e.g.* lithium phosphorus oxynitride, LIPON), NASICON-type phosphates (Na Super Ionic CONductor) and LISICON-type materials (Li Super Ionic CONductor).[24,25] Among these materials, sulfides do not have very good chemical stability, LIPON suffers from low room temperature ionic conductivity, NASICON-type materials have good conductivity but are unstable against Li, and LISICON-type materials have both low conductivity and stability.[19] Some oxides, on the other hand,

either have exceptional room temperature conductivity, or are stable by themselves and/or against Li.[26] In this work, two oxide materials are of particular interest to us: lithium lanthanum titanate (LLTO) and lithium lanthanum zirconate (LLZO). Detailed studies will be presented in the following chapters.

1.3.2. Polymer Solid Electrolytes

For pure solid polymer electrolytes, their room temperature ionic conductivity is too low (~10^{-6} S/cm) for practical use.[27] The first reported polymer electrolytes with reasonably high ionic conductivity were some polyethylene oxide (PEO) systems by Wright *et al*.[28] Later it was found that the addition of certain salts could amorphize some polymers and form complexes, which helped promote the delocalization/dissociation of the ions in the salts.[29] The ions, especially the anions, then had more freedom to be carried around by the segmental motion of the polymer chains. It was also discovered that the amorphous regions in the polymer are actually contributing to ionic conduction.[30] A general material selection criterion is that the salt should have low lattice energy, and the polymer should have high dielectric constant.[31] Up till today, different systems with a variety of polymer and salt combinations have been identified with satisfactory room temperature ionic conductivity. The PEO-based systems are the most studied and therefore are usually used as a model. Among all the polymer solid electrolytes, there is one type that is of particular interest to us, which is the composite polymer solid electrolyte. Sometimes another type of polymer electrolyte, called a gel electrolyte, is counted as a polymer solid electrolyte; gel electrolytes are, essentially polymer soaked with organic liquid electrolyte.[29,31] Although significantly reduced compared to a battery

using solely liquid electrolyte, the amount of liquid electrolyte in the system is still substantial and therefore the flammability problem is not fully addressed.

1.3.3. Composite Solid Electrolytes

Generally speaking, electrolytes that utilize two or more different types of materials can all be categorized as composite electrolytes. Composite polymer electrolyte is the most widely studied type of solid electrolyte, which is typically composed of a polymer matrix and a small amount of inorganic solid particles as the filler, or in other words, inorganic particles embedded in a polymer solid electrolyte.[32,33] Sometimes when ceramic NPs are used, it is also termed as the 'nanocomposite polymer electrolyte'. The overall ionic conductivity of the polymer matrix can be greatly improved (up to several orders of magnitude) by dispersing a certain amount of ceramic NPs within the matrix. The exact mechanism of this drastic increase in conductivity is still unclear, but it is widely accepted that the presence of NPs interfered with the crystallization of the polymer matrix, *i.e.* the crystallinity of the matrix is reduced.[29,34,35] This is understandable because those particles can inhibit the ordering and/or aligning of polymer chains, creating amorphous regions around themselves. Another popular theory is that each ceramic particle acts as a Lewis acid/base center, which helps promote the dissociation of Li^+ from the lithium salt, generating more 'free' Li^+ and hence increasing the ionic conductivity.[34,36–39] This will be discussed in more detail in Chapter III.

1.3.4. Parameters for Evaluating Solid Electrolytes

1.3.4.1. Conductivity and Ionic Transport

In solid electrolytes, the conductivity consists of two components: electronic conductivity and ionic conductivity.[40] Since the aim is to replace both the liquid electrolyte and the separator by solid electrolyte, the material needs to have negligible electronic conductivity in order to prevent the cell from shorting. Therefore, solid electrolyte materials are ideally electronic insulators. The ionic conductivity, usually expressed as σ, is one of the most important properties for evaluating solid electrolyte materials. The overall/total ionic conductivity is the resultant of all the conduction mechanisms taking place within the material. For inorganic solid electrolytes, the two major contributions to the total ionic conductivity are conduction through the bulk (grain volume) and through the grain boundaries (GBs).[17,19,41,42] The bulk conduction is intragranular, meaning that it concerns how ions move within a grain. In ceramics, for example, atoms are bonded together by strong covalent bonds, making it difficult to free an ion by breaking bonds, and to move it all the way across the entire grain. Rather, ionic conduction in ceramics depends on a short-range process called 'hopping'. No material is perfect, and so there are always some defects in the structure, including vacancies. Vacancies are high-energy sites, which makes it energetically more favorable for Li^+ to 'hop' to the nearest vacancy, than to travel from one end of the grain to the other. Because the bonding strength, the structural configuration and the chemical environment *etc*. of Li^+ are governed by the types of material, and therefore the bulk ionic conductivity is mainly a material property. The GB conduction is intergranular, in which Li^+ have to travel from across the GB between adjacent grains. One could image that this process would be energy-demanding and requires physical contact between grains. This GB conductivity can be improved by means of increasing the contact area between grains,

such as eliminating pores and gaps, applying external pressure, or using better preparation methods. The total ionic conductivity can be calculated by the relationship

$$\frac{1}{\sigma_{\text{Total}}} = \frac{1}{\sigma_{\text{Bulk}}} + \frac{1}{\sigma_{\text{GB}}} \quad (1)$$

where σ_{Bulk} and σ_{GB} represent the contribution from bulk and GBs, respectively. Detailed explanation of how this relationship is established, and how to extract information from experimental results to calculate these values, will be given in Section 1.6. It can be seen in Equation (1) that the order of magnitude of σ_{Total} is determined by the smallest value in the individual contributions since it is a reciprocal sum. Therefore, it is necessary to improve both σ_{Bulk} and σ_{GB} in order to achieve a σ_{Total} high enough for practical applications. The best total ionic conductivity one can get from all the ceramic solid electrolytes so far is in the range of 10^{-4}–10^{-3} S/cm at room temperature.[16,17,19,26,41,42]

In composite polymer solid electrolytes, the scenario is more complex and not well-understood. For pure polymers, as mentioned earlier, ionic conduction happens primarily through the amorphous regions[43], and more specifically, through the polymer backbone segmental motions,[44] with surface groups also participating in conduction.[43,45] With the addition of ceramic particles, the list of conduction processes goes even longer. Similar to pure ceramic solid electrolytes, intragranular and intergranular conductions can take place in the particles. At the same time, conduction along and across the polymer/ceramic interface, conduction of dissociated ions generated by the presence of ceramic particles, so on and so forth, can all be taking place. Although a lot of the times, it is nearly impossible to separate out and distinguish the contribution from every conduction mechanism, the total ionic conductivity is still the most important.

Another important parameter is the ion transference number, or ion transport number. The transference number of a given ion species is defined as the proportion of the total electric current that is carried by that specific ion in the electrolyte, and the sum of the transference number of all ions in one system should be unity.[15] Ideally, for applications in lithium-ion batteries, the transference number for Li^+ should be 1, or very close to it. It means that the current in the battery is completely (or mostly) due to the motion of Li^+, which is desired for maximum efficiency, because only Li^+ can participate in the intercalation-disintercalation reactions.[20] For inorganic solid electrolyte materials this is usually not an issue, but for the majority of polymer-based solid electrolytes, the transference number can only reach ~0.5,[29] which calls for further improvement. However, some composite polymer solid electrolytes are an exception because the selection of salt and polymer can be carefully tailored so that Li^+ is only cation in the system, and the anion(s) are trapped or immobilized by the polymer backbone, and hence the transference number can approach unity.[17]

1.3.4.2. Interfaces

Within a cell, there are a number of different interfaces that are of importance to the overall performance, namely, the interface between ceramic solid electrolyte particles (for ceramic electrolytes), the interface between the polymer matrix and the ceramic fillers (for composite electrolytes), and the interface between the solid electrolyte and the electrodes. In all-solid-state cells, the contact between solid materials has been one of the major problems faced by researchers.[46,47] Unlike the liquid/solid interface in a commercial cell, the solid/solid contact is very poor, and can even be considered the

limiting step to overall performance. The quality of interface generally depends on the area that is in contact – more contacting area means a better interface. In the case of contact between solids, surface roughness and the presence of external compressive forces are two major factors dictating the amount of contact area. A rough surface increases the exposed area, but contact can still be bad if the surface pattern/texture does not match that of the other surface. Pressing two materials against each other help improve the contact most of the time, but the magnitude of the force needs to be carefully controlled to prevent the solids from cracking. Another issue with applying a compressive force to a cell is that, since the force is uniaxial in most cases, only a fraction of the surfaces, especially those that are perpendicular to the force direction, can benefit from it. Surfaces that are parallel to the force direction usually will not be affected. By using some bottom-up growth techniques, *e.g.* sol-gel or other deposition methods, the materials can be directly grown onto another solid surface to produce a uniform interface with good contact. Taking the sol-gel method as an example, it can benefit from the liquid/solid interface when the liquid phase is in contact with the solid phase. The sol/gel is then processed to remove the solvents, so the material can use the surface of the solid as nucleation sites.[48] Since the grains grow directly on the solid, the interfaces tend to have low energy, and thus adhesion is considered to be improved. Another example would be epitaxial growth, in which the material crystallizes with the same lattice orientation (lattice match) as the substrate because that is the orientation with the lowest energy.

For composite polymer solid electrolytes, the interface between the polymer matrix and the ceramic filler particles is usually considered to be better than that in

ceramic solid electrolytes. This is because that the fabrication of such composite electrolytes starts from the solution of the polymer matrix material in most cases. Ceramic fillers are dispersed into the solution, which is then cast to form a thin film, and dried by removing the organic solvents. It is still unclear, however, what is exactly happening at the interfaces due to the complexity of the system. Recently, Zheng *et al*.[49] studied the Li^+ pathways in PEO-LLZO system by replacing ^7Li with ^6Li, and found that conduction was more favored within the LLZO particles than at the PEO/LLZO interface. It shed some light on how the conduction processes can be probed for the composite system.

The quality of the interface can be quantitatively evaluated by the resistance/impedance associated with it, or sometimes capacitance, too. A low value in these properties means a good interface. But a lot of the times, due to the complexity of the system, or the limit of the measuring technique, it is very difficult or even impossible to distinguish/extract the interfacial component from the experimental data. In that case, the overall or averaged value is used to approximate the order of magnitude of the actual one.

1.3.4.3. Stability

The stability of the solid electrolyte materials includes chemical, physical and electrochemical stabilities.[50] The material needs to be chemically stable during synthesis, fabrication and normal operation. Although air exposure is a very unlikely event under normal operation conditions, it is still desirable to test the air stability (against oxygen and moisture). Sometimes carbon dioxide (CO_2) can be harmful to the material as well,

and therefore should also be looked at. In terms of physical stabilities, a series of mechanical properties can be tested, including elastic moduli (*e.g.* Young's modulus, shear modulus), hardness and fracture toughness. Shear modulus is crucial to all types of solid electrolytes since a large modulus (> 8.5 GPa) can in theory suppress Li dendrite formation.[51] For ceramic solid electrolytes, the fracture toughness is especially important because ceramics are brittle materials, and cracks tend to form due to the calcination-cooling cycles, or shocks during handling. The Young's modulus should be studied on polymer-based solid electrolytes when bending is required in the application.

Electrochemical stability means that the electrolyte must remain stable across the operation voltage window of the battery. The material should not decompose, or take part in any unwanted side reactions. In order to have an energy density as high as possible for lithium-ion batteries, materials with high electrochemical potentials are preferred as the cathode, as mentioned earlier. The problem with this is that, by increasing the working voltage of the battery, the energy density is improved, but the electrolyte is also polarized by a high voltage at the same time. In conventional lithium-ion batteries, this can cause the organic liquid electrolyte to be oxidized at the cathode, and reduced at the anode, forming a layer termed the 'electrode-electrolyte interface' (EEI) or 'solid-electrolyte interphase' (SEI) on each electrode. This EEI layer does not contribute to the total battery capacity; on the contrary, it consumes a small amount of energy to form upon the initial cycle. On the other hand, it acts as a passivating layer that prevents further reaction between the electrode and the electrolyte, while still allowing Li^+ to go through, and hence ensuring safety, long cycle life, high Coulombic efficiency and high voltage efficiency.[52] Therefore, in polymer-based solid electrolytes, the formation of EEI must be

assessed. For inorganic solid electrolytes, due to the absence of organic components and the relatively high dielectric constant of ceramics, EEI is usually considered non-existing and the materials can withstand higher voltages. However, a recent study[49] showed that at the $LiCoO_2$/LLZO interface, a very thin layer of EEI would form if the two materials were in direct contact, which negatively affected the electrochemical performance. This suggests that EEI formation might have been overlooked for inorganic solid electrolytes and therefore should also be carefully examined.

Thermal stability, apart from non-flammability, is still very important because the reactions inside the battery are quite exothermic, not to mention that batteries are usually located in a constricted space within the device where ventilation or any type of heat dissipation is extremely poor and lacking, which can result in localized high temperatures. This is especially true in polymer-based systems as organic materials are not known for withstanding too high of a temperature, so melting and/or thermal decomposition can happen, which can cause degradation of the performance, or even catastrophic failure. Moreover, the added salts (*e.g.* $LiClO_4$) can be highly reactive and problematic. For most oxide-based ceramic solid electrolyte materials, they are completely immune to those issues because of their refractory nature. However, another aspect of thermal stability is required, which is the resistance to thermal shocks. Thermal shocks are rapid temperature changes, and ceramics are brittle materials that are prone to cracking under thermal shocks. Therefore, the tolerance of rapid thermal expansion/contraction should also be an important parameter when evaluating candidate materials.

1.3.4.4. Activation Energy

The concept of activation energy was first introduced by Svante Arrhenius in 1889. It is the minimum energy required to initiate a process (chemical reaction). Ionic conduction in solid electrolytes is considered to be an activation process, which follows the Arrhenius equation (relationship)

$$\sigma(T) = A\exp(-\frac{E_a}{RT}) \tag{2}$$

where σ is the ionic conductivity, T is the temperature in Kelvin, A is a pre-exponential factor, E_a is the activation energy and R is the universal gas constant. A lower activation energy means that the reaction is easier to take place, and therefore is desired for all solid electrolytes. We can re-arrange the Arrhenius equation to get a new relationship:

$$\log\sigma = -\frac{E_a}{RT} + \log A \tag{3}$$

If a plot of $\log\sigma$ *vs*. $\frac{1}{T}$ is drawn, then it will be a straight line with a slope of $-\frac{E_a}{R}$ and an intercept of $\log A$. Therefore, to measure the activation energy, a common practice is to measure the ionic conductivity at various temperatures, and then make a $\log\sigma$ *vs*. $\frac{1}{T}$ plot to calculate the slope.

1.4. One-Dimensional Nanomaterials as Solid Electrolytes

When materials reach the sub-micron regime, especially tens of nanometers in size, their properties become significantly different from the bulk ones. This is because bulk properties are essentially the average or overall behavior of all atoms within the

material. When the particle size is reduced, fewer and fewer atoms are left within the material, and eventually the behavior of individual atoms becomes more dominant than the overall effect. For instance, the NPs of some materials show different colors than their bulk forms because factors like quantum confinement[53,54] and surface plasmon resonance[55] come into play. In terms of mechanical properties, metals are generally considered to be 'soft', as they are ductile and malleable, which is due to the fact that atoms can 'slide' over each other when in bulk. However, inside metal NPs, these large-scale 'slidings' are no longer present, and the relative density of dislocations and stacking fault are largely increased. As a consequence, the metal becomes a very hard material.[56] Other properties such as electrical, optical, chemical, magnetic, *etc*., can all exhibit very interesting changes as the particle size is reduced. This is also why nanomaterials and nanostructured materials have been attracting researchers' attention for many years.

When used as solid electrolytes in lithium-ion batteries, nanomaterials can also be advantageous in different aspects.[57] For example, nanocrystalline solid electrolytes have been shown to display higher ionic conductivities than their bulk single crystal forms.[58,59] Recent studies have also shown improved properties when nanosized solid electrolyte is used compared to bulk materials, such as higher ionic conductivity,[60] cycling performance and current density,[47] and fracture strength.[61] Among the different forms of nanomaterials, one-dimensional (1D) nanostructures, *e.g*. nanowires (NWs), nanorods and nanotubes, are of particular interest to us. A common point to all 1D nanostructures is that their radial dimension (*i.e*. diameter) is on the nanometer scale, but the axial length is orders of magnitude higher. Such high aspect ratio can have multiple advantages on the material properties. For example, transport across the diameter, whether it is mass,

electron or heat, can benefit from the short distance. While on the other hand, processes that happen along the length are highly directional, meaning that they can be made very selective or controllable. A pertinent example would be that researchers have made electrodes with different types of NWs and nanoribbons and demonstrated significant improvement in performance,[62–65] which is a direct result of the unique morphology and properties of 1D nanomaterials. Electrospun LLTO NWs were used as fillers in a polyacrylonitrile-$LiClO_4$ polymer complex to make a composite solid electrolyte and achieved a room temperature ionic conductivity of 2.4×10^{-4} S/cm.[45] Electrospun LLZO NWs were also embedded as a filler network in a PEO-LiTFSI (lithium bis(trifluoromethane)sulfonimide salt) complex and demonstrated an ionic conductivity of 2.5×10^{-4} S/cm at room temperature.[66]

1.5. Characterization Techniques

1.5.1. X-ray Diffraction

X-ray diffraction (XRD) is a very useful and straightforward technique for identifying phases in crystalline samples, as well as revealing crystallographic information. It is based on the fact that the wavelength of X-rays is comparable to the interatomic spacing of solid materials, so diffraction will happen when the incident X-ray beam hits the sample, and scattered X-rays are collected by the detector. The fundamental relationship governing the diffraction behavior is described by Bragg's Law

$$n\lambda = 2d\sin\theta \quad (4)$$

where n is an integer, λ is the wavelength of the incident X-ray, d is the interplanar lattice spacing and θ is the incident angle. A simple explanation of this formula is that, for a set of planes with a fixed d, the incident beam is diffracted by a fixed angle (2θ), provided that λ is kept unchanged. It means that, for crystalline samples, because of the presence of long range order, all beams diffracted from a specific set of planes will point to the same direction and hence can produce distinct and strong signals when they interfere with each other constructively. When these signals are plotted on a signal intensity *vs*. angle diagram, they appear as sharp peaks (high intensities), and this plot is called an XRD pattern. For amorphous materials, or the amorphous part within the materials, the incident beams are scattered to all possible directions due to the lack of long range order. Therefore, only a very broad 'hump' is obtained, which is termed the amorphous halo.

All XRD analyses in this work were performed using a PANalytical X'Pert Pro high resolution X-ray diffractometer. The X-ray used was CuK_α radiation with λ = 1.541874 Å. Sample powders were held by a zero background substrate during measurement. Sometimes double-sided tape was used to hold the sample in place. The pattern of the tape is mostly low-intensity and amorphous, with some very broad peaks at low angles. This means that the presence of tape does not interfere with crystalline samples, and its contribution to the overall pattern can be simply subtracted. For polymer film samples, they are placed directly onto the zero background substrate without any adhesives.

1.5.2. Scanning Electron Microscopy

Scanning electron microscopy (SEM) is a commonly used technique for examining sample morphology. In an SEM machine, electrons are generated from the emission gun under high voltage, and are focused into a beam by electromagnetic lenses onto the sample. As the incident electrons bombard the sample, some electrons in the sample are knocked off from their orbitals within the atoms and become the secondary electrons, while some incident electrons are deflected backwards and become the back-scattered electrons. These two types of electrons are collected to image the sample as the beam scans across it. Secondary electrons are useful in showing the sample topography, while back-scattered electrons carry information about the mass of the atoms in the sample. The SEM facility used in this work is an XL30 Environmental FEG, which is also equipped with the EDAX system, capable of doing energy-dispersive X-ray spectroscopy (EDS or EDX). Upon the bombardment of the incident beam, electrons on the inner shell of an atom in the sample are excited and ejected, then electrons from a higher energy shell fall back to fill the vacancies, emitting X-rays at the same time. The energy of the X-rays is equal to the energy difference between the two shells. Because the energy of each shell is quantized and specific for each element, the emitted X-rays are called ‘characteristic X-rays’ and can be used for elemental identification and compositional analysis. For SEM specimen preparation, sample powders were dispersed in isopropanol through sonication. Droplets of the resulting suspension were then deposited onto a substrate till the isopropanol dries out. For bulk samples, such as electrospun fiber mats or polymer films, they can be directly loaded onto the holder using

a double-sided carbon tape. Sometimes a very thin layer of gold (~10 nm) was sputtered onto the specimen to improve electronic conductivity for better image quality.

1.5.3. Transmission Electron Microscopy

As the name suggests, transmission electron microscopy (TEM) collects transmitted electrons, rather than secondary or back-scattered electrons, to obtain information. High energy electrons have very short wavelengths, and therefore they are able to interact with features that are extremely fine (sub-ångström level) in the material. For example, a 200 keV electron has a wavelength of only ~0.025 Å, comparing to the aforementioned wavelength of CuK_{α} X-rays of ~1.54 Å. This resolving power enables us to look directly at crystallographic planes, dislocations, domains, *etc*., which is not achievable with SEM. Also, since the interaction and imaging are both based on diffraction, it is very easy to distinguish between crystalline and amorphous regions. However, one important requirement for TEM specimens is that they need to be thin enough for electrons to pass through (*i.e*. electron-transparent). Therefore, for bulk materials, careful grinding and milling are usually needed in specimen preparation. But for nanomaterials, fortunately, most samples automatically meet the size/thickness requirement, and therefore can be used directly.

In this work, TEM studies were performed on a JEOL 2010F microscope at 200 kV accelerating voltage. Specimens were prepared firstly by dispersing the sample powder in isopropanol using sonication, and then a tiny droplet of the dispersion was deposited onto a copper TEM grid with lacey carbon (or carbon film) to allow all the isopropanol to fully evaporate.

1.5.4. Inductively Coupled Plasma Optical Emission Spectrometry

Due to the fact that lithium is transparent to EDS, *i.e*. the characteristic X-rays of light elements are blocked by the beryllium window protecting the detector, a different technique is needed to measure the amount of lithium in the sample. The technique we chose was the inductively coupled plasma optical emission spectrometry (ICP-OES). Solid samples need to be prepared in the dissolved state, and therefore are often digested by acids. Sometimes when the sample is difficult to dissolve under ambient conditions, the digestion process can be assisted with microwaves under elevated temperature and pressure. Droplets of the digested solution are fed into the device chamber and vaporized by the plasma, releasing solute atoms. These atoms are ionized to an excited state, emitting photons of characteristic wavelengths, which are then collected and measured to identify each elemental species. The number of photons is proportional to the amount of corresponding elements contained in the sample, and therefore quantitative measurements can be achieved. This technique has very high sensitivity, which is ideal for ppm (parts per million, mg/L) to sub-ppb (parts per billion, μg/L) level analysis.

The ICP-OES equipment used in this work is a Themo iCAP6300. The digestion protocol used in this dissertation was to first add the sample into 50% H_2SO_4 (usually around 5-10 ppm), and then the mixture was heated at 100 °C for 20 min using a CEM SP microwave reactor (50 W, 2.56 GHz) with stirring. The resulting solution should be a transparent one without any visible solid particles. If that is not the case, then the heating temperature and/or time can be increased until all solids are fully dissolved.

1.6. Electrochemical Measurement Technique

1.6.1. Electrochemical Impedance Spectroscopy

Electrochemical impedance spectroscopy (EIS) is a widely used technique for measuring the ionic conductivity of solid materials. Typically, the sample is probed by a small sinusoidal potential or current stimulus across a range of frequencies, and its response to such a perturbance is recorded and analyzed. The principle behind this technique is that, in a system, each individual component or conduction mechanism has its own response to various electrical stimulus frequencies.[67] For ionic conductivity measurements, the obtained data are usually presented in a Nyquist plot (imaginary impedance *vs*. real impedance), and fitted to an equivalent circuit in order to extract the contribution of each individual component.

Microscopically, the 'brick-layer' model can be used to study and extract the ionic conductivity of different contributions, namely, bulk (grain or grain interior) and GBs, from the experimental data. This model was proposed by van Dijk *et al*. and Verkerk *et al*., and has been successfully applied to polycrystalline solid electrolyte materials.[68,69] As illustrated in Figure 1 (adopted from Haile *et al*.[70]), inside the polycrystalline sample, this model represents the grains as cube-shaped 'bricks' with edge length G, close-packed together. Between the grains are the GBs with thickness g, which are divided into two categories: series GBs (perpendicular to the applied electric field) and parallel GBs (parallel to the applied electric field). Since the intrinsic GB thickness is usually on the order of 1 to 10 nm,[71,72] and the grains are large after being sintered, the condition $g \ll G$ is met and therefore, the total length of all series GBs ($L_{\perp}$) is

$$L_{\perp} = \frac{g}{G} L \tag{5}$$

and the total area of all series GBs ($A_{\perp}$) is

$$A_{\perp} = A \tag{6}$$

For parallel GBs, the total length and total area are

$$L_{\parallel} = L \tag{7}$$

$$A_{\parallel} = \frac{2g}{G} A \tag{8}$$

respectively, where L is the sample length between the two electrodes, and A is the sample cross-sectional area.

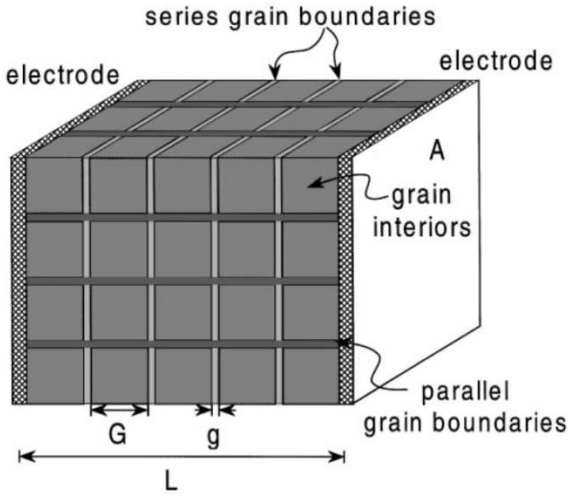

Figure 1. Schematic of the brick-layer model

For a typical pure solid electrolyte sample with ionically non-blocking electrodes, the Nyquist plot typically consists of two semicircles/arcs and a tail, as shown in Figure 2a.[40,73,74] The tail at low frequencies is usually a straight line with a slope around 45° if non-blocking electrodes are used, and is a result of solid-state diffusion through the

electrodes.[40,75] This plot can be fitted using the equivalent circuit in Figure 2b, in which Q is a constant phase element with impedance $Z_{\mathrm{Q}} = \frac{1}{Y(j\omega)^n}$ ($j = \sqrt{-1}$, ω is frequency, Y and n are constants, $0 \leq n \leq 1$), and R is a resistor with impedance $Z_{\mathrm{R}} = R$. If we assume that both the bulk and GB components in the brick-layer model can be represented by a pair of Q and R, then Figure 2b can be further improved to suit the model, as shown in Figure 3a. This circuit can be simplified (Figure 3b) so that the value of $Q_{\mathrm{Bulk+GB}\parallel}$ is (Y_{Bulk} + $Y_{\mathrm{GB}\parallel}$), and the value of $R_{\mathrm{Bulk+GB}\parallel}$ is $(1/R_{\mathrm{Bulk}} + 1/R_{\mathrm{GB}\parallel})^{-1}$. If we make another assumption that ionic conduction in both the grain interior and GBs is governed by the same mechanism (*e.g.* $\sigma_{\mathrm{GB}\parallel} = \sigma_{\mathrm{GB}\perp}$), we get

$$\begin{aligned} \frac{1}{R_1} &= \frac{1}{R_{\mathrm{Bulk}}} + \frac{1}{R_{\mathrm{GB}\parallel}} \\ \frac{A}{L}\sigma_1 &= \frac{A_{\mathrm{Bulk}}}{L_{\mathrm{Bulk}}}\sigma_{\mathrm{Bulk}} + \frac{A_{\parallel}}{L_{\parallel}}\sigma_{\mathrm{GB}\parallel} \\ \frac{A}{L}\sigma_1 &= \frac{A}{L}\sigma_{\mathrm{Bulk}} + \frac{2g}{G}\frac{A}{L}\sigma_{\mathrm{GB}} \\ \sigma_1 &= \sigma_{\mathrm{Bulk}} + \frac{2g}{G}\sigma_{\mathrm{GB}} \end{aligned} \tag{9}$$

$$\begin{aligned} \frac{1}{R_2} &= \frac{1}{R_{\mathrm{GB}\perp}} \\ \frac{A}{L}\sigma_2 &= \frac{A_{\perp}}{L_{\perp}}\sigma_{\mathrm{GB}\perp} = \frac{A}{L}\frac{G}{g}\sigma_{\mathrm{GB}} \\ \sigma_2 &= \frac{G}{g}\sigma_{\mathrm{GB}} \end{aligned} \tag{10}$$

when we take the definition $\sigma = \frac{L}{A}\frac{1}{R}$ into account.

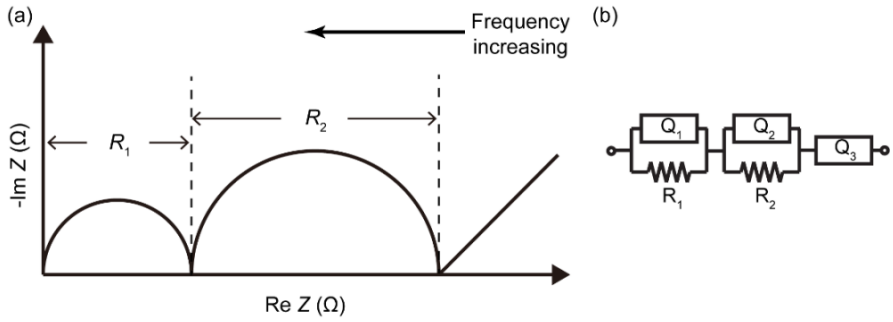

Figure 2. (a) Schematic of an ideal Nyquist plot for solid electrolyte. (b) An equivalent circuit of (a).

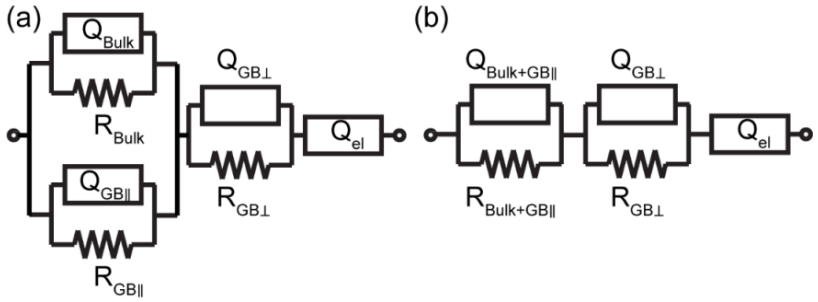

Figure 3. (a) Equivalent circuit for a typical polycrystalline sample. (b) Simplified equivalent circuit of (a).

From the derivation we can see that the first semicircle R_1 at high frequencies corresponds to the bulk and parallel grain boundary impedance, and the second semicircle R_2 in the intermediate frequency range corresponds to the series GB impedance. However, because it is difficult to characterize the microscopic properties of g and G, some approximations must be made in order to get σ_1 and σ_2 using the information that we are able to extract from the impedance measurement. First, as mentioned above, since $g \ll G$, the ratio $2g/G$ becomes negligible and hence Equation (9) approximates to

$$\sigma_1 = \sigma_{\mathrm{Bulk}} \tag{11}$$

Second, the relationship between the macroscopic and microscopic GB conductivities is

$$\sigma_{\mathrm{GB}}^{\mathrm{mac}} = \frac{G}{g}\sigma_{\mathrm{GB}}^{\mathrm{mic}} \tag{12}$$

according to van Dijk *et al*.,[68] and therefore Equation (10) becomes

$$\sigma_2 = \sigma_{\mathrm{GB}}^{\mathrm{mac}} = \sigma_{\mathrm{GB}} \tag{13}$$

The macroscopic GB conductivity will be termed σ_{GB} henceforth. It should be noted that, although the macroscopic GB conductivity is not the 'true' conductivity, we at least can obtain an estimation of the order of magnitude of the microscopic one.[68]

So far, we have demonstrated that the bulk and GB conductivities can be extracted from the experimental EIS data. The leftmost arc in the Nyquist plot (corresponding to high frequencies) is associated with the bulk conductivity, and the other arc at intermediate frequencies is associated with the GB component.

In this work, EIS was performed using a Biologic VMP3 potentiostat over the frequency range 1 Hz – 1 MHz, or a Biologic SP-200 potentiostat over 1 Hz – 5 MHz, both with 10 mV stimulus voltage and at various temperatures. Details pertaining to different samples will be given in their corresponding chapters.

1.7. Electrospinning

Electrospinning is a simple and versatile technique of producing very fine fibers/NWs from liquids or gels. It is based on electrostatic interactions, and can be deemed as a variant of electrospraying.[76] In 1887, C.V. Boys discovered that fibers can be drawn from various viscous materials when insulated and connected with an electrical

machine, and the phrase ‘electrical spinning’ was mentioned for the first time.[77] In 1995, Doshi and Reneker described the electrospinning of polymer fibers. The modern lab-scale electrospinning set up typically consists of a spinneret (*e.g.* a metallic needle tip), a metallic collector and a power supply, as depicted schematically in Figure 4. Before spinning, a syringe is filled with a viscous solution, and the spinneret is connected to the syringe. The positive electrode of the power supply is linked to the spinneret, and the collector is connected to ground. During spinning, both the syringe pump and the power supply are turned on, and the solution will be pushed out of the spinneret tip, forming a droplet. Since the droplet is electrified, it will experience dragging forces towards the collector, exerted by the electric field, but is still balanced by the surface tension of the liquid at this stage. When the applied voltage exceeds a critical value, surface tension can no longer hold the liquid in place, and then the droplet will shape into a cone and a jet will shoot out from the apex. This geometry is termed the ‘Taylor cone’, which is named after Sir Geoffrey Taylor, who studied extensively the formation of such process.[78–80] The jet gets accelerated along the field direction, and at the same time, is being stretched/elongated due to its high viscosity, forming into a fiber, which will eventually land on the collector.

Some important parameters for electrospinning are the applied voltage, distance between the tip and the collector, feed rate and viscosity of the liquid. The applied voltage determines whether the Taylor cone can form, and usually several kilovolts (kV) is required to overcome the liquid surface tension. The distance from the tip to the collector should not be too short, as it allows the liquid to be stretched completely into fibers. The combined effect of voltage and distance, which is the electric field strength

(kV/cm), can be used for selecting an appropriate range for the spinning to work. Empirically, a field strength of 0.7 to 2 kV/cm should fit most systems. The feed rate, *i.e*. the speed at which the pump is pushing the liquid, should match the applied voltage, in order to achieve a steady stream of jet. Like the field strength, the feed rate can also have a range within which the spinning is stable. Therefore, when other parameters are fixed, changing the feed rate can fine tune the diameter of fibers on the order of tens of nanometers. A rule-of-thumb is that a slower feed rate produces finer fibers. If the tip is 'spitting' liquid and there is no Taylor cone forming, the voltage needs to be increased. If the Taylor cone is formed, but disappears due to not enough liquid at the tip, then a faster feed rate is needed, and/or the voltage needs to be turned down. The viscosity of the liquid needs to be sufficiently high to produce uniform fiber diameter. Low viscosity solutions often leads to 'beaded' fibers, or varying diameter within one fiber. When beading is observed under SEM, more polymer should be added into the precursor solution. Some other factors can have effect on the spinning process as well. For example, the evaporation speed of the solvent(s) can affect the porosity of the fibers. The electrical property of the liquid, *e.g*. the ion species in it, can also determine how it behaves under applied voltage. It should be noted that the ambient humidity can also have significant effects on electrospinning. If the humidity is too high, the evaporation of solvents can be inhibited, especially for water-based precursors. Thus the jet can have difficulty solidifying, resulting in droplets on the collector (similar to spraying). In that case, a dehumidifying device should be used to reduce and control the humidity around the working area. Fortunately, the Phoenix area in Arizona is very dry most of the time

(average annual humidity: 37%), and therefore no device was deployed to control the ambient humidity in this work.

In our experiments, the home-made electrospinning setup (Figure 5) was composed of a syringe pump (New Era), a high voltage power supply (Gamma Power Supply, ES40P-20W/DAM), and a flat stationary collector made of aluminum foil. A BD PrecisionGlide 21 gauge (21G) needle firstly had its bevel removed by pliers, and then the remaining flat/blunt tip was polished by both coarse and fine sand papers. The processed needle tip was then installed onto a BD Luer-Lok Tip 5 mL syringe. Of course, needles with flat tip as-purchased are good to be used, too. Electrical connections were established using cables with alligator clips. In a typical electrospinning experiment, the voltage was set between 7 to 11 kV, depending on the type of sol (but unfortunately no rule-of-thumb can be followed); the distance between the needle tip and the collector was kept at 10-15 cm, and the feed rate was adjusted between 0.1 to 0.3 mL/h.

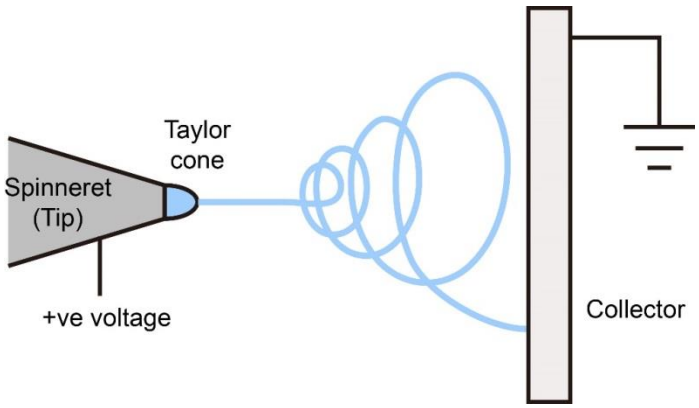

Figure 4. Schematic of an electrospinning setup

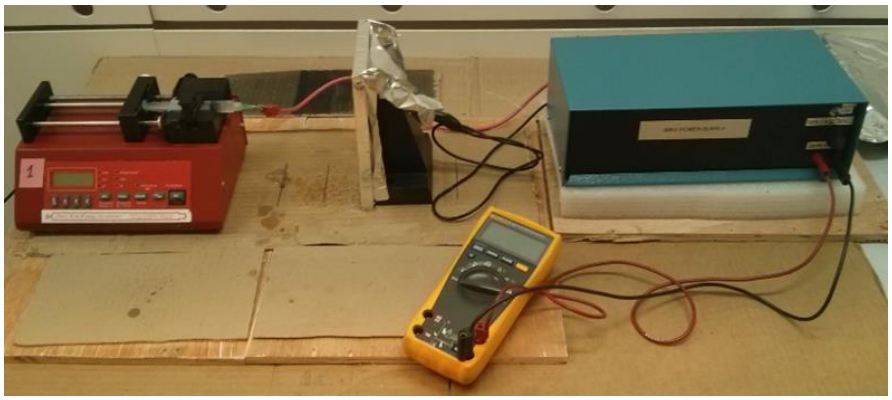

Figure 5. Electrospinning setup used in this work

1.7.1. Electrospinning of Oxide Materials

Technically speaking, the electrospinning of oxide materials can be roughly categorized into ‘decorative’ spinning and ‘formational’ spinning, in terms of the type of precursor materials. For ‘decorative’ spinning, the oxides used are pre-synthesized particles, usually in the nano- or microscale to avoid clogging the tip. These particles are dispersed in the electrospinning precursor solution as a secondary phase. After being spun, the fibers are decorated by those particles (on the surface and/or embedded in the fiber), and are usually used as-spun without any calcination. On the other hand, ‘formational’ spinning involves the formation of fibers made up completely by the oxide materials, thanks to the development of sol-gel synthesis of oxides. Typically, the oxide precursors are dissolved into a homogeneous sol, and a polymer is also dissolved in the sol to act as a sacrificial carrier, as well as to increase the viscosity. The as-spun fibers are then calcined at high temperature to remove all the organic components and to crystallize the oxides. As long as the heating ramp rate is fast, and the calcination time and/or temperature do not allow significant sintering to take place, the resulting oxides should be able to preserve the fiber morphology, owing to the dimensional confinement

of the as-spun fibers. Each calcined oxide fiber is composed of multiple crystal grains (crystallites), either small or large, connecting each other.[81] This is significantly different from the NWs yielded using other growth techniques, such as hydrothermal or chemical/physical vapor deposition, in which each NW is one single crystal.

II: ELECTROSPINNING OF LITHIUM LANTHANUM TITANATE

2.1. Introduction

LLTO is an ABO_3 type perovskite material with a generic chemical formula $Li_{3x}La_{2/3-x}\square_{1/3-2x}TiO_3$ ($0 < x < 0.16$), where □ stands for vacancies. Its crystal structure is shown in Figure 6 (image adopted from Stramare *et al.*[82]). LLTO has by far the highest reported bulk ionic conductivity among all oxide solid electrolyte materials, which exceeds 1×10^{-3} S/cm at room temperature,[83] only one order of magnitude less than that of the typical liquid electrolyte. This high value is achieved when $x \approx 0.1$, *i.e.* the stoichiometry becomes $Li_{0.33}La_{0.56}TiO_3$. The conduction mechanism is considered to depend mainly on the concentration of A-site vacancies and the size of cations.[82] Besides, it has been determined that the ionic conductivity is due entirely to the motion of Li^+ ions, so the transference number is 1.[84] However, one major problem with LLTO is that the Ti^{4+} can get reduced to Ti^{3+} when in direct contact with metallic Li,[82] thus greatly compromising its stability and preventing its use in battery applications where Li metal is used as the anode. Such reaction also promotes LLTO's electronic conductivity, which may cause the cell to short circuit. Another problem is that the GB ionic conductivity of LLTO is typically several orders of magnitude less than the bulk conductivity, and therefore the total ionic conductivity is dominated by the GB conductivity's order of magnitude, according to Equation (1). A lot of research efforts have been focused on the origin of this large difference in conductivity, and also on how to improve the GB component.

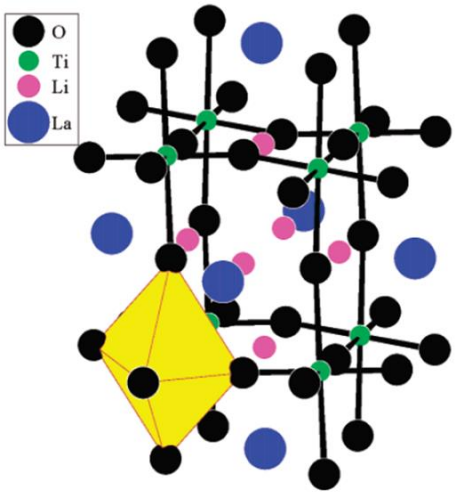

Figure 6. Crystal structure of LLTO

2.2. Experimental

2.2.1. Synthesis of LLTO

All chemicals were purchased from Sigma-Aldrich and used without further purification. To synthesize LLTO NWs, the electrospinning precursor was prepared by mixing a LLTO sol with a polymer solution. The LLTO sol was prepared according to procedures described by Dokko *et al*. [85] Lithium acetate ($LiCH_3CO_2$, 99.95%), lanthanum acetate hydrate ($La(CH_3CO_2)_3 \cdot xH_2O$, 99.9%), and titanium isopropoxide ($Ti[OCH(CH_3)_2]_4$, 97%) were weighed so that the Li:La:Ti molar ratio was 0.33:0.56:1, with 10% excess Li used to compensate loss during calcination. In a typical synthesis, 3.3 mmol lithium acetate and 5.6 mmol lanthanum acetate hydrate were dissolved in 25 mL de-ionized (DI) water. 10 mmol titanium isopropoxide was first dissolved in 5.72 mL acetic acid (CH_3COOH, $\geq$ 99%) to inhibit hydrolysis, and then 15.27 mL isopropanol (C_3H_7OH, anhydrous) was added into the mixture. The two solutions were then mixed to create the LLTO sol. The sol looked slightly ‘foggy’ at first, but it would turn completely

transparent after several hours of sitting. The polymer solution used was a 10 wt% polyvinylpyrrolidone (PVP, $(C_6H_9NO)_n$, M_w ~ 1,300,000) in acetic acid, which was prepared by dissolving PVP in acetic acid with vigorous stirring. The LLTO sol and PVP solution were then mixed at a 1:1 volume ratio to form the precursor solution for electrospinning. In a typical electrospinning run, the voltage was set to 7 kV, the distance between the needle tip and the collector was kept at 10 cm, and the feed rate was 0.3 mL/h. After electrospinning, the as-spun NWs were peeled off the collector as a free-standing, flexible mat (Figure 7a and b) and calcined in an alumina combustion boat in air at 1000 °C for 3 h (Lindberg/Blue M Moldatherm box furnace) to remove all the organic components and to crystallize the LLTO NWs. The mass of the calcined NWs is about 1/7 of the as-spun ones.

To serve as a comparison, LLTO was also synthesized using a conventional sol-gel method.[86] The conventional sol-gel was prepared by dissolving 3.3 mmol lithium nitrate ($LiNO_3$, ≥ 98.5%) and 5.6 mmol lanthanum nitrate hexahydrate ($La(NO_3)_3 \cdot 6H_2O$, ≥ 99.0%) into 12.5 mL DI water, and 10 mmol titanium isopropoxide into 10 mL isopropanol. The two solutions were mixed together to form the gel, which was then dried at 100 °C on a hotplate for 10 h in air. The dried gel was calcined in air at 500 °C for 5 h and then 1000 °C for 5 h with 10 °C/min ramp rate (Lindberg/Blue M Moldatherm box furnace).

2.2.2. Materials Characterization

XRD was performed for phase identification, and sample morphology was examined using SEM. TEM studies were carried out to examine the sample's

microscopic features. ICP-OES was performed for compositional analysis. The samples for ICP were prepared by digesting in 50% H_2SO_4 at 100 °C for 20 min using a CEM Explorer SP microwave reactor (50 W, 2.56 GHz).

2.2.3. Ionic Conductivity Measurements

In order to measure the conductivity of powders, the most common way is to press the powders into a dense pellet, sinter the pellet and then perform EIS measurement on it. As mentioned earlier, for ceramic materials, due to the fact that most of them are very poor electronic conductors, and their ionic conduction rely predominantly on the solid-state movement of conducting species through lattice defects and vacancies, it is necessary to establish a network through which the ions can 'hop' from one particle to another. Apparently, mere 'touching' of particles does not serve the purpose very well because particles only have point contacts between each other. Also since there are no externally applied forces holding the particles together, the pellet could even disintegrate on its own. Therefore, an additional sintering step is introduced to 'fuse' the particles together, creating GBs that act as an intergranular interface for ionic movement.

To make a pellet, the powders are placed in a die, and then a uniaxial force is applied to the die, generating pressure on the order of megapascals (MPa) to compact the powders. Typically in this work, 100 mg of powder was loaded into a 7 mm die set to make one pellet, and a pressure of ~250 MPa was applied (corresponding to ~1.3 metric ton). When the pressure reached the desired value, the system was left undisturbed to equilibrate for 5 min, and then the pressure was removed.

The calcined LLTO NWs and conventional sol-gel powder were made into pellets using identical procedures for ionic conductivity measurements. The sample was pressed into a 7 mm diameter pellet with a pressure of 255 MPa using a Specac Atlas manual hydraulic press. The pellet was then placed in an alumina combustion boat and sintered in air at 1100 °C for 12 h using a tube furnace (Lindberg/Blue M Mini-Mite) with a ramp rate of 1 °C/min. Both surfaces of the sintered pellets were polished using a fine grit (*e.g.* 2000 grit) sand paper and then gold (Au) electrodes were sputtered onto both surfaces. It should be noted that since Au and Li can form alloy, Au electrodes are not completely ion-blocking for Li^+, and therefore a non-vertical tail is seen in the EIS spectrum (diffusion is present). The impedance of the bulk and GB components are R_{Bulk} and R_{GB}, respectively. The ionic conductivity (σ) of each individual component can be calculated by

$$\sigma = \frac{t}{RA} \tag{14}$$

in which t is the thickness of the pellet, R is the impedance and A is the surface area of the pellet. The total ionic conductivity can then be obtained using Equation (1).

2.3. Results and Discussion

The as-spun NWs had diameters around 1 μm and smooth surface (Figure 7c). After calcination, the NWs shrank to around 100 - 200 nm in diameter and showed rough surfaces with kinky morphology, as seen in Figure 7d. SEM observation at higher magnification revealed that the NWs were formed through the merging of LLTO particles (Figure 7e), but without void or porosity, as was seen in TiO_2 NWs prepared by

electrospinning.[81] This is likely due to the higher crystallization temperature of 1000 °C for LLTO, which promoted grain coarsening, compared to only 500 °C for TiO_2. However, despite the higher temperature to crystallize LLTO, coalescence was minimized due to the separation of the NWs, with grain growth restricted by the dimensions of the as-spun NWs.

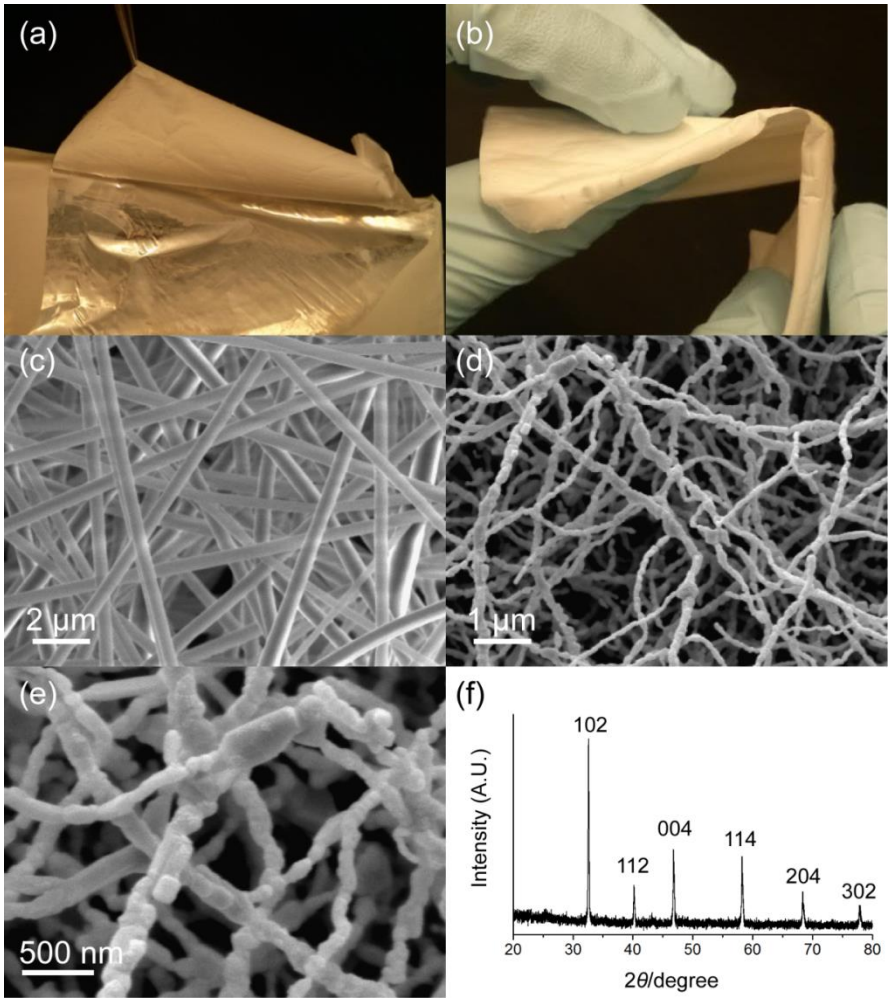

Figure 7. Photographs of (a) as-spun LLTO NW mat being removed from the collector, (b) free-standing as-spun LLTO mat with good flexibility. SEM image of LLTO NWs (c) as-spun, (d) after calcination. (e) A higher magnification of (d) showing the NW surfaces. (f) XRD pattern of electrospun LLTO NWs after calcination with *P*4/*mmm* tetragonal structure.

LLTO is stable over a wide range of compositions and can adopt simple cubic, hexagonal tetragonal, tetragonal, and orthorhombic perovskite ($ATiO_3$) distorted structures with different distribution of La^{3+}, Li^+, and vacancies on the A sites.[82] The XRD pattern of the crystallized NWs (Figure 7f) matched the tetragonal structure of LLTO with no impurity phases observed. ICP analysis gave a composition of $Li_{0.26}La_{0.61}TiO_3$ for the acid-digested NWs, indicating that the NWs are Li^+-poor ($x < 0.10$), possibly due to Li^+ loss during calcination. Although the annealing times were short, the high surface area of the NWs could facilitate Li^+ volatilization during heating.

Rietveld method was used to refine the crystal structure of the LLTO samples from their XRD patterns. This method, developed by Dutch scientist Hugo M. Rietveld, is a simulation-based technique used for the refinement of powder XRD or neutron diffraction results. Parameters such as crystallographic configuration, crystallite size and shape, instrument settings, *etc*. are varied until the simulated pattern is the closest match to the experimentally obtained pattern. Then the crystal structure of the simulated pattern can be deemed as a good representation of the sample's crystal structure. The program used was PANalytical X'Pert HighScore Plus with built-in Rietveld refinement function. Rietveld analysis of the calcined LLTO NWs XRD pattern using the La content determined from ICP, the tetragonal (*P*4/*mmm*) space group, and the atomic coordinates from Fourquet *et al*.[87] yielded lattice constants of a = 3.875 Å and c = 7.739 Å, with R_{exp} = 16.03, R_w = 15.57 (Figure 8a). Rietveld analysis of the calcined LLTO powder from conventional sol-gel is shown in Figure 8b, in which R_{exp} = 19.54, R_w = 19.42. Due to the low scattering factor of Li, its contribution to LLTO XRD patterns is often neglected and therefore was not included in the refinement.[88]

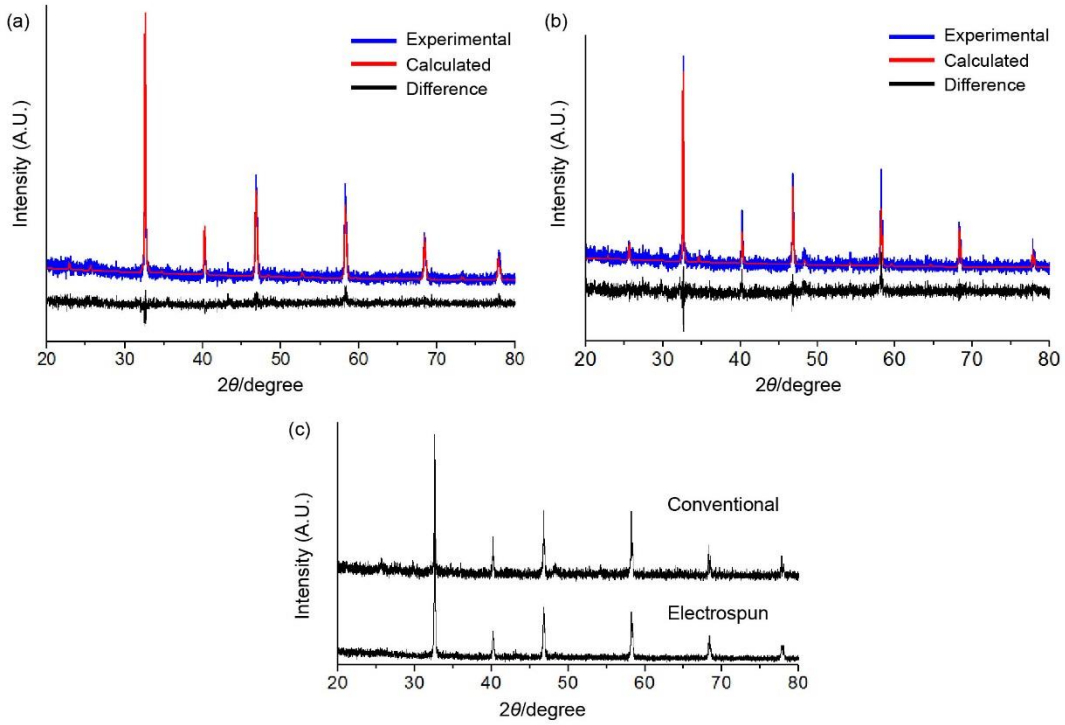

Figure 8. XRD pattern with calculated pattern from Rietveld refinement of (a) electrospun LLTO NWs and (b) conventional sol-gel LLTO; (c) XRD pattern comparison of conventional sol-gel LLTO *vs*. electrospun LLTO NWs after calcination.

TEM examination showed that the calcined NWs were about 50 - 500 nm in length and were polycrystalline, consisting of connected grains with the grain width spanning the diameter of the NWs (Figure 9a). Figure 9b shows a zoomed-in view of one grain and the inset is the corresponding selected-area electron diffraction (SAED) pattern with major spots circled and indexed, showing that each grain is a single crystal. Figure 9c is a high-resolution TEM (HRTEM) image showing the lattice fringes with spacing of 3.88 Å, which is close to the *a*-parameter obtained from XRD Rietveld refinement (3.875 Å). A typical HRTEM image of the boundary between two adjacent grains is shown in Figure 9d with the fast Fourier transform (FFT) of each grain shown in the insets. Analysis of the lattice spacings in each grain revealed that the GB is highly coherent and

the mismatch between the two grains is relatively small. There are also no visible or secondary phase segregations at the boundary.

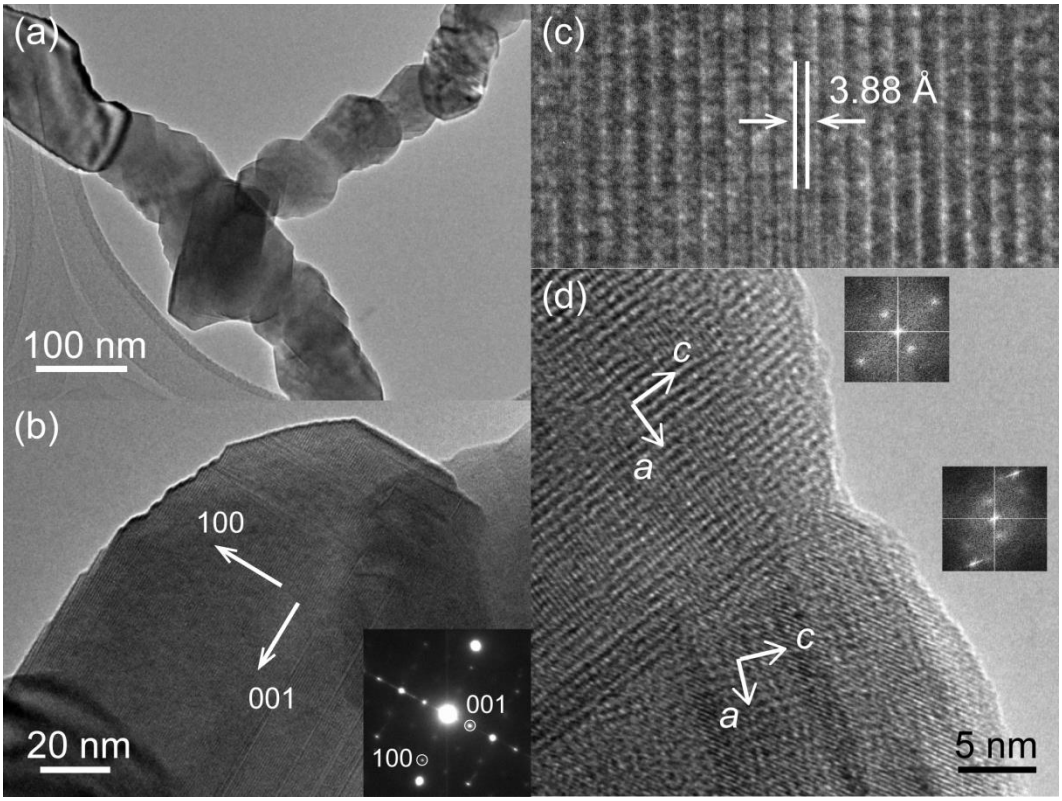

Figure 9. TEM image of calcined electrospun LLTO NWs at (a) low magnification; (b) high magnification showing individual grains. Inset shows the corresponding SAED pattern. HRTEM image of (c) the lattice fringes and (d) GB between two grains. The upper and lower inset shows the FFT of the upper and lower grain, respectively.

From these results, we can see that the calcination temperature and time required to obtain crystalline LLTO using the electrospinning approach (1000 °C for 3 h) is greatly reduced compared with conventional solid state methods.[83] Also, one problem with conventional sol-gel synthesis of LLTO is the tendency to form impurity phases such as $La_2Ti_2O_7$, particularly when using calcination times < 12 hours.[89,90] However, we can see that the LLTO prepared using electrospinning does not have these problems due

to the short diffusion distances along the NW diameters, which allows for better distribution of the ionic species.

To better characterize the Li^+ transport properties of the electrospun LLTO NWs, room temperature EIS measurements were performed and compared with LLTO synthesized using conventional sol-gel methods. The XRD pattern of the conventional sol-gel powder was very similar to that of the NW sample and had the same tetragonal structure as the NWs (Figure 8b and c). The measured impedance data are presented as Nyquist plots in Figure 10. The total ionic conductivity of the sample can be approximated by extrapolating the low frequency semicircle to intercept the *x*-axis.[40] The total conductivity given by this method is 7.8×10^{-7} S/cm for the conventional sol-gel sample and 3.3×10^{-6} S/cm for the electrospun NW sample ($t_{conventional}$ = 0.076 cm, $t_{electrospun}$ = 0.064 cm). The impedance associated with Li^+ conduction in the grain interior is typically observed in the high frequency range between 200 kHz – 13 MHz as a depressed semi-circle.[83,85] The high frequency region of the Nyquist plots is shown in Figure 10a. Due to the frequency limitation of the instrument (1 MHz maximum), the full semi-circle could not be resolved in our data. However, it is clear that the impedance is higher for the pellet prepared from conventional sol-gel compared to the NW sample.

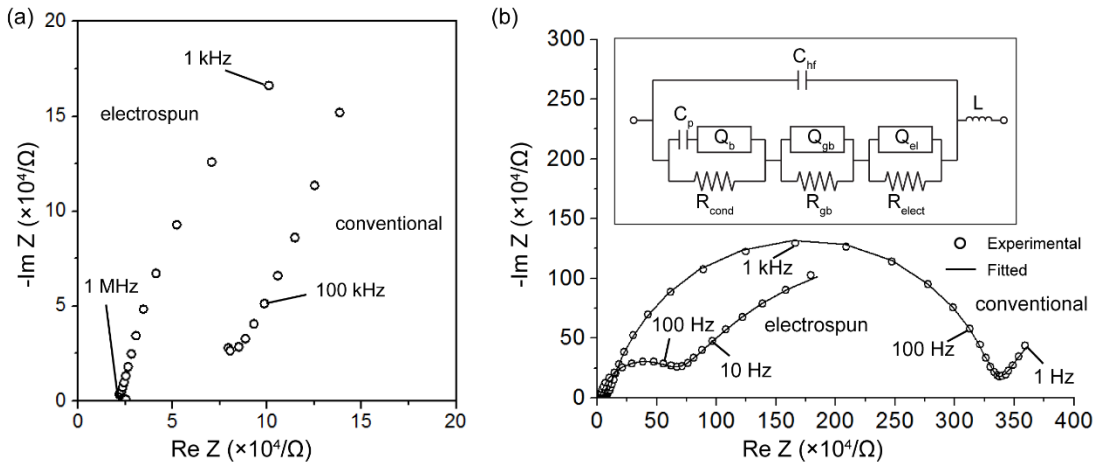

Figure 10. Nyquist plots of LLTO pellets derived from conventional sol-gel *vs*. electrospun NWs, normalized by pellet thickness in the (a) high frequency range and (b) full frequency range with fitted curves; inset shows the equivalent circuit used for fitting.

The Nyquist plots over the entire frequency range are shown in Figure 10b. Semi-circles associated with Li^+ conduction through the GBs were observed from about 200 kHz – 30 Hz and a tail due to the polarization behavior of the blocking electrode was observed at low frequencies. The GB arc is clearly much larger for the conventional sol-gel sample compared to the electrospun NW one. An equivalent circuit (Figure 10b inset) proposed by Bohnke *et al*.[91] was used to fit the experimental data, where L represents the inductance of the wire connections, C_{hf} is the high frequency capacitance, which is related to the high frequency dielectric constant of the material, C_p is the bulk polarization capacitance, Q_b is a constant phase element for the bulk interface, Q_{el} is a constant phase element for the electrode interfaces, and R_{elect}, R_{gb}, and R_{cond} represent the resistance from the electrode interfaces, GBs, and grain interior, respectively. The fitting parameters and fitted values for both samples are shown in Table 1.

Table 1. Impedance analysis results of both conventional sol-gel and electrospun LLTO samples

Equivalent Circuit Symbol	Fitting Parameter[a]	Value (Conventional)	Value (Electrospun)
L	L1	0.121×10^{-18} H	9.805×10^{-25} H
C_{hf}	C1	3.958×10^{-12} F	1.169×10^{-11} F
C_p	C2	4.982×10^{-9} F	8.753×10^{-7} F
Q_b	Q2	4.938×10^{-9}	3.313×10^{-8}
N/A	α2	0.8339	0.9091
R_{cond}	R2	245231 Ω	37121 Ω
Q_{gb}	Q3	7.848×10^{-6}	2.244×10^{-6}
N/A	α3	0.6476	0.6403
R_{gb}	R3	1046000 Ω	273266 Ω
Q_{el}	Q4	1.092×10^{-7}	3.214×10^{-8}
N/A	α4	0.3836	1.141×10^{-5}
R_{elect}	R4	7593 Ω	1384 Ω

[a] The impedance of a constant phase element is expressed by $Z = \frac{1}{A_0(j\omega)^{\alpha}}$ where A_0 is a capacitance related term, j is the current, ω is the applied frequency and α is an exponent. Here α2, α3 and α4 are the corresponding α for Q_b, Q_{gb} and Q_{el}, respectively.

The bulk (grain interior), GB, and total conductivities calculated from the fitting results are shown in Table 2. The bulk conductivity for the electrospun sample was on the order of 10^{-4} S/cm, which is comparable to some LLTO samples that were synthesized using solid state method.[92,93] Based on the ICP data, the electrospun NW sample was slightly Li^+ deficient, which would decrease its bulk ionic conductivity.[88,93–96] The total conductivity from the fitted data was on the order of 10^{-7} S/cm for the conventional sol-gel sample and 10^{-6} S/cm for the electrospun NW sample, similar to the values determined from extrapolation of the low-frequency semi-circle. Compared to the

total Li^+ conductivity reported of 7×10^{-5} S/cm for the record LLTO samples synthesized with solid state method,[83] these values are still lower. This is reasonable considering that the sol-gel LLTO typically demonstrates lower conductivity compared to LLTO prepared with solid state methods.[85,86,90]

Table 2. Ionic conductivities (S/cm) calculated from fitted impedance data of two LLTO samples

Sample	Bulk Grain Volume	Grain Boundary	Total
Conventional	2.63×10^{-5}	8.16×10^{-7}	7.91×10^{-7}
Electrospun	1.22×10^{-4}	4.54×10^{-6}	4.37×10^{-6}

The total conductivity of LLTO is typically limited by its GB conductivity.[83,85,86,92,93,95,97,98] Hence, using nanostructured LLTO with high surface-to-volume ratio and large GB area could be considered a disadvantage. Indeed, LLTO nanopowders 15 - 20 nm in diameter prepared using a combustion method showed an extremely low GB conductivity of ~ 10^{-10} S/cm at room temperature.[99] Also, previous studies have shown that increasing the LLTO grain size with sintering can improve (lower) the GB resistance,[92,100] suggesting that nanostructured LLTO is undesirable. However, the advantages of the electrospun NW samples over the conventional sol-gel sample can be clearly seen in our results. Both the bulk and GB conductivities of the NW-derived sample were more than four times higher than that in the conventional sol-gel sample, with the GB conductivity nearly six times higher for the NW sample.

To better understand the observations, the pellets were fractured and SEM images of the cross-sectional areas were taken. The pellet derived from conventional sol-gel

(Figure 14a) had many more pores and voids compared to the one derived from the electrospun NWs (Figure 14b). In general, the sintering of particles involves neck formation, mass transport and pore closure, with the major driving force being the reduction of total surface energy. NPs have very large surface-to-volume ratio, which means that the driving force of reducing surface energy is tremendous, and should in theory yield high density in sintered pellets. However, one common problem with NPs is that they tend to form agglomerates due to electrostatic or van der Waals forces. Figure 11 shows an example of such behavior. Figure 11a is an SEM image of an oxide material (LLZO) in bulk form, and Figure 11b is the same material after being ball milled, with the average particle size being approximately 25 nm. It can be seen that although the particles have their dimensions greatly reduced after ball milling, they are not scattered uniformly all over the place. Instead, they stick together and form agglomerates with different sizes. Figure 12 is a schematic of a more microscopic view to this phenomenon.[101] It shows that particles are more close-packed within each agglomerate, but the inter-agglomerate pores are large.[101–104] During sintering, these agglomerates will start to densify first since the particles inside are close together. This process is very effective and most of them can reach nearly full density. However, because the total surface energy is significantly reduced by those as-sintered agglomerates, the driving force for further densification diminishes, and so the inter-agglomerate pores are difficult to eliminate (Figure 13). On the other hand, using 1D nanomaterials can potentially circumvent this problem by taking advantage of their shape.[105,106] As illustrated in Figure 13, 1D nanomaterials tend to lie down on their axial direction (long axis) because it is the most stable (lowest energy) position, which allows them to pack more efficiently.

Additionally, the particle size of 1D nanomaterials (a few hundred nm in the long axis) is usually much larger than NPs (several tens of nm in diameter), so the increased mass helps cancel out the attractive forces between particles, and the particles are less likely to adhere to each other. These combined effects should in theory yield denser pellets and hence improved GB conductivity. The sol-gel method is known to produce very fine nanopowders, but they also suffer from agglomeration, which means that the large pores seen in Figure 14a are very likely to be the inter-agglomerate ones. Moreover, the necks between adjacent pores, which formed during the necking stage of sintering, acted as the 'bottlenecks' for ionic conduction. Because ions cannot move across the void area of pores, the effective cross-sectional area for conduction is limited to the necks only, which are usually very thin, as is apparent in Figure 14a. It has also been shown, in LLZO for example, that improving the pellet density can greatly increase the total ionic conductivity.[107] Therefore, it becomes clear that the relative density of the pellets needs to be included when reporting the conductivity, which serves as an indicator of how relevant the calculated value is to the 'true' (theoretical) conductivity. For instance, a pellet with 50% porosity (*i.e.* 50% relative density) means that only half of the volume participates in the conduction process, and the calculated macroscopic conductivity will be undoubtedly far lower than the theoretical value. In other words, the calculated/measured conductivity has at most 50% correlation with the true value, and hence cannot be deemed significant. Although there has not been an established universal relationship between the pellet density, measured conductivity and theoretical conductivity (but empirical ones exist for some individual materials), and to what extent of the pellet density can one report the measured conductivity with confidence, it shows

that improving the pellet density is very important, which again is one of the reasons for using 1D nanomaterials.

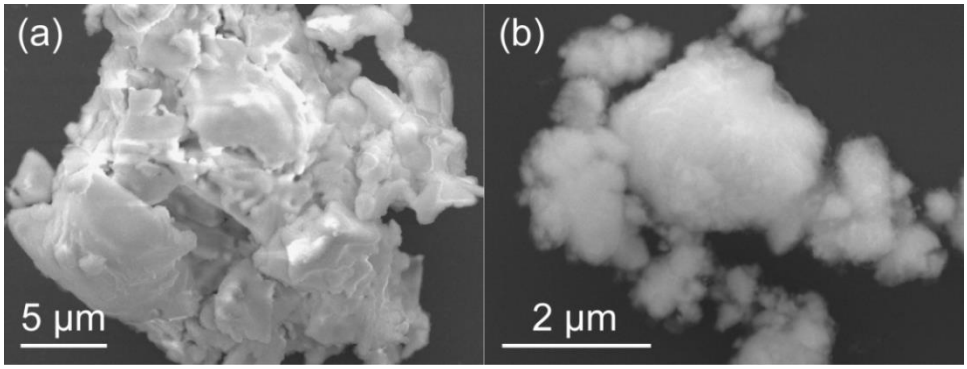

Figure 11. (a) SEM image of bulk LLZO powder. (b) SEM image of the same powder in (a) after being ball milled.

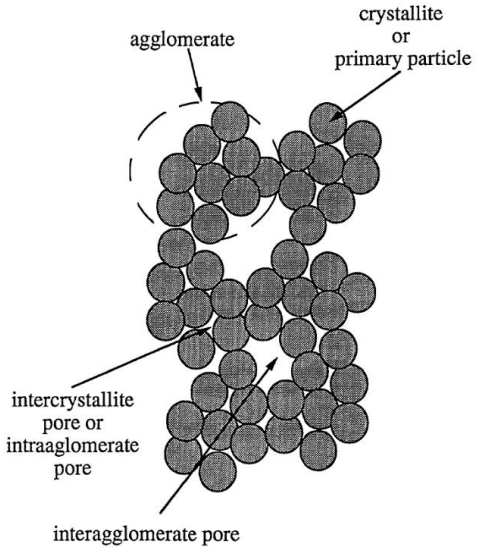

Figure 12. Schematic showing agglomeration in NPs

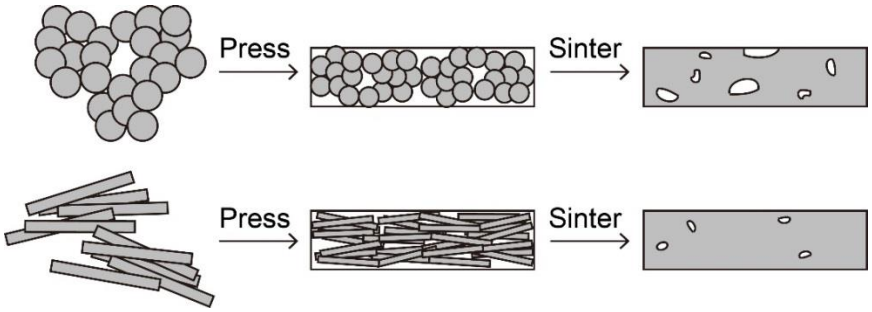

Figure 13. Schematic showing the pellet making process with different starting morphologies

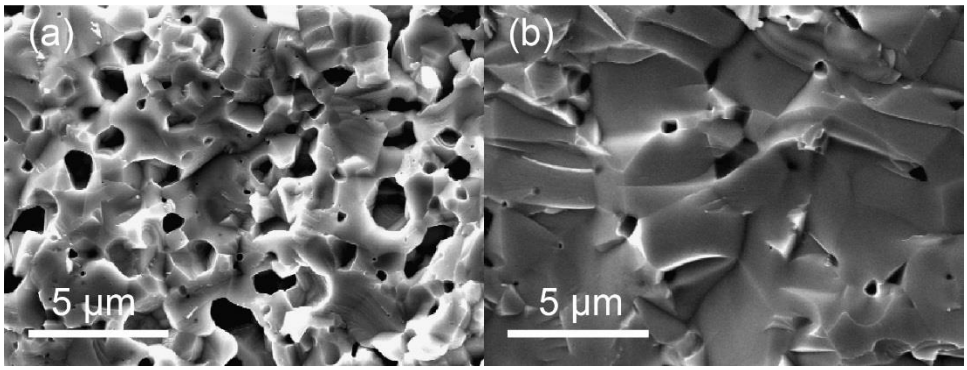

Figure 14. Cross-sectional SEM image of pellet made of (a) conventional sol-gel LLTO and (b) electrospun LLTO.

Nanocrystallites from electrospinning, on the other hand, circumvent the agglomeration problem by connecting each other and forming NWs at the crystallization stage. This is clearly observed in the TEM images of the LLTO NWs (Figure 9a), in which the NWs formed due to the merging of adjacent particles. Thus, agglomeration in NWs derived from electrospinning can be greatly prevented while maintaining many high energy surfaces, which means that the main driving force for sintering is not compromised. Hence, with the pellet preparation and calcination steps kept identical for the two samples, the increase in conductivities in the NW-derived sample can be attributed to the improved microstructure and densification processes in the pellet. Using the mass and dimensions of the pellet, the density of the pellet prepared from

conventional sol-gel LLTO was 3.42 g/cm^3. This corresponds to a relative density of ~68% (with respect to the theoretical LLTO density of 5.01 g/cm^3), which is comparable to other results obtained using similar pellet preparation conditions. For example, Ban and Choi used 1050 °C for 2 h and obtained a relative density of ~58%,[92] while Yang *et al.* achieved ~64% when sintering at 1050 °C for 8 h.[93] Higher density (> 90%) can only be achieved using more advanced techniques, such as hot-pressing.[98] In contrast, the pellet derived from electrospun NWs had a density of 4.06 g/cm^3, or a relative density of ~81%, showing improved densification using conventional sintering. These observations are also similar to previous studies that showed pressed pellets of titanate-based ferroelectric NWs had higher green and sintered densities than pellets derived from sol-gel synthesized nanopowders.[105,106] Even though the NWs lost their 1D morphology and nanostructure after sintering, the pellets derived from NWs still showed better dielectric and piezoelectric properties than those from conventional sol-gel nanopowders. The improved sinterability of the NWs in that study was attributed to: 1) better packing efficiency, 2) enhanced plastic deformation under uniaxial pressing, and 3) high amounts of surface defects such as oxygen vacancies, which can accelerate mass and energy transfer between reactants.[108] It is also reasonable to believe that similar processes may occur in the LLTO NW pellets and contribute to the better ionic conductivity properties compared to the conventional sol-gel powders.

2.4. Conclusions

In summary, LLTO NWs were successfully synthesized for the first time using electrospinning. The calcination temperature and time required to obtain crystalline

LLTO NWs was greatly reduced compared with conventional solid state and sol-gel methods, with only 3 hours at 1000 °C needed to obtain the tetragonal form of the perovskite-type structure. Characterization results showed that the NWs were polycrystalline with diameter < 200 nm and grain sizes ranging from 50 - 500 nm. Pellets derived from the electrospun materials were denser, had less void space, and displayed improved ionic conductivities over LLTO made through the conventional sol-gel route. It is expected that the ionic conductivity of the electrospun LLTO NWs can be further enhanced by tuning the parameters during synthesis, for example by identifying and minimizing the source of the Li^+ loss. These results highlight the potential of utilizing the electrospinning method to improve the ionic conductivity of sol-gel derived solid electrolytes.

III: ELECTROSPINNING OF LITHIUM LANTHANUM ZIRCONATE

3.1. Introduction

LLZO belongs to the garnet-type fast Li^+ conducting material family, with a nominal chemical formula $Li_5La_3M_2O_{12}$ (M = Nb, Ta).[109] When M is replaced by Zr, and seven instead of five Li atoms are contained per formula, the nominal stoichiometry becomes $Li_7La_3Zr_2O_{12}$, which is also called the 'Li-stuffed' (Li-rich) garnet. It has been found that the total Li^+ conductivity can reach 10^{-4} S/cm at room temperature,[110] which is considered to be originated from the excess Li in the structure.[111] Moreover, it is stable against metallic Li,[112] making it a very promising candidate for battery applications. But on the other hand, studies show that there are three polymorphs of LLZO: a tetragonal phase (t-LLZO), and two associated with the cubic phase (c-LLZO), namely, high temperature cubic (HT-cubic), and low temperature cubic (LT-cubic). The remarkable high conductivity is only associated with the HT-cubic phase (space group: $Ia\bar{3}d$, Figure 15a), which is due to the disordered Li sublattice with partial site occupation.[113] Unfortunately, this phase will transform into the tetragonal phase when temperature drops below 650 °C.[114] A common way to achieve stabilization of the HT-cubic phase at room temperature is by adding dopants, such as Al, Ta and Nb.[113,115,116] The stabilization mechanism of Al, for instance, is believed to be due to the formation of Li^+ vacancies (2 per each Al^{3+} added to maintain electroneutrality), which increases the total entropy and reduces the free energy gain from Li ordering to destabilize t-LLZO with respect to HT-cubic.[117] Indeed, when the Li content is increased from 6.24 to 7.32 per formula unit, a transformation from HT-cubic to t-LLZO was observed.[118] However, the drawback to Al

doping is that non-conducting compounds such as $LaAlO_3$ may form as byproducts that segregate at the GBs and are detrimental to the ionic conductivity.[47,113] Also, a higher activation energy for Li^+ conduction was observed in Al-containing HT-cubic LLZO compared to the Al-free counterpart, likely because the partial occupation of Al on the Li sites can cause increased electrostatic repulsion from the +3 charge of Al and also hinder Li^+ mobility.[114] For Zr substitutional dopants such as Ta and Nb, a narrow composition range for peak conductivity was observed, meaning that doping must be carefully controlled.[116,119,120] For the tetragonal phase (space group: $I4_1/acd$, Figure 15b), the ionic conductivity is 2-3 orders of magnitude lower than that of the HT-cubic phase.[121] The tetragonal distortion is a result of Li^+ ordering (blue spheres in Figure 15) that eliminates the short Li-Li interactions and disordered Li^+ clustering that is responsible for the high conductivity in the HT-cubic phase.[117,122–125] The LT-cubic phase was discovered through the development of low temperature synthesis methods.[126,127] This phase has the same structure as the HT-cubic phase, but with a slightly larger lattice constant and lower ionic conductivity than even t-LLZO.[128] Detailed studies on LT-cubic LLZO have indicated that it may be stabilized at low temperatures due to adsorption of CO_2 or H_2O,[114,128,129] and that it transforms to t-LLZO once these adsorbates are removed using calcination (*e.g.* between 450 to 650 °C).[114] Therefore, it is advantageous to find other ways to stabilize the HT-cubic LLZO phase at room temperature without relying on extrinsic dopants, or incurring the formation of LT-cubic phase.

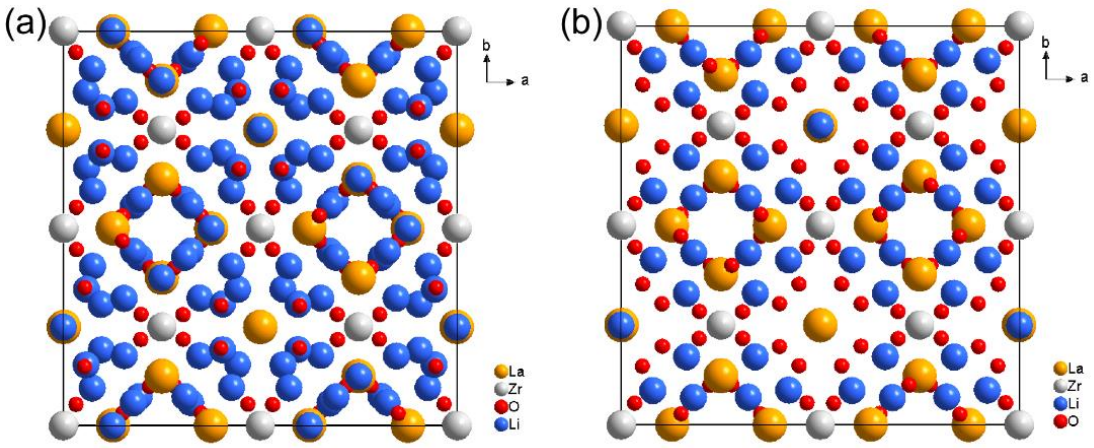

Figure 15. Crystal structure of (a) cubic phase LLZO and (b) tetragonal phase LLZO

3.2. Experimental

In order to obtain nanostructured LLZO and investigate its phase transformations, the electrospinning technique was selected as it has been a versatile method for preparing ceramic nanofibers or NWs from sol-gel precursors.[81,130] To our knowledge, this is the first report on the synthesis of LLZO NWs using electrospinning. The synthesis of LLZO NWs also enables detailed structural characterization using TEM to better understand the formation mechanism of LLZO synthesized from sol-gel precursors.

3.2.1. Synthesis of LLZO Nanowires

All chemicals were purchased from Sigma-Aldrich and used without further purification. The precursor for electrospinning was prepared by mixing an LLZO sol with a polymer solution. For the nitrate-based sol, lithium nitrate ($LiNO_3$, $\geq$ 98.5%), lanthanum nitrate hexahydrate ($La(NO_3)_3{\cdot}6H2O$, $\geq$ 99.0%), and zirconium oxynitrate hydrate ($ZrO(NO_3)_2{\cdot}xH_2O$, 99%) were weighed so that the Li:La:Zr molar ratio was 7.7:3:2, with 10% excess Li used to compensate loss during calcination. In a typical

synthesis, the three salts were dissolved in 25 mL DI water with stirring. For the acetate-based sol, lithium acetate ($LiCH_3CO_2$, 99.95%), lanthanum acetate hydrate ($La(CH_3CO_2)_3 \cdot xH2O$, 99.9%), and zirconium propoxide ($ZrC_{12}H_{28}O_4$, 70 wt% in 1-propanol) were weighed so that the Li:La:Zr molar ratio was 7.7:3:2. In a typical synthesis, 7.7 mmol of lithium acetate and 3 mmol of lanthanum acetate hydrate were dissolved in 14.5 mL DI water with stirring. 2 mmol zirconium propoxide was dissolved in 1.2 mL acetic acid (CH_3COOH, ≥ 99%) first, and then 3.06 mL isopropanol (C_3H_7OH, anhydrous) was added. The two solutions were then mixed to make the sol. In both methods, the polymer solution is a 15 wt% PVP (M_w ~ 1,300,000) solution, prepared by dissolving PVP in acetic acid with vigorous stirring. The LLZO sol and PVP solution were then mixed at a 2:1 volume ratio to form the precursor for electrospinning.

In the electrospinning setup, the distance between the needle tip and the collector was kept at 10 cm. For the acetate-based precursor, the voltage was set to 7 kV and the feed rate was 0.12 mL/h. After electrospinning, the as-spun NWs were peeled off the collector and calcined in an alumina crucible in air at 700 °C (Lindberg/Blue M Moldatherm box furnace) to remove the PVP and crystallize LLZO. The ramp time for calcination was 1 h in order to retain the NW morphology. For the nitrate-based precursor, the voltage was set to 11 kV and the feed rate was 0.16 mL/h. The ramp time for calcination was 2.5 h. The mass of the calcined NWs is about 1/4 of the as-spun ones.

3.2.2. Synthesis of Bulk LLZO

Bulk LLZO was prepared using the sol-gel method described by Janani *et al*. but without the addition of Al_2O_3.[127] In a typical synthesis, 0.7 mmol lithium nitrate, 0.3

mmol lanthanum nitrate hexahydrate, 0.2 mmol zirconium oxynitrate hydrate and 2.4 mmol citric acid ($C_6H_8O_7$, 99%) were dissolved in 50 mL DI water with stirring and heating (60 °C). 10 mL isopropanol was added into the solution as a surfactant. The mixture was then stirred and heated at 60 °C until a thick and transparent gel formed. The gel was fired at 250 °C for 1 h (Lindberg/Blue M Moldatherm box furnace) in air to obtain a brown foam-like solid. The solid was ground into powder with mortar and pestle. The powder was calcined at 500 °C for 2 h in air first, then 700 °C for 5 h in air to obtain t-LLZO, both with 2 °C/min ramp rate (Lindberg/Blue M Moldatherm box furnace).

To obtain c-LLZO from the bulk LLZO, the powder was ball milled for 1 h using a SPEX SamplePrep 8000M with methacrylate cylinder and tungsten carbide balls and caps. Ball milling is a type of grinding process in which solids are crushed by taking impact from a hard grinding media, and therefore particle size reduction can be achieved. The media needs to have higher hardness than the sample material, and the impact needs to have enough energy to induce cracking/fracture on the sample material.

3.2.3. Materials Characterization

XRD was performed for phase identification. The sample morphology was looked at using SEM. TEM examination was conducted to take high-resolution images and to study the structure of the samples.

3.3. Results and Discussion

SEM images of the as-spun NWs prepared from acetate-based precursor are shown in Figure 16a, showing diameters ranging from ~100 to 200 nm. Figure 16b-e

shows the morphology evolution of the LLZO NWs after being heated at 700 °C for 1.5 h, 2 h, 2.5 h and 3 h, respectively. Figure 16f and g are both from the same sample that was calcined for 5 h. The dimensions and morphology of the NWs did not change much after 1.5 h of heating (Figure 16b). However, as the heating time increased, the NWs became thicker and underwent coalescence to form larger ligaments. More interestingly, these morphology changes were also accompanied by a phase transformation, as determined using XRD. As shown in Figure 16h, 1.5 h was not sufficient time for formation of LLZO. The peaks labelled with asterisks were assigned to the intermediate phase $La_2Zr_2O_7$. After 2 h of calcination, a small amount of cubic phase LLZO was observed, but the majority of the sample was still $La_2Zr_2O_7$. After 2.5 h of calcination, c-LLZO was the majority product and the amount of $La_2Zr_2O_7$ decreased significantly. This is also consistent with the findings of other groups that $La_2Zr_2O_7$ is the first intermediate phase as well as the main byproduct.[61,110,126,127]

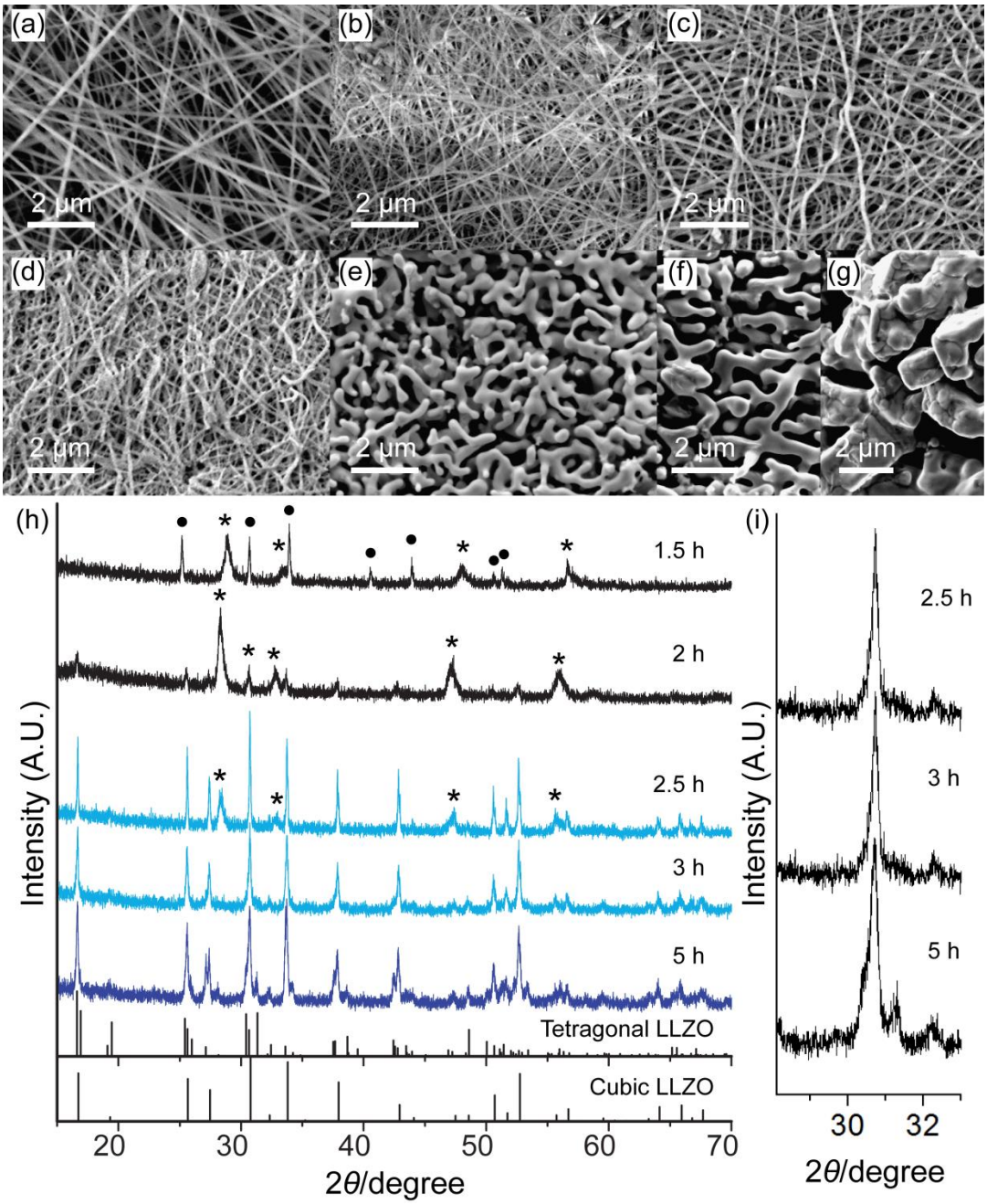

Figure 16. SEM image of (a) as-spun LLZO NWs and the NWs after calcination at 700 °C for (b) 1.5 h, (c) 2 h, (d) 2.5 h, (e) 3 h, (f) & (g) 5 h. (h) XRD patterns showing the effect of calcination time on the product. ●: unidentified intermediate phase; *: $La_2Zr_2O_7$; light blue: c-LLZO phase; dark blue: mixture of tetragonal + cubic LLZO phases. (i) Zoom-in of XRD patterns around 31°, showing the emergence of peak doublet during heating from 2.5 h to 5 h.

Figure 17a shows a flexible fiber mat made of as-spun LLZO NWs from nitrate-based precursor. The NWs showed similar as-spun morphology to that in Figure 16, only that the higher feed rate during electrospinning resulted in larger NW diameter. After being calcined with the same conditions as the ones from acetate-based precursor, the NW morphology retention appeared to be better, but they contained a higher amount of byproduct (Figure 17d, upper pattern) apart from c-LLZO. For NWs calcined in quartz crucible, c-LLZO still formed (Figure 17d, lower pattern), meaning that the formation of c-LLZO in alumina crucible was not due to Al doping. A large amount of $La_2Zr_2O_7$ was present in the product, which was likely due to the reaction between Li and the quartz crucible.

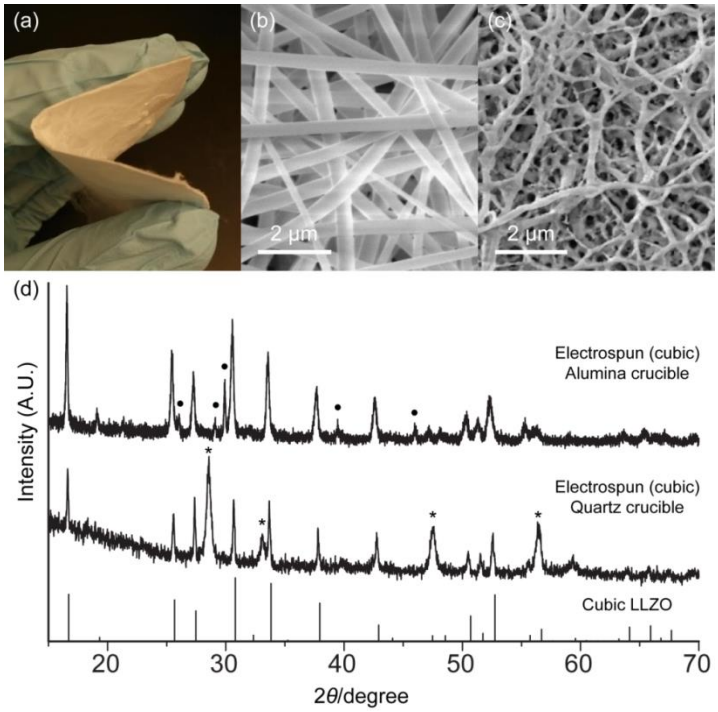

Figure 17. LLZO NWs from nitrate-based precursor. (a) Photograph of an as-spun LLZO fiber mat. (b) SEM image of as-spun LLZO NWs. (c) SEM image of LLZO NWs after 3 h of calcination at 700 °C. (d) XRD patterns of LLZO NWs calcined in alumina and quartz crucibles, matching the HT-cubic LLZO phase shown as reference. (●: La_2O_3; *: $La_2Zr_2O_7$)

To better understand the spatial distribution of $La_2Zr_2O_7$ and LLZO in the acetate-based NW sample calcined for 2.5 h, TEM studies were performed. As shown in Figure 18, TEM imaging revealed that the sample contained two types of morphologies. Polycrystalline NWs composed of small crystallites 10 to 20 nm in size (Figure 18a inset) were observed as the first morphology. The measured lattice spacing from the HRTEM image is 3.12 Å (Figure 18b inset), which corresponds to the {222} spacing of $La_2Zr_2O_7$. It is also evident from the corresponding XRD pattern (Figure 16h, 2.5 h) that the $La_2Zr_2O_7$ peaks are broadened, indicating nano-sized crystallites. The NWs appeared to be surrounded by a layer of amorphous material, as noted by the arrows in Figure 18b, which is believed to be a Li-containing amorphous phase. The formation of sol-gel derived LLZO from $La_2Zr_2O_7$ and an amorphous Li-phase has been proposed before[61] based on XRD analysis. Figure 18c shows the other morphology, which is composed of much larger crystals with particle size of 100 – 200 nm interconnected to form ligaments, similar to those observed more distinctly in the SEM images of the samples calcined for 3 h (Figure 16e). The inset in Figure 18c is an HRTEM image showing the lattice fringes with d = 2.91 Å, in good agreement with the {024} spacing (2.90 Å) in c-LLZO. Due to the thickness of the samples, it was difficult to measure the grain sizes within the ligaments, but using the Scherrer equation on the XRD pattern yielded a grain size of ~ 65 nm, which is smaller than the size of the ligament diameter.

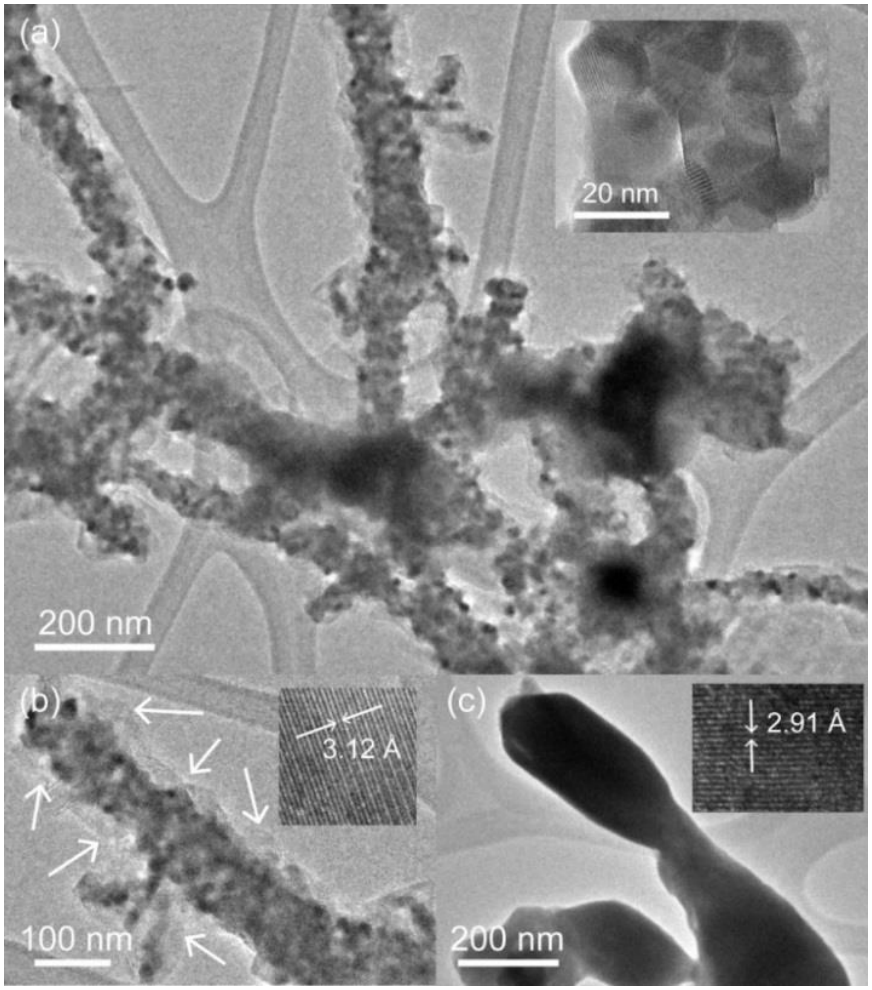

Figure 18. (a) TEM image of the acetate-based NWs calcined for 2.5 h, showing one of the morphologies. Inset is a zoomed-in view showing the $La_2Zr_2O_7$ crystals. (b) TEM image of one branch in (a) Areas indicated by arrows are considered to be a Li-containing amorphous phase. Inset is an HRTEM image showing the lattice fringes. (c) TEM image of the same sample calcined for 2.5 h, showing the other morphology (LLZO crystals). Inset shows the HRTEM image with lattice fringes.

From the TEM image (Figure 18a), it appears that nucleation of these ligaments occurred at the intersections between adjacent or crossing NWs, as shown by the dark regions. These results along with the XRD data in Figure 16h suggest that, during the calcination process, $La_2Zr_2O_7$ first formed as small crystallites within the NW core, and then reacted with the Li-rich amorphous shell to form c-LLZO. During the reaction, the NWs changed in morphology and the resulting c-LLZO formed ligaments with larger

grain sizes due to the coalescence of neighboring $La_2Zr_2O_7$ crystallites with the amorphous Li-containing regions. To our knowledge, this is the first time that the formation steps of LLZO are elucidated, which is made possible by studying the LLZO NWs synthesized from electrospinning.

As shown in the XRD pattern in Figure 16h, after 3 h of calcination, the sample was composed of phase pure c-LLZO, which is consistent with the SEM images showing the sample morphology consisted entirely of ligaments associated with c-LLZO. The c-LLZO derived from the electrospun NWs was structurally stable, as XRD performed on a sample after 14 months of storage showed the structure remained in the cubic phase (Figure 19). When heated for an additional 2 h, some of the XRD peaks split into 'doublets' (Figure 16h, 5 h), indicating the emergence of t-LLZO. This is shown more clearly in Figure 16i, in which the (024) planes for c-LLZO split into the tetragonal double peaks as the set of (042) and (024) planes at ~31°. Based on the visible coarsening of grains from the corresponding SEM images in Figure 16f and g, this cubic to tetragonal phase transformation between 3 and 5 h calcination time appears to be due to the increase in ligament diameter. Morphologically, the 5 h sample is a mixture of small ligaments (Figure 16f) and larger micron-sized particles (Figure 16g). The small ligaments are almost identical in morphology and size to the ones observed in the 3 h sample. Therefore, it is not unreasonable to assign the c-LLZO peaks to the small ligaments. On the other hand, the large particles would give rise to the tetragonal peaks emerging in the XRD pattern. Hence, from these results, we can see a clear correlation between the particle size and preferred crystal structure, with smaller particles adopting the cubic phase and larger particles the tetragonal phase.

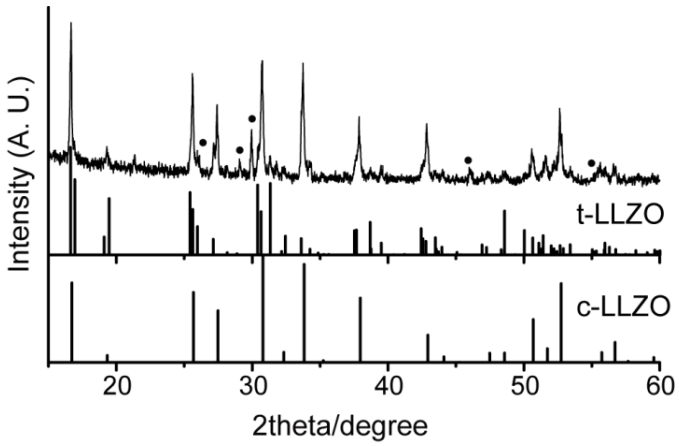

Figure 19. XRD pattern of bulk LLZO calcined at 700 °C for 3 h, showing a mixture of cubic and tetragonal LLZO. (●: La_2O_3)

In fact, similar observations have been made in other studies. Kokal *et al*. synthesized Al-free LLZO using the Pechini sol-gel method and calcined the sample at various temperatures. They found that after heating at 700 °C, the sample was c-LLZO with a particle size of 300 - 500 nm. When 800 °C was used, the particle size increased to 500 - 1000 nm and the phase changed to tetragonal.[126] In the study by Xie *et al*., Al-free c-LLZO particles with ~20 nm in size was also obtained by sol-gel methods.[131] Neither of the aforementioned groups discussed the possible mechanism for stabilization of the cubic phase in Al-free LLZO. Several mechanisms from the literature could be in play, *e.g*. a high concentration of Li vacancies,[117,118,132] CO_2 adsorption [114,128] and H_2O doping[129] (the latter two are proposed to stabilize the LT-cubic phase). Additionally, here we propose another possible mechanism, in which the phase transformation can be induced by the change in particle size as a result of the difference in surface energy between the cubic and tetragonal LLZO phases.

Several differential thermal analysis (DTA) and differential scanning calorimetry (DSC) studies have shown that the t-LLZO to HT-cubic phase transformation is an

endothermic reaction, and the reverse transformation is an exothermic one.[114,126,129] Filipovich, Kalinina and Garvie independently postulated that for any solid state endothermic transformation, there exists a critical crystallite size below which the high temperature structure is stable at temperatures much lower than the bulk transformation temperature.[133,134] This in fact has been confirmed both theoretically and experimentally in several systems, perhaps most famously in the titania (TiO_2) and zirconia (ZrO_2) polymorphs. Although rutile is the thermodynamically stable (equilibrium) phase of titania at both room temperature and elevated temperatures, anatase is a kinetically stable (metastable) phase at low temperatures.[135] Anatase can transform irreversibly to rutile by heating, which acts to accelerate the phase transformation kinetics. However, when the crystallite size is reduced to a few nanometers, anatase becomes the thermodynamically stable phase.[136–138] For zirconia, the monoclinic structure is the equilibrium phase at room temperature and it transforms to a tetragonal phase at around 1200 °C.[134,139] Since pure zirconia cannot be quenched to retain the tetragonal phase, a common practice is to stabilize it with dopants, such as yttria (Y_2O_3), to form yttria-stabilized zirconia (YSZ). However, by reducing the size of the crystallites, the tetragonal phase can exist at ambient conditions without requiring extrinsic dopants.[130,134,139–141] The origin of this phenomenon is the difference in surface energy between the two polymorphs for each material. As proposed by Garvie,[134] the most probable reason of such a transformation is that the high temperature phase zirconia has a lower surface energy than the low temperature phase. When the crystallite size is sufficiently small, the material has to undergo a phase transformation to the low surface energy phase in order to relieve the internal stress (to lower the total energy). Indeed, it was verified that the surface energy

of rutile is larger than that of anatase,[136] and the surface energy of monoclinic zirconia is larger than that of tetragonal zirconia.[140] Based on these previous works, therefore, we envision that a similar size-dependent phase transformation could also be present in LLZO. In other words, for particles with grains below a critical size, the HT-cubic phase of LLZO will be more stable than the t-LLZO phase at room temperature.

Several proof-of-concept experiments were conducted as follows. First, bulk LLZO powder was prepared and calcined at 700 °C in air for 3 h (Lindberg/Blue M Moldatherm box furnace) in an alumina crucible. Unlike the electrospun NWs, these conditions were not sufficient for a complete phase transformation, as the products were a mixture of the cubic and tetragonal phases (Figure 19). This shows that the shorter diffusion distances for the reactants (*e.g*. diffusion of Li from the Li-rich amorphous phase) in the NWs is advantageous for obtaining the crystallized LLZO using shorter calcination times. After calcining the bulk LLZO at 700 °C for 5 h, the XRD pattern showed that the product was t-LLZO (Figure 21a). SEM imaging of this product showed agglomerated particles 1 – 10 microns in size (Figure 11a). These results are consistent with the calcination studies on the c-LLZO NWs, showing that the t-LLZO structure was favored for the larger particle sizes. The data also show that Al dopants diffusion from the crucible was unlikely in the calcination conditions used, which rules out the possibility that stabilization of c-LLZO in the NWs calcined at 700 °C for 3 h was from the Al dopants. Example reaction conditions that have been used to intentionally introduce Al dopants include 850 °C for 25 h,[142] or 1180 °C for 35 h,[143,144] which are obviously of much higher temperatures and heating time periods. Moreover, examination using EDS in the SEM showed that there was no Al in the c-LLZO NW sample (Figure

22). Calcination of the as-spun NWs in a quartz crucible at 700 °C for 3 h also resulted in c-LLZO (Figure 17d), further suggesting that the stabilization is due to the small size of the NWs and not from Al dopants.

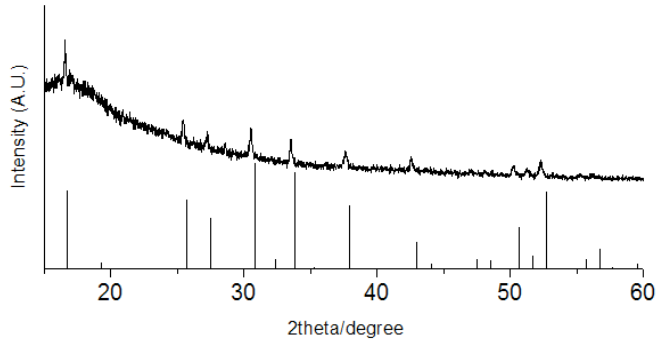

Figure 20. XRD pattern of c-LLZO derived from electrospun NWs after 14-month storage.

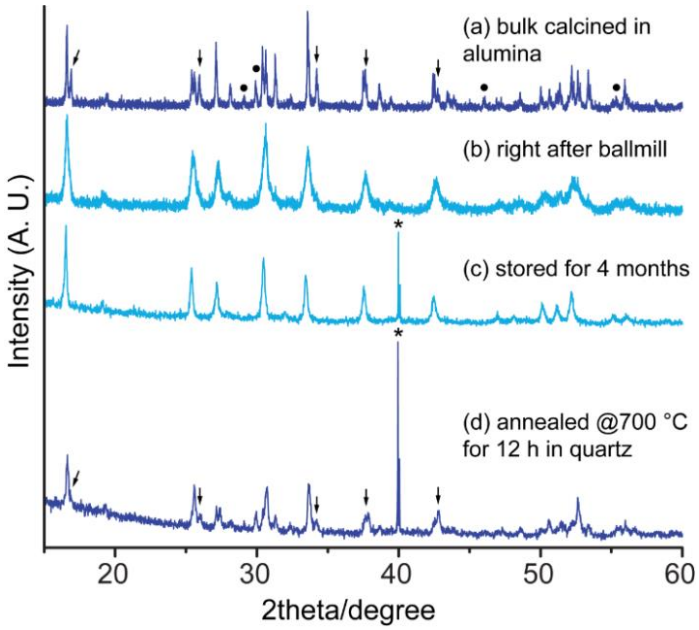

Figure 21. XRD patterns of bulk LLZO prepared from nitrate-based sol-gel (a) after calcining at 700 °C for 5 h, (b) after ball milling, (c) after 4-month storage, (d) after annealing at 700 °C for 12 h. The bulk LLZO changed from tetragonal to cubic after ball milling with the re-emergence of t-LLZO after heating. Tetragonal peak doublets are marked with arrows. (Dark blue: t-LLZO; light blue: c-LLZO; ●: La_2O_3; *: artifact peaks from instrument)

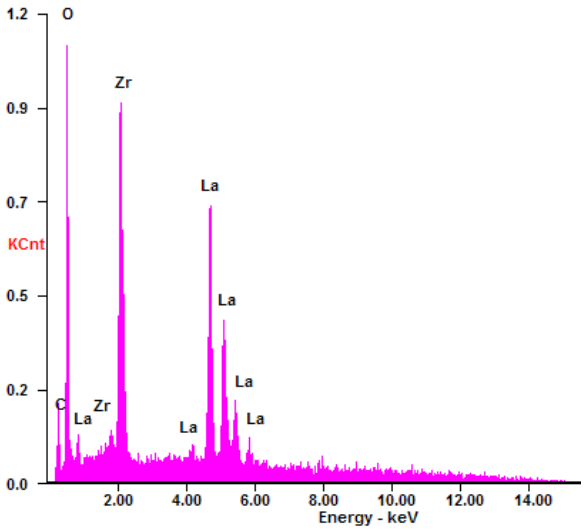

Figure 22. EDS spectrum obtained in an SEM of the c-LLZO NW sample.

The bulk t-LLZO was then subjected to ball milling for 1 h in order to reduce the particles size. SEM imaging after ball milling showed that the sample consisted of agglomerates of smaller particles (Figure 11b). The XRD pattern (Figure 21b) of the ball milled sample showed broadening of the diffraction peaks, which is an indication of particle size reduction. The grain size was determined to be ~ 25 nm using the Scherrer equation. Additionally, most of the tetragonal double peaks became unified, indicating the transformation of the bulk t-LLZO to c-LLZO after ball milling. The ball milled powder was then stored in a capped scintillation vial in air. After 4 months, the sample was re-examined with XRD. Notably, the ball milled sample was still c-LLZO (Figure 21c); also the peak widths had significantly reduced and the position of some peaks had shifted, which we interpret to be due to the relaxation of the large residual strains in the crystal lattice induced by ball milling. This stored sample was then annealed at 700 °C in a quartz crucible for 12 h in air (Lindberg/Blue M Moldatherm box furnace), the same temperature at which the sample was initially synthesized, to induce grain growth. The

resulting XRD pattern (Figure 21d) showed that a number of the doublets re-appeared, indicating the return of t-LLZO. According to the Scherrer equation, the grain size of the c-LLZO doubled to ~ 50 nm, and the grains corresponding to the t-LLZO peaks were even larger at ~ 80 nm. This further confirms our hypothesis that c-LLZO can be stabilized below a certain critical grain size, and the transformation to t-LLZO during heating is due to grain growth and particle coalescence. This notion, that c-LLZO can exist at room temperature without stabilizing extrinsic dopants provided that the particle size is small enough, is consistent with our results as well as those reported by Kokal *et al.*[126] and Xie *et al.*[131] We point out that the recent work by Teng *et al.*,[145] whereby t-LLZO was transformed to c-LLZO using pulsed laser annealing, is not in conflict with our observations, as the LLZO grain sizes in that work were ~ 4 μm and the laser irradiation may have caused sufficient local heating to thermally promote the tetragonal to cubic phase transformation.

On the other hand, the fact that the LT-cubic phase is difficult to distinguish from the HT-cubic phase by XRD complicates the discussion. One could argue that since smaller particles have larger surface area, the stabilization effect from adsorption of CO_2/H_2O would be easier than with larger particles. For example, as shown by Toda *et al.*, t-LLZO (presumably bulk particles, although the size was not reported) transformed into the LT-cubic phase after being annealed in air at 450 °C for 20 h. Partial transformation back to t-LLZO could be achieved with heating at temperatures as low as 600 °C to drive off the CO_2; full transformation could be achieved by annealing at 800 °C for just 1 h.[128] Matsui *et al.* also showed that the extraction of CO_2 from LLZO occurs around 450-650 °C.[114] Based on these results, we believe that calcination of LT-cubic

LLZO at 700 °C for 12 h would most likely drive off any adsorbed CO_2 or H_2O and cause the material to transform completely to t-LLZO, if the cubic phase stabilization were indeed adsorption-based. Since our sample remained mostly c-LLZO (Figure 21d), it is not likely that the stabilization was, as reported for the LT-cubic phase, due to CO_2 or H_2O adsorption. Similarly, in Xie *et al.*'s study, their cubic phase LLZO had been calcined at 750 °C for 20 h,[131] which means that it is also unlikely that CO_2 or H_2O was causing the stabilization. Since in their study, detailed particle size information was not provided either, it is not clear how much coalescence had occurred after 20 h of calcination. But from the TEM data provided, the LLZO was still only 20 nm after 8 h of calcination at 750 °C, so the crystallite size could still be smaller than the critical transition size even after 20 h of calcination.

This critical grain size for the LLZO phase transition can be determined from the difference in surface energy between the cubic and tetragonal phases. In the titania and zirconia systems, the calculated critical grain size showed good agreement to the experimental observations.[138,140] The surface energy difference between rutile and anatase titania is approximately 0.59 J/m^2 and the critical size is ~14 nm.[138] For monoclinic and tetragonal zirconia, the surface energy difference is ~0.36 J/m^2 and the critical size is ~9 nm.[140] Hence we can see that a smaller difference in the surface energy between the two polymorphs of a material would require a smaller critical grain size in order to stabilize the higher temperature phase. Although the surface energy for the tetragonal and cubic LLZO structures is not yet known, we expect that the surface energy difference is relatively large, since the LLZO grains must be at least larger than the $La_2Zr_2O_7$ crystallites at the intermediate stage. Based on our SEM and TEM data, it appears that c-

LLZO with dimensions of ~200 nm (the grain size would be even smaller, since the LLZO studied here was polycrystalline) have sufficient excess surface area to be stabilized at room temperature, which can be feasibly obtained with top-down approaches such as ball milling, in addition to more sophisticated chemical synthesis approaches such as the electrospinning method we present here.

While achieving c-LLZO particles using these surface energy considerations should not be difficult, the more challenging aspect is how to maintain the cubic phase once it is integrated into a suitable form, such as a dense pellet, for use as a solid state electrolyte in a Li-ion battery. Conventional sintering conditions for preparing dense LLZO pellets, *e.g*. calcination at 1230 °C for 36 h,[110] would promote significant grain growth/coalescence and hence the transformation of c-LLZO to t-LLZO. Ionic conductivity measurements on pellets derived from Al-free, c-LLZO fine powders synthesized using sol-gel methods at 750-800 °C gave rather low bulk conductivities of ~ 10^{-6} S/cm,[128,131] or two orders of magnitude lower than the c-LLZO stabilized with Al doping at high temperature. This is why the LT-cubic phase was proposed as a separate (and undesired) polymorph of LLZO with low ionic conductivity. However, based on the observations presented here, it is possible that this low apparent ionic conductivity is due to the c-LLZO transformation to the tetragonal phase during the pellet formation. For this reason, structural characterization of fine powders should also be performed after densification, particularly for correlation to ionic conductivity measurements.

Another possible reason for the lower ionic conductivity observed in Al-free, nanostructured c-LLZO could be a high GB resistance in the sintered pellet due to

insufficient densification.[128] Wolfenstine *et al.* found that the total conductivity of t-LLZO can be greatly improved by about 2 orders of magnitude to ~10^{-5} S/cm by making a very dense pellet (~98% relative density) through hot-pressing.[107] NPs have very large surface-to-volume ratios and should in theory yield sintered pellets with high density, but tend to form agglomerates due to electrostatic or van der Waals forces. Indeed, we observed this phenomenon in the ball milled LLZO (Figure 11b). Particles are more close-packed within each agglomerate, but the inter-agglomerate pores are large.[101–104] During sintering, these agglomerates can reach near-full density, while the pores between them are difficult to eliminate. This is because that the surface energy of the as-sintered agglomerate is already significantly reduced, and hence the material loses its driving force to densify further. This could possibly explain the high GB resistivity observed in the c-LLZO pellets prepared by Xie *et al*., which had a density of 89.2%.[131]

In this regard, the electrospun LLZO NWs have a clear advantage in that the nanocrystallites connect to each other and form larger structures (NWs) at the crystallization stage. Thus, agglomeration in powders derived from electrospinning can be greatly prevented while maintaining many high energy surfaces, which means that the main driving force for sintering is not compromised. Additionally, advanced sintering techniques such as two-step sintering (TSS), spark plasma sintering (SPS), or templated grain growth sintering (TGGS) may also be employed to create dense pellets from c-LLZO NWs. TSS suppresses grain growth by first using rate-controlled sintering to produce uniform pore microstructures, followed by sintering at a lower temperature where GB-controlled densification predominates.[146] SPS uses a very high current through the material, causing localized heating, with pressure applied at the same time for better

densification. Therefore the temperature required is much lower than conventional sintering and grain growth is greatly inhibited.[147] TGGS is typically achieved by embedding anisotropic particles into a precursor matrix, followed by calcination to grow the templates from the matrix materials and densify the films.[148] All of these methods have been used for preparing dense pellets of other types of NWs while preserving the 1D morphologies[108,146–149] and are anticipated to work similarly for LLZO NWs. Moreover, the highly anisotropic NWs are ideal templates for using TGGS to obtain dense films.

3.4. Conclusions

In summary, we synthesized LLZO NWs using the electrospinning technique for the first time. During calcination, $La_2Zr_2O_7$ nanocrystals and Li-containing amorphous phases are first formed, and then react with further annealing time to form c-LLZO. We also show that the transformation between the tetragonal and cubic phases in the LLZO system can be induced by a change in particle size, with c-LLZO stabilized in nanostructures and t-LLZO preferred for larger particles. The mechanism is likely related to the difference in surface energy between the high temperature cubic phase and the low temperature tetragonal phase. Using nanostructured LLZO as solid electrolyte can be beneficial in terms of ionic conductivity, cycle life, and mechanical strength, in addition to improving the safety characteristics of lithium-ion batteries.

IV: COMPOSITE POLYMER ELECTROLYTE WITH LLZO NANOWIRE FILLERS

4.1. Introduction

Developing solid Li^+ conducting electrolytes for all-solid-state batteries has attracted a great deal of research interest recently[17], particularly since solid electrolytes have the potential to increase the safety characteristics of Li metal batteries[150], mitigate the polysulfide dissolution problem in Li/S batteries[151], and circumvent the organic electrolyte oxidation problem in Li/O_2 batteries[152]. Polymer-based electrolytes avoid the brittleness and interfacial problems found in inorganic electrolytes, but are typically characterized by poor mechanical properties and low ionic conductivities at room temperature[32,33,36]. The use of composite polymer electrolytes (CPEs), comprising a polymer electrolyte embedded with ceramic fillers, has become an attractive strategy for enhancing the mechanical stability and ionic conductivity of the polymer[27,32,34,36,43,153]. The ceramic filler can increase the ionic transport of Li^+ in the CPE by several orders of magnitude, for example by decreasing the crystallinity of the conducting polymer and creating space-charge regions that can enhance the Li^+ diffusion[32,34,36,39,154].

While early studies investigated ceramic fillers comprising spherical particles of inert or 'passive' components with no intrinsic Li^+ conductivity (*e.g.* Al_2O_3 and SiO_2)[34,155], recent advances in nanomaterials synthesis have enabled the development of novel CPEs containing fillers of 'active' Li^+ conductors with NW morphologies. Electrospinning has emerged as a versatile and effective method to prepare oxide Li^+ conductors such as LLTO[45,156] and LLZO[66,157] as NWs . So far, very promising results have been reported regarding the use of these materials as CPE fillers. LLTO NWs

embedded into polyacrylonitrile (PAN) achieved three orders of magnitude improvement in room temperature Li^+ ionic conductivity compared to the polymer and Li^+ salt alone, but the mechanism was not thoroughly investigated[45]. A CPE prepared from a mat of Al-doped LLZO NWs infiltrated with PEO was effective for preventing Li dendrite formation under repeated lithium stripping/plating and also showed good flammability resistance[66]. Both studies attribute the long-range and continuous Li^+ diffusion pathways formed at the interfaces between the NWs and polymers as key to the improvements in conductivity. However there are still many critical questions remaining, such as how the nature of the ceramic filler and its properties (*e.g.* morphology, composition) affect the total conductivity of the CPE and the mechanism of conductivity enhancement.

Our group's recent studies[157,158] on nanostructured LLZO have examined the role of particle and grain size on the phase stability of this garnet-type material. Nanostructured LLZO, either prepared by electrospinning, templating onto cellulose nanofibers, or ball milling bulk powders, was observed to remain stable in the non-equilibrium cubic phase (c-LLZO) at room temperature without the use of extrinsic dopants. Calcining the c-LLZO induced grain growth and coalescence, which was correlated to the formation of the thermodynamically stable tetragonal phase (t-LLZO). As t-LLZO typically displays two orders of magnitude lower ionic conductivity than c-LLZO[121], our findings point to a new way to access c-LLZO, namely through the use of nanostructures, which can subsequently be exploited as new ceramic fillers for CPEs. This approach allows for the systematic study of different c-LLZO fillers (with and without dopants), in order to understand the critical parameters needed for high conductivity CPEs. The substitution of Al^{3+} on Li^+ sites[113,114,118,142,159] and Ta^{5+} on Zr^{4+}

sites[115,120,159–161] both stabilize c-LLZO and create Li^+ vacancies, which could increase the number of hopping sites for Li^+.[121,160–163]

Herein we report the following: 1) the synthesis of undoped and doped (with Al or Ta) c-LLZO NWs using electrospinning from a dimethylformamide (DMF)-based precursor solution; 2) the evaluation of the aforementioned LLZO NWs as fillers in CPEs containing PAN and $LiClO_4$ using EIS, and 3) the determination of the Li^+ pathways through the CPEs using selective isotope labelling and solid-state Li nuclear magnetic resonance (NMR). We also evaluated CPEs containing c-LLZO NPs or Al_2O_3 NWs to understand the role of filler type (active *vs*. passive), c-LLZO composition (undoped *vs*. doped), and c-LLZO morphology (NW *vs*. NP) on the total ionic conductivity of the CPE.

4.2. Experimental

4.2.1. Preparation of LLZO Sol-gel Precursor

All chemicals were purchased from Sigma-Aldrich and used without further purification. The precursor for electrospinning was prepared by mixing an LLZO sol and a polymer solution. In a typical synthesis, the sol was prepared by first dissolving 2 mmol zirconium propoxide ($ZrC_{12}H_{28}O_4$, 70 wt% in 1-propanol) into and 2 mL acetic acid (CH_3COOH, ≥ 99%), an then 10 mL *N*,*N*-dimethylformamide (DMF, C_3H_7NO, ≥ 99%) was added into the solution. The purpose of acetic acid was to inhibit hydrolysis of the alkoxides. Then, 7.7 mmol lithium nitrate ($LiNO_3$, ≥ 98.5%) and 3 mmol lanthanum nitrate hexahydrate ($La(NO_3)_3{\cdot}6H_2O$, ≥ 99.0%) were dissolved into the above solution with stirring (10% excess Li was used to compensate for losses *via* volatilization during

calcination). For the polymer solution, a 15 wt% PVP (M_w ~ 1,300,000) solution was prepared by dissolving PVP in acetic acid with vigorous stirring. The sol and PVP solution were then mixed at 1:1 volume ratio and stirred for 5 h to form the precursor solution. For the Al-doped sample (Al-LLZO), 0.24 mmol aluminum nitrate nonahydrate ($Al(NO_3)_3 \cdot 9H_2O$, ≥ 98%) was added into the sol with the other nitrates during the preparation (nominal final composition: $Li_{6.28}La_3Zr_2Al_{0.24}O_{12}$). For Ta-doped (Ta-LLZO), 0.5 mmol tantalum ethoxide ($TaC_{10}H_{25}O_5$, in < 2 wt% toluene) was added together with 1.5 mmol zirconium propoxide into acetic acid (nominal final composition: $Li_{6.5}La_3Zr_{1.5}Ta_{0.5}O_{12}$).

4.2.2. Electrospinning of LLZO Nanowires

The electrospinning setup used a syringe pump (New Era) to feed the precursor through the electric field generated by a high voltage power supply (Gamma Power Supply, ES40P-20W/DAM) between the needle tip and a flat stationary collector made of aluminum. The distance between the needle tip and the collector was 15 cm, the voltage of the power supply was set to 8 kV, and the syringe pump feed rate was 0.24 mL/h. The as-spun fibers formed a mat on the collector, which was then peeled off the collector and placed into an alumina combustion boat for calcination using a Lindberg/Blue M Moldatherm box furnace at 700 °C for 1 h or 3 h in air with 1 h ramp. For Al-doped and Ta-doped samples, the steps were identical. The mass of the calcined NWs is about 1/7 of the as-spun ones. The NWs were transferred immediately to an Ar-filled glovebox (M. Braun) after calcination.

4.2.3. Preparation of LLZO Nanoparticles

Bulk undoped LLZO was synthesized according to our previous work[157] using a modified synthesis from the sol-gel method reported by Janani *et al.*[127]. The bulk product (t-LLZO) was then ball milled for 1 h using a SPEX SamplePrep 8000M with methacrylate cylinder and tungsten carbide balls and caps to obtain c-LLZO NPs[157]. The average particle size was calculated to be ~25 nm according to the Scherrer equation.

4.2.4. Preparation of Composite Electrolyte

The polymer matrix for the composite solid electrolyte was prepared using a solution containing 10 wt% PAN ($(C_3H_3N)_n$, M_w ~ 150,000) and 5 wt% lithium perchlorate ($LiClO_4$, ≥ 95%) in DMF, which corresponds to ~33.3 wt% of $LiClO_4$ in the final dry film. PAN powder was dried in a vacuum oven (MTI Corporation) at 50 °C overnight prior to use, and $LiClO_4$ had been stored in an Ar-filled glovebox with H_2O level < 0.1 ppm. In a typical synthesis, 0.53 g PAN and 0.265 g $LiClO_4$ were added into 5 mL DMF and the mixture was stirred at 80 °C for 5 h in a sealed vial in air until a clear solution was obtained. The desired ceramic filler was added into the polymer matrix solution so that amount of ceramic in the final CPE was between 1 – 15 wt%, and the mixture was vigorously stirred for 5 h, after which a homogeneous suspension was obtained. To make the composite films, the suspension was then cast onto a glass slide using an automatic drawdown machine (Auto-Draw III) and dried in the vacuum oven overnight at 50 °C. The thickness of the film can be varied by applying different number of layers of tape (labeling tape, Scotch tape, *etc*.) onto the long edges of the glass slide. For the films with passive ceramic filler, Al_2O_3 NWs (Sigma-Aldrich, 2-6 nm diameter, 200-400 nm length) were used without further processing. For comparison, a blank

control sample consisting of only PAN and $LiClO_4$ was made without adding any ceramic filler. All dried films were stored in the vacuum oven at 50 °C before any tests. To remove the dried film from the glass substrate, a pair of tweezers was used to carefully lift and peel the film off. The thickness of each dried composite film was measured with a Mitutoyo micrometer, and the average thickness of all films was about 28 microns.

4.2.5. Materials Characterization

XRD on the as-calcined samples was performed for phase identification. The reference pattern for c-LLZO was generated according to Awaka *et al*.[121] The sample morphology was examined using SEM. EDS spectra were acquired using an EDAX system equipped on the SEM. TEM studies were performed to investigate the microstructure of the NW sample.

4.2.6. Electrochemical Characterization

EIS was performed using a Biologic SP-200 potentiostat with 10 mV stimulus voltage and a frequency range from 5 MHz – 1 Hz at 20 °C and 50-80 °C (10 °C interval) in air. Two identical stainless steel discs (MTI Corporation, 15.5 mm diameter) were used as the electrodes. The dried composite film was peeled off from the substrate, sandwiched between the electrodes, and trimmed to fit the size of the discs using a pair of scissors. A spring-loaded clamp was used to hold the assembly together. EIS measurements at 50-80 °C were carried out on the sample containing 5 wt% undoped LLZO NWs in a Thermo Heratherm OGS60 oven (Figure 23). Starting from 50 °C, at each temperature, sufficient time was allowed for the sample to reach equilibrium with

the surroundings before conducting measurements. The obtained conductivities were plotted on a logσ *vs.* 1/*T* graph, according to the Arrhenius equation (Equation (3)).

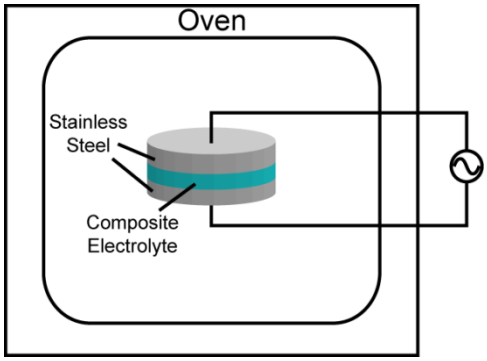

Figure 23. Schematic of EIS measurement in oven

4.2.7. Galvanostatic Cycling

The sample film (blank or composite) was sandwiched between two ^{7}Li foils, and then assembled into a coin cell. The configuration of the coin cell is: top case | wave spring | stainless steel spacer | ^{7}Li foil | sample film | ^{7}Li foil | stainless steel spacer | bottom case (all coin cell components and ^{7}Li foils were purchased from MTI Corporation). The cell was mounted onto a Biologic coin cell holder, which was connected to a Biologic MPG-2 potentiostat. The cell was cycled using a current density of 50 μA/cm^{2}, and the sign of the current switched every 300 s. The cell voltage was limited between -3 V and 3 V. All ^{7}Li cycling experiments were carried out at 20 °C in air.

4.2.8. NMR Characterization

^{6}Li and ^{7}Li magic-angle-spinning NMR experiments were carried out at the National High Magnetic Field Laboratory at Florida State University on a Bruker Avance

III-500 with Larmor frequencies of 73.6 and 194.4 MHz for ^{6}Li and ^{7}Li, respectively. A 2.5 mm Bruker HXY probe was used and the samples were spun at 25 kHz. The ^{6,7}Li chemical shift was referenced to solid LiCl at 0 ppm.

To investigate the Li^{+} diffusion pathway, a CPE containing 5 wt% of undoped LLZO NWs was prepared as described above. Symmetric cells were prepared by pressing ^{6}Li foils (1.5386 cm^{2} surface area) on either side of the CPE using a spring-loaded clamp. Charge and discharge cycling was conducted using a constant current of ±0.01 mA (300 s hold per half-cycle) on a LANHE battery testing system in an Ar-filled glovebox (M. Braun). After 10 cycles, the CPE was removed from the cell for the NMR measurement.

4.3. Results and Discussion

Our original method for preparing LLZO *via* electrospinning (Chapter III) used an aqueous precursor solution containing an LLZO sol mixed within a polymer solution, which resulted in the formation of NWs after electrospinning, as shown in Figure 24a. Calcination of these NWs at 700 °C for 3 h led to formation of c-LLZO characterized by interconnected 'ligament'-like morphologies with dimensions of 100 – 200 nm (Figure 24b). In comparison, the c-LLZO NWs obtained using a DMF-based precursor solution showed improved fiber-like morphologies (Figure 24c) after calcination for 1 h with average diameter of 276 nm (Figure 25a). The Al-doped (Al-LLZO, Figure 24e) and Ta-doped (Ta-LLZO, Figure 24g) samples displayed similar morphologies as the undoped samples (Figure 24c), but the respective dopants were detectable using EDS (Figure 25b and c).

TEM analysis revealed that the LLZO NWs were polycrystalline and became interconnected after calcination. Figure 24i shows the TEM image of the undoped LLZO NWs calcined for 1 h, while Figure 24j is an HRTEM image showing one region on a NW. The HRTEM image shows that each NW is made of multiple small grains with different shapes and sizes. The measured *d*-spacings were 3.23 Å and 2.78 Å, which corresponds to the interplanar distance of 3.24 Å for the (004) planes and 2.77 Å for the (233) planes, respectively, for c-LLZO[121]. The bottom-right inset is the SAED pattern of a few grains, with some major reflections labelled. As shown in the SEM and TEM images, if two NWs were in contact with each other, they could merge and form a 'junction' during calcination. Hence, the materials after calcination can be described as clusters or aggregates of multiple NWs connected together. In contrast, the c-LLZO NWs prepared from the aqueous precursor (Figure 24b) are characterized by ligaments with rounded ends and fewer connections with neighboring particles. Hence, the c-LLZO NWs prepared using the DMF-based precursors have more advantageous morphologies to serve as interconnected CPE fillers that can create continuous Li^+ diffusion pathways.

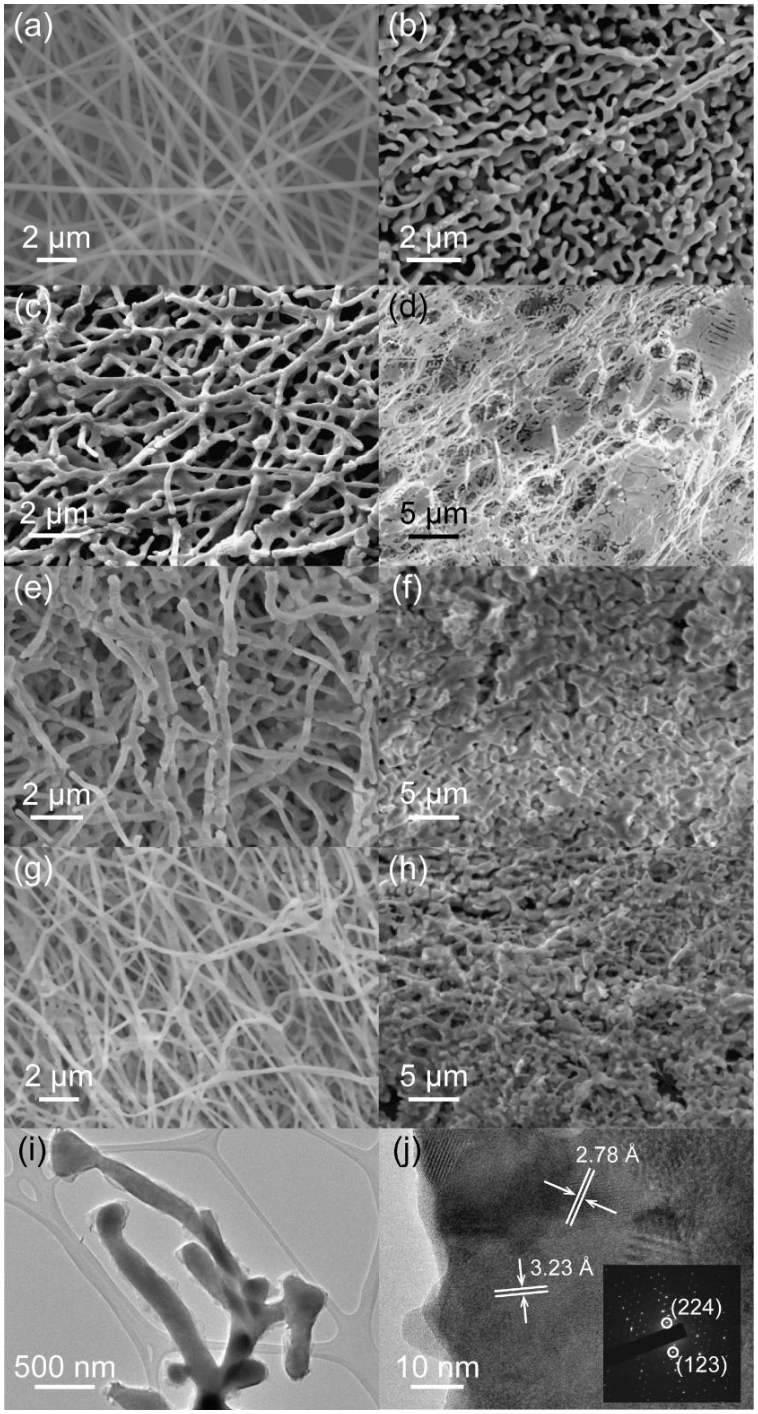

Figure 24. (a)-(h): SEM images of electrospun NWs. All calcinations were performed at 700 °C (a) As-spun NWs. (b) c-LLZO NWs prepared using water-based precursor and calcined for 3 h. (c)-(h): c-LLZO NWs prepared using DMF-based precursor and calcined for (c),(e),(g) 1 h or (d),(f),(h) 3 h. (c)-(d): undoped LLZO; (e)-(f): Al-LLZO; (g)-(h): Ta-LLZO. (i) TEM image and (j) HRTEM image of undoped c-LLZO NWs prepared from DMF-based precursor and calcined for 1 h. Inset is the corresponding SAED pattern.

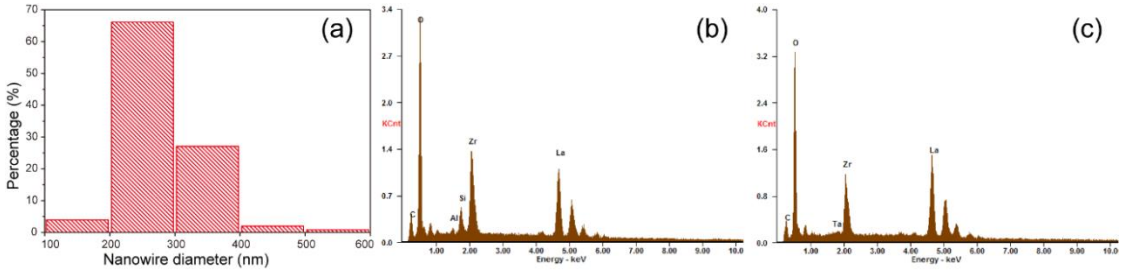

Figure 25. (a) Diameter distribution of the 1 h calcined undoped LLZO NWs. EDS spectra of (b) Al-LLZO and (c) Ta-LLZO, both calcined at 700 °C for 1 h.

XRD analysis revealed that the undoped NW product was predominately c-LLZO (Figure 26a) after calcination, but a small degree of bifurcation (peak doublets) was observed in some high angle peaks, indicating the presence of some t-LLZO (Figure 26c). However, both Al-LLZO and Ta-LZZO samples also displayed XRD peak doublets as well (Figure 26c), suggesting that the dopants did not fully stabilize the c-LLZO structure. The rapid heat treatment (1 h calcination) likely resulted in a non-uniform distribution of dopants within the grains of the NWs, leading to formation of c-LLZO (stabilized by dopants) and t-LLZO in the undoped regions. This can also explain the presence of secondary phases in the two doped samples. $La_2Zr_2O_7$ was found in Al-LLZO and La_2O_3 in Ta-LLZO, which could be caused by incomplete reaction[61,126,127] or Li^+ loss due to volatilization during calcination[110,126], with the former scenario being more likely since the heat treatment time was very short. Undoped samples subjected to 3 h calcination under the same conditions displayed particle coalescence and loss of the NW morphology (Figure 24d), along with more pronounced peak bifurcation in the XRD pattern (Figure 26c). This is consistent with our previous observations that longer heating times cause particle coalescence and increase the fraction of t-LLZO (Chapter III). For Al-LLZO and Ta-LLZO, although 3-hour calcination also destroyed the NW morphology

(Figure 24f and h, respectively), the t-LLZO peak doublets disappeared (Figure 26c). These results show that the incorporation of dopants was indeed limited by the kinetics in this situation. Unlike our previous work, in which the NWs prepared from water-based precursors required 3 h of calcination to completely crystallize into c-LZZO, the NWs from DMF-based precursors required only 1 h to form c-LLZO at the same temperature, even without requiring the dopants.

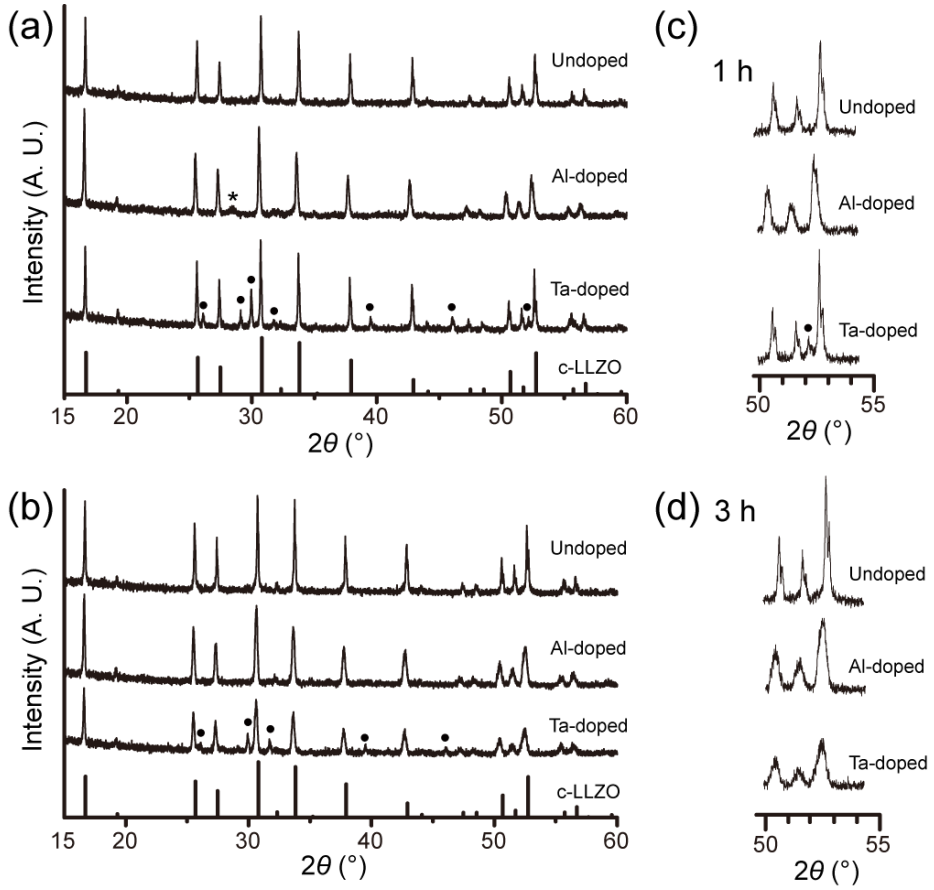

Figure 26. XRD patterns of LLZO NW samples after calcination for (a) 1 h and (b) 3 h at 700 °C; (c) zoomed-in patterns at the region around 52°. (*: $La_2Zr_2O_7$; ●: La_2O_3)

The SEM image in Figure 27a shows a top-down view of a CPE film containing 5 wt% of undoped LLZO NWs. It can be see that the NWs were embedded within the

polymer matrix, but the dispersion was not highly uniform, as some clusters/aggregates of NWs were observed. EIS measurements were performed using the configuration in Figure 27b and the equivalent circuit used for data fitting is shown in Figure 27c, which was previously applied to CPEs with ceramic fillers[164]. Here Q_c is a constant phase element for the bulk capacitance of the CPE, R_c is the overall resistance of the film, and Q_{el} is a constant phase element for the capacitances at the electrode interfaces. The representative total ionic conductivity (σ) of various CPE films obtained at 20 °C is shown in Table 3, normalized by the thickness of each individual film. The associated Nyquist plots are shown in Figure 27d, with the high-frequency region shown in Figure 27e. As expected, all of the CPEs displayed higher conductivities than the blank sample containing only PAN and $LiClO_4$, which had an ionic conductivity ~10^{-7} S/cm and a Nyquist plot (Figure 28a) similar to previous reports[43–45]. Figure 28b shows the Nyquist plots of CPEs loaded with undoped LLZO NWs at different weight percentages. The peak conductivity of 1.31×10^{-4} S/cm was observed when using 5 wt% loading, but this decreased when the wt% of filler was increased further. This was likely due to an increase in the amount of aggregated NW clusters as the wt% increased, which was also observed in PAN-based CPEs containing LLTO NW fillers.[45] EIS measurements of the CPE containing 5 wt% of undoped LLZO NWs were studied further at different temperatures (Figure 28c). The activation energy, E_a, was calculated to be 0.12 eV from the Arrhenius plot (Figure 27g).

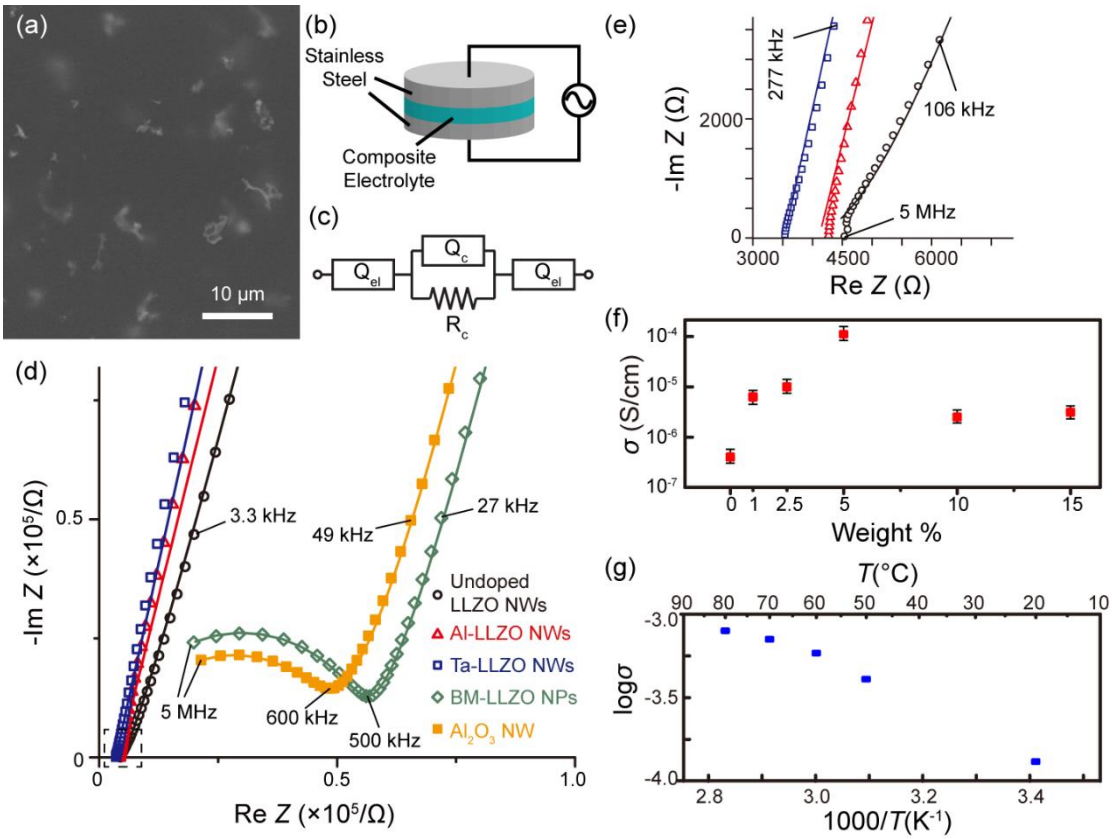

Figure 27. (a) SEM image (top-down view) of a CPE film with 5 wt% undoped LLZO NWs. (b) Schematic of the EIS test setup. (c) Equivalent circuit used for EIS data fitting. (d) Representative Nyquist plots of CPEs embedded with 5 wt% of different filler materials, all tested at 20 °C and normalized by film thickness. (e) Zoomed-in view of the region marked by dashed lines in (d). (f) Ionic conductivity comparison of CPEs embedded with different wt% of undoped LLZO NWs at 20 °C, with the conductivity of a blank sample for reference. Each point is the average of three measurements and the error bars indicate the standard deviation. (g) Arrhenius plot of CPE with 5 wt% undoped LLZO NWs. Each point is the average of two measurements.

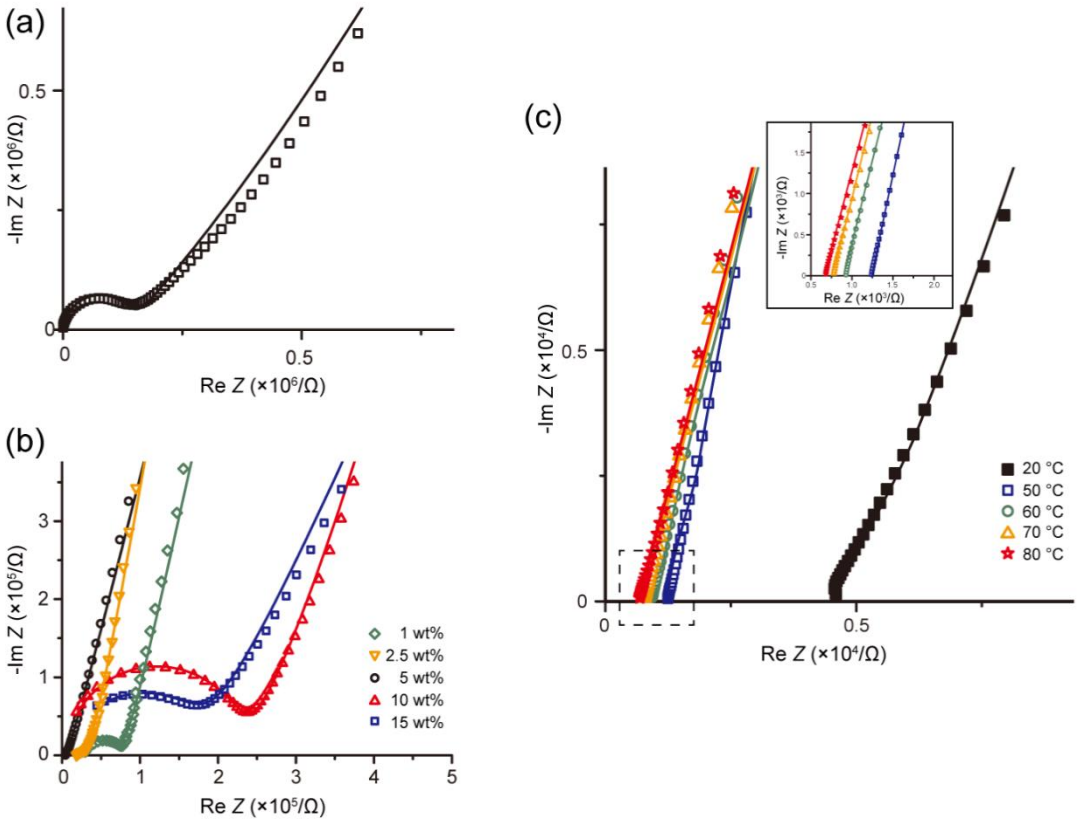

Figure 28. (a) Nyquist plot of a blank sample composed of 66.7 wt% PAN and 33.3 wt% $LiClO_4$, tested at 20 °C. (b) Nyquist plots of CPEs embedded with different wt% of undoped LLZO NWs, tested at 20 °C and normalized by film thickness. (c) Nyquist plots of samples embedded with 5 wt% undoped LLZO NWs, tested at different temperatures and normalized by film thickness. Inset shows a zoomed-in view of the region marked by dashed lines.

Table 3. Ionic conductivity of different samples at 20 °C

Ceramic Type	Wt% of Filler	σ (S/cm)
None ($LiClO_4$ in PAN only)	0	4.06×10^{-7}
Undoped LLZO NWs	1	6.17×10^{-6}
	2.5	1.00×10^{-5}
	5	1.31×10^{-4}
	10	2.52×10^{-6}
	15	3.10×10^{-6}
Al-doped LLZO NWs	5	1.27×10^{-4}
Ta-doped LLZO NWs	5	1.50×10^{-4}
BM-LLZO NPs	5	1.13×10^{-5}
Al_2O_3 NWs	5	1.52×10^{-5}

In order to investigate the effect of dopants in the LLZO on the overall ionic conductivity of the composite, CPEs loaded with 5 wt% Al- or Ta-LLZO NWs were prepared and tested. The EIS results showed that the CPEs with doped LLZO NW fillers had similar ionic conductivities, ~10^{-4} S/cm, as the CPEs with undoped LLZO NWs (Table 3), suggesting that the Li^+ conduction mechanism through the CPEs is dominated by a polymer/filler interfacial phenomenon that is independent of the LLZO filler composition. When undoped c-LLZO NPs (average particle size ~25 nm, Figure 29) prepared by ball milling bulk t-LLZO (BM-LLZO NPs) were used as fillers with 5 wt% loading, the total ionic conductivity measured was 1.13×10^{-5} S/cm (Figure 27d), roughly an order of magnitude lower than with LLZO NW fillers. This indicates that the NW morphology was important for the increased conductivity of the CPEs. Since the BM-LLZO NPs had much smaller diameters than the LLZO NWs, this suggests that the local continuous conduction pathways provided by the NWs are more important than the small

particle diameters, which has previously been shown to play a large role in the plasticizing effect for spherical fillers[34,35].

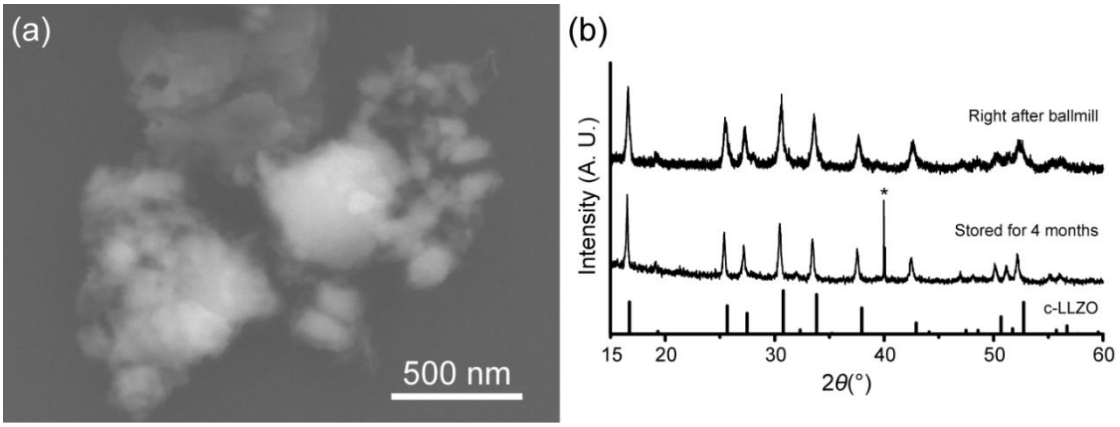

Figure 29. Bulk undoped LLZO after ball milling (BM-LLZO NPs): (a) SEM image; (b) XRD patterns with c-LLZO reference. The LLZO adopted the c-LLZO structure after ball milling and could maintain this structure even after 4-month storage. (*: Artifact peaks from instrument)

Since previous studies[45,165] have shown that the intrinsic ionic conductivity of the filler materials can also play an important role in the ionic conductivity of the CPE, 5 wt% Al_2O_3 NWs were used as passive fillers. The total ionic conductivity at room temperature was similar to that of the CPE with BM-LLZO NPs, but still higher than the conductivity of the blank sample containing only PAN and $LiClO_4$. These results suggest that the ceramic fillers should be made of 'active' Li^+ conductors with NW morphology in order to obtain CPEs with high ionic conductivity. However, since all of the LLZO NW samples displayed an ionic conductivity with similar order of magnitude, it appears that the presence of dopants is not crucial. Using the undoped c-LLZO NW as filler is advantageous because these materials had fewer impurities and better NW morphology than the doped samples.

To better understand the Li^+ local environment and transport mechanism in the LLZO-PAN CPEs, solid-state Li NMR was performed with selective ^{6}Li-isotope labelling and a ^{6}Li-^{7}Li isotope-replacement strategy. This method was established in a previous study to map out Li^+ pathways in CPEs comprising 50 wt% Al-doped LLZO particles in a PEO matrix. It was determined that there is preferential transport of Li^+ through the LLZO phase rather than the polymer phase or polymer-LLZO interface.[49] The method builds on the basis that ^{6}Li replaces ^{7}Li during Li^+ transport; by evaluating changes in the ^{6}Li amount in the CPE before and after electrochemical cycling, the Li^+ transport pathway can be determined. As shown in Figure 30a, the possible Li^+ transport pathways in the CPE in this work are through the polymer phase, through the LLZO NW phase, or through the interface region between the polymer and LLZO. In order to experimentally determine the actual Li^+ pathway in this CPE, it is necessary to first distinguish the Li ions in these three different local environments. Figure 30b shows the high-resolution ^{6}Li NMR spectra for the CPE containing 5 wt% undoped LLZO NWs, a blank film containing only PAN and $LiClO_4$, and the undoped LLZO NW powder. The ^{6}Li resonance in the undoped LLZO NWs was observed at 2.3 ppm, which is similar to what was observed in Al-doped LLZO in previous studies.[49] This resonance was not observed in the ^{6}Li NMR spectrum for the CPE, indicating that the amount of LLZO was too small. The ^{6}Li resonance of the $LiClO_4$ within the PAN in the blank film appeared at 0.90 ppm. In the NMR spectrum of the CPE, in addition to the 0.90 ppm peak, a new resonance was observed at 0.85 ppm. This resonance is attributed to $LiClO_4$ within the PAN with a local structural environment modified by the LLZO NW fillers, *i.e.* at the PAN/LLZO interfacial regions. Quantification of the Li NMR spectrum of the CPE

reveals that 37.4% of the Li resonates at 0.85 ppm and 62.6% of the Li at 0.90 ppm, which suggests that 37.4% of the PAN polymer matrix is modified by the LLZO NW filler.

To identify the preferred Li^+ diffusion pathway in the CPE, symmetric ^6Li foil/CPE/^6Li foil cells were assembled and tested galvanostatically (Figure 31). After 10 cycles, the ^6Li NMR spectrum was acquired. As shown in Figure 30c, the intensity of the resonance at 0.85 ppm increased after cycling, while the intensity of the resonance at 0.9 ppm did not change. This indicates that Li^+ prefer to travel through this LLZO-modified PAN phase rather than the unmodified PAN regions. This mechanism is different from what occurs in PEO-based CPEs containing 50 wt% Al-doped LLZO particles, wherein the Li^+ transport is preferred through an interconnected LLZO percolation network, despite the formation of an local Li^+ environment at the interface between the LLZO and PEO that is detected using NMR.[49] For the films containing 5 wt% of LLZO NWs (corresponding to 2 vol%), there is insufficient LLZO to form a percolation network to enable Li^+ transport solely through the LLZO phase. However, these results show that for the PAN-based CPEs, very little LLZO is required to modify a significant fraction of the Li^+ local environment in the polymer phase and improve the ionic conductivity.

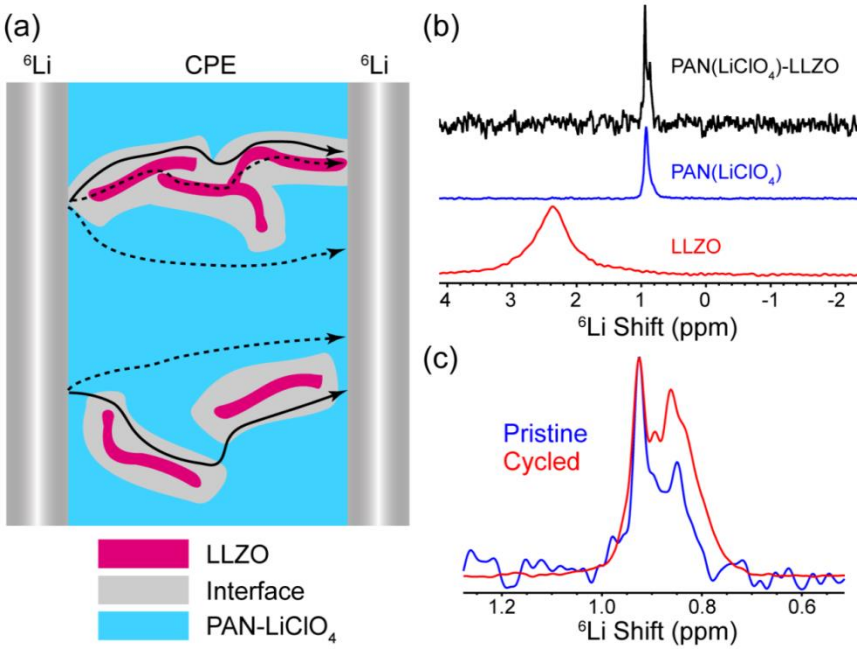

Figure 30. (a) Schematic showing possible Li^+ transport pathways in the CPE. (b) ^{6}Li NMR spectra of CPE sample containing 5 wt% undoped LLZO NWs, blank sample with only PAN and $LiClO_4$, and undoped LLZO NW powder. (c) ^{6}Li NMR spectra comparison between the as-made (pristine) and cycled CPEs containing 5 wt% undoped LLZO NWs. The cycled CPE had undergone 10 galvanostatic charge/discharge cycles in a symmetric ^{6}Li cell using 7.2 μA/cm^2.

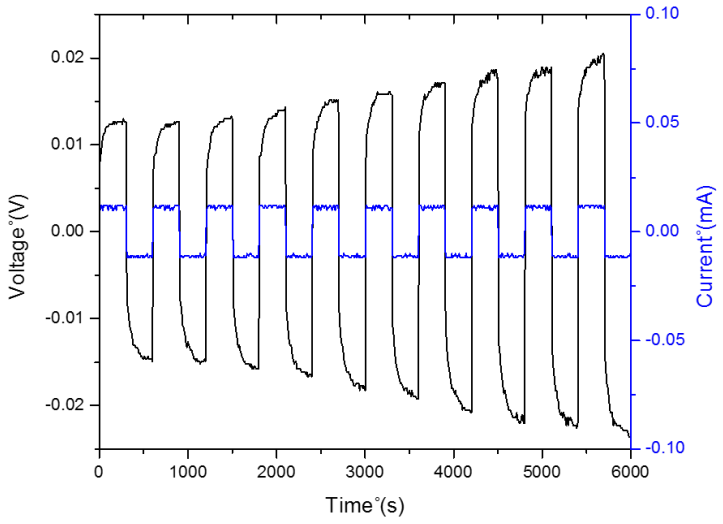

Figure 31. Galvanostatic cycling data of a symmetric ^{6}Li foil/CPE/^{6}Li foil cell. The area of ^{6}Li electrodes is 1.5386 cm^2. The CPE contains 5 wt% undoped LLZO NWs.

Unlike PEO-based CPEs, in which ionic conductivity is increased by introduction of ceramic fillers acting as plasticizers to decrease the crystallinity of the polymer and enhance Li^+ transport through amorphous PEO regions[34], previous studies demonstrated that introduction of ceramic fillers does not significantly change the crystallinity of PAN films containing Li^+ salts[43,45]. XRD of the blank sample and CPE with 5 wt% undoped LLZO NWs also confirmed that the PAN was amorphous in both cases (Figure 32). Instead, LLZO NW fillers could improve the ionic conductivity of the CPE by increasing the Li^+ dissociation from the ClO_4^- anion, which would increase the concentration of free Li^+ in the CPE[44,166,167]. This has been observed in CPEs using ceramic fillers with high dielectric constants and Lewis base surface groups with high affinity to the salt anion[37,168]. The dielectric constants (relative permittivities) of doped c-LLZO materials have been reported to be in the range of 40 – 60[169,170]. This is much higher than the dielectric constant of 9 for Al_2O_3[171], indicating that LLZO can better promote ionic dissociation of the salt. Differences between the Lewis basicity of Al_2O_3 and LLZO may also explain the observed differences in conductivity for the CPEs containing either type of NW filler. Al_2O_3 is amphoteric and contains both surface Lewis acid centers (Al) and Lewis base centers (O)[37]. Although the acid-base properties of LLZO has, to our knowledge, not been thoroughly investigated yet, the negatively charged Li^+ vacancies created by Al[118,163,172] and Ta[132,173] doping should act as strong Lewis base centers. Li^+ vacancies may also play a role in the stabilization of the c-LLZO structure[117,118,132] in the undoped LLZO NW samples, although this needs to be further investigated. We also note that the ionic conductivities of our CPEs are of the same order of magnitude but roughly half of those reported by Liu, *et al*.[45], who observed a peak conductivity using 15 wt% LLTO

NWs with average diameter of 223 nm. Similar to LLZO, LLTO is also characterized by Li^+ vacancies[82]. Currently, it is not clear why only 5 wt% loading of LLZO NWs was needed to reach the peak CPE conductivity in our study, and why the peak value is lower than what was observed with the LLTO NWs. However, this could be due to differences in NW diameter and aggregation, differences in the intrinsic ionic conductivity of LLTO *vs.* LLZO, in addition to the aforementioned dielectric and Lewis base properties of the materials. Also, since there was no elucidation of the conductivity-enhancing mechanism or Li^+ transport pathways in the study using LLTO NW fillers, there could be other potential causes that are still unknown.

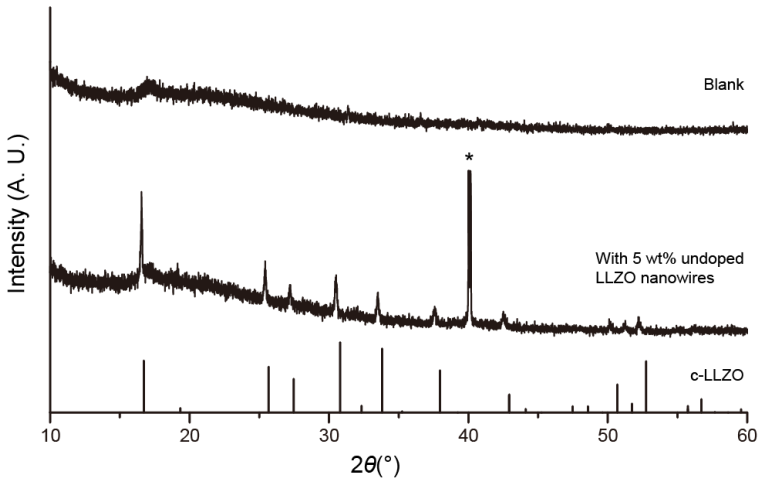

Figure 32. XRD patterns of blank sample (PAN with 33.3 wt% $LiClO_4$) and CPE containing 5 wt% undoped LLZO NWs, with c-LLZO for reference. (*: Artifact peaks from instrument)

Galvanostatic cycling was also performed to test the durability of the CPE sample containing 5 wt% undoped LLZO NWs (Figure 33a). The CPE film was sandwiched between two Li foils and tested at 20 °C, with a constant current density of 50 μA/cm^2 and changing the sign of the current every 300 s. It can be seen that there was an overall

decrease in the cell voltage, which is similar to other studies.[66,174] At around the 535th cycle, a sudden voltage drop was observed (Figure 33b), which is characteristic of the penetration of the CPE film by Li dendrites, leading to failure of the cell.[174,175] For comparison, a blank film containing no LLZO fillers was cycled under the same conditions and the result is shown in Figure 33c. The overall cell voltage remained stable until it failed at the 492nd cycle (Figure 33d), which is about 92% of the lifetime of the CPE containing 5 wt% undoped LLZO NWs. It should be noted that the data presented in Figure 33b are the best cycling result obtained from our blank samples. All other blank samples either failed at very early stages (*e.g.* at the 221st cycle), or did not display stable cell voltages (Figure 34). These results imply that adding an appropriate amount of undoped LLZO NWs may have also reinforced the polymer matrix and made it mechanically stronger, similar to what has been observed in other nanocomposite polymer electrolytes[29,34,45,49,66,176], which helped to resist the piercing of the CPE from growing Li dendrites. Further mechanical property testing in the future may help to shed light on this enhancement in cycling durability.

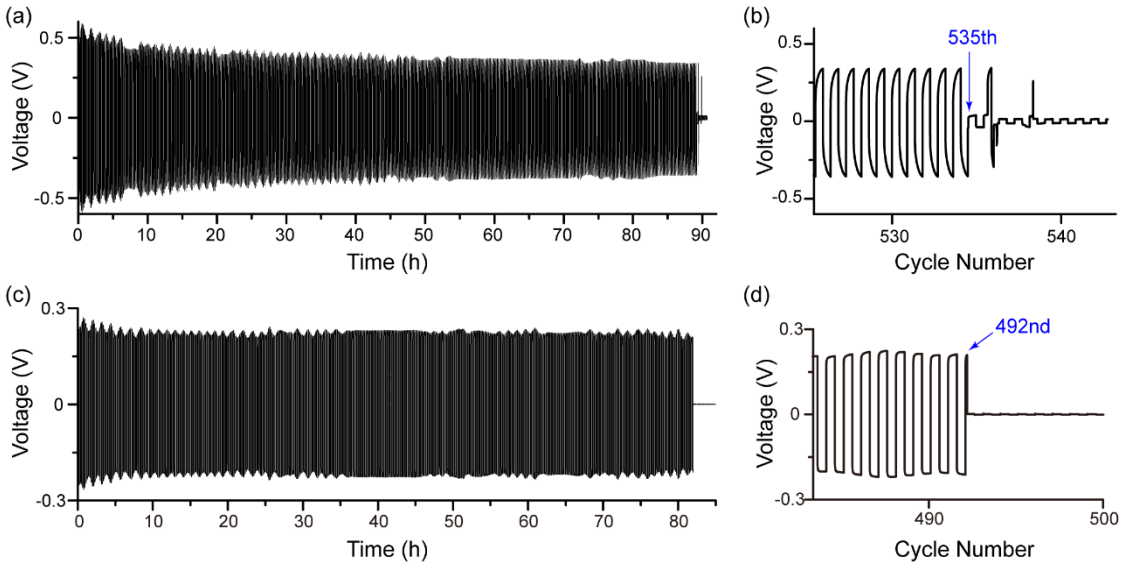

Figure 33. (a) Li symmetric cell galvanostatic cycling data of a CPE sample containing 5 wt% undoped LLZO NWs. (b) The tail region of (a), showing the sudden voltage drop. (c) Li symmetric cell galvanostatic cycling data of a blank sample. (d) The tail region of (c), showing the sudden voltage drop.

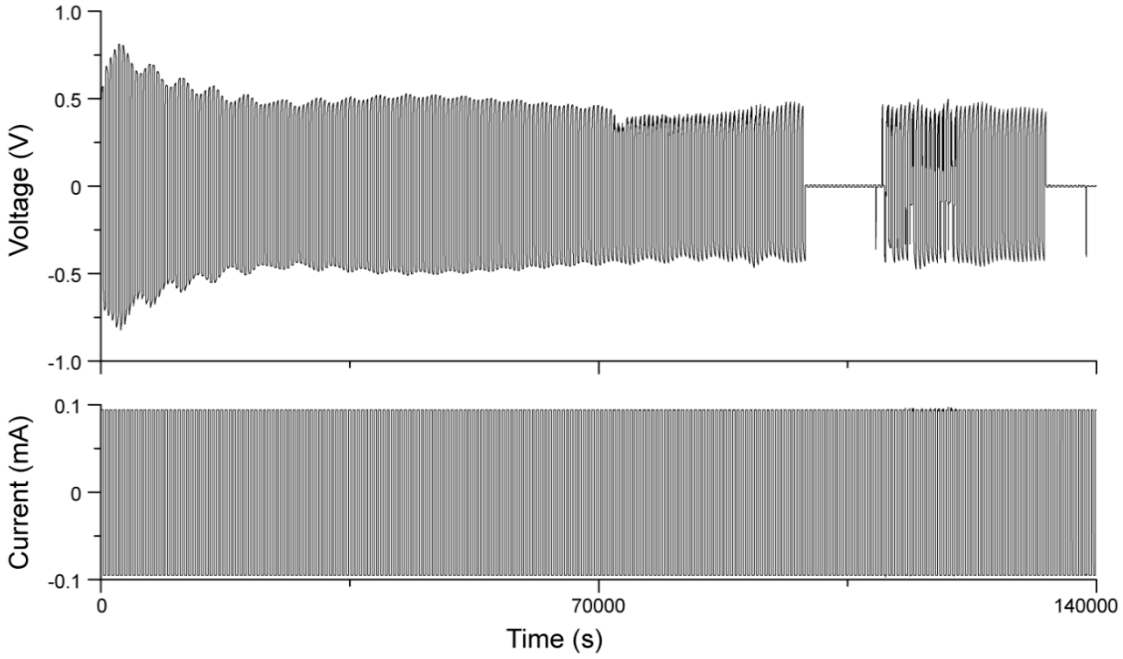

Figure 34. Galvanostatic cycling data of a blank sample (PAN with 33.3 wt% $LiClO_4$), showing the cell voltage and current.

4.4. Conclusions

In summary, CPEs with LLZO NWs as ceramic fillers were fabricated and showed great improvement in the room temperature ionic conductivity of a PAN-based polymer electrolyte to the scale of 10^{-4} S/cm. The optimal mass loading for undoped LLZO NWs was determined to be 5 wt%. Doping of the LLZO did not have a pronounced influence on the ionic conductivity of the CPE, as films containing Al- and Ta-doped LLZO NWs displayed similar conductivity as those with the undoped LLZO NWs. NMR results showed that the presence of LLZO NWs partially altered the PAN polymer matrix, and that Li^+ diffusion occurred preferentially in those modified regions. We also demonstrated that both intrinsic ionic conductivity and NW morphology were required for the filler materials to achieve maximum effectiveness.

V: SUMMARY

It has been demonstrated that electrospinning is very effective in producing NWs made of oxide materials, such as LLTO and LLZO. Pellets made from electrospun LLTO NWs had their density greatly increased over the ones made from LLTO powders synthesized through conventional sol-gel method, which was attributed to the reduced agglomeration brought by the shape and morphology of the NWs. As a result, the Li^+ conductivity was largely improved in the NW-made pellets. Electrospun LLZO NWs enabled the observation of a particle size related phase transformation phenomenon, in which undoped c-LLZO could be stabilized at room temperature when the grain size is below some critical value, and would change back to t-LLZO when the grain grew larger. It was proved preliminarily that this phenomenon is due to the difference in the surface energy of the two polymorphs. LLZO NWs was also incorporated as fillers into a PAN-$LiClO_4$ matrix to form a flexible CPE. The CPE showed the highest ionic conductivity when the added undoped LLZO NWs was at 5 wt%. It was decided that both filler morphology and the intrinsic Li^+ conductivity of the filler were two of the crucial factors to the overall ionic conductivity of the CPE. NMR studies showed that the addition of undoped LLZO NWs modified the interface regions between the fillers and the polymer matrix, and acted as the preferential conduction pathways for Li^+ transport.

REFERENCES

(1) Tarascon, J.-M.; Armand, M. Issues and Challenges Facing Rechargeable Lithium Batteries. *Nature* **2001**, *414*, 359–367.

(2) Whittingham, M. S. Electrical Energy Storage and Intercalation Chemistry. *Science (80-.).* **1976**, *192*, 1126–1127.

(3) Huggins, R. A. Negative Electrodes in Lithium Cells. In *Advanced Batteries: Materials Science Aspects*; Springer US: New York, 2009; pp. 123–149.

(4) Yazami, R.; Touzain, P. A Reversible Graphite-Lithium Negative Electrode for Electrochemical Generators. *J. Power Sources* **1983**, *9*, 365–371.

(5) Mizushima, K.; Jones, P. C.; Wiseman, P. J.; Goodenough, J. B. Li_xCoO_2 ($0<x<1$): A New Cathode Material for Batteries of High Energy Density. *Mater. Res. Bull.* **1980**, *15*, 783–789.

(6) Whittingham, M. S. Lithium Batteries and Cathode Materials. *Chem. Rev.* **2004**, *104*, 4271–4302.

(7) Nagaura, T.; Tozawa, K. Lithium Ion Rechargeable Battery. *Prog. Batter. Sol. Cells* **1990**, *9*, 209.

(8) Arora, P.; Zhang, Z. Battery Separators. *Chem. Rev.* **2004**, *104*, 4419–4462.

(9) Goodenough, J. B.; Kim, Y. Challenges for Rechargeable Li Batteries. *Chem. Mater.* **2010**, *22*, 587–603.

(10) Balakrishnan, P. G.; Ramesh, R.; Prem Kumar, T. Safety Mechanisms in Lithium-Ion Batteries. *J. Power Sources* **2006**, *155*, 401–414.

(11) Dudley, B. Lithium-ion batteries pack a lot of energy — and challenges http://www.seattletimes.com/business/lithium-ion-batteries-pack-a-lot-of-energy-mdash-and-challenges/.

(12) Ivory, D. Federal Safety Agency Ends Its Investigation of Tesla Fires. *The New York Times*, 2014, B4.

(13) Dreamliner: Boeing 787 planes grounded on safety fears http://www.bbc.com/news/business-21054089.

(14) Samsung Expands Recall to All Galaxy Note7 Devices http://www.samsung.com/us/note7recall/ (accessed Oct 13, 2016).

(15) Quartarone, E.; Mustarelli, P. Electrolytes for Solid-State Lithium Rechargeable Batteries: Recent Advances and Perspectives. *Chem. Soc. Rev.* **2011**, *40*, 2525–2540.

(16) Cao, C.; Li, Z.-B.; Wang, X.-L.; Zhao, X.-B.; Han, W.-Q. Recent Advances in Inorganic Solid Electrolytes for Lithium Batteries. *Front. Energy Res.* **2014**, *2*, 1–10.

(17) Chen, R.; Qu, W.; Guo, X.; Li, L.; Wu, F. The Pursuit of Solid-State Electrolytes for Lithium Batteries: From Comprehensive Insight to Emerging Horizons. *Mater. Horiz.* **2016**.

(18) Hayashi, K.; Nemoto, Y.; Tobishima, S.; Yamaki, J. Electrolyte for High Voltage Li/$LiMn_{1.9}Co_{0.1}O_4$ Cells. *J. Power Sources* **1997**, *68*, 316–319.

(19) Knauth, P. Inorganic Solid Li Ion Conductors: An Overview. *Solid State Ionics* **2009**, *180*, 911–916.

(20) Fergus, J. W. Ceramic and Polymeric Solid Electrolytes for Lithium-Ion Batteries. *J. Power Sources* **2010**, *195*, 4554–4569.

(21) Xiang, H.; Chen, J.; Li, Z.; Wang, H. An Inorganic Membrane as a Separator for Lithium-Ion Battery. *J. Power Sources* **2011**, *196*, 8651–8655.

(22) Gaines, L.; Cuenca, R. *Costs of Lithium-Ion Batteries for Vehicles*; 2000.

(23) Daniel, C. Materials and Processing for Lithium-Ion Batteries. *JOM* **2008**, *60*, 43–48.

(24) Dudney, N. J. Glass and Ceramic Electrolytes for Lithium and Lithium-Ion Batteries. In *Lithium Batteries - Science and Technology*; Nazri, G.-A.; Pistoia, G., Eds.; Springer US, 2003; pp. 624–642.

(25) Fergus, J. W. Recent Developments in Cathode Materials for Lithium Ion Batteries. *J. Power Sources* **2010**, *195*, 939–954.

(26) Ren, Y.; Chen, K.; Chen, R.; Liu, T.; Zhang, Y.; Nan, C.-W. Oxide Electrolytes for Lithium Batteries. *J. Am. Ceram. Soc.* **2015**, 1–21.

(27) Manuel Stephan, A.; Nahm, K. S. Review on Composite Polymer Electrolytes for Lithium Batteries. *Polymer (Guildf).* **2006**, *47*, 5952–5964.

(28) Fenton, D. E.; Parker, J. M.; Wright, P. V. Complexes of Alkali Metal Ions with Poly(ethylene Oxide). *Polymer (Guildf).* **1973**, *14*, 589.

(29) Agrawal, R. C.; Pandey, G. P. Solid Polymer Electrolytes: Materials Designing and All-Solid-State Battery Applications: An Overview. *J. Phys. D Appl. Phys.* **2008**, *41*, 223001.

(30) Armand, M. The History of Polymer Electrolytes. *Solid State Ionics* **1994**, *69*, 309–319.

(31) Meyer, W. H. Polymer Electrolytes for Lithium-Ion Batteries. *Adv. Mater.* **1998**, *10*, 439–448.

(32) Kumar, B.; Scanlon, L. G. Polymer-Ceramic Composite Electrolytes. *J. Power Sources* **1994**, *52*, 261–268.

(33) Nairn, K.; Forsyth, M.; Every, H.; Greville, M.; MacFarlane, D. R. Polymer-Ceramic Ion-Conducting Composites. *Solid State Ionics* **1996**, *86–88*, 589–593.

(34) Croce, F.; Appetecchi, G. B.; Persi, L.; Scrosati, B. Nanocomposite Polymer Electrolytes for Lithium Batteries. *Nature* **1998**, *394*, 456–458.

(35) Jayathilaka, P. A. R. D.; Dissanayake, M. A. K. L.; Albinsson, I.; Mellander, B.-E. Effect of Nano-Porous Al_2O_3 on Thermal, Dielectric and Transport Properties of the $(PEO)_9LiTFSI$ Polymer Electrolyte System. *Electrochim. Acta* **2002**, *47*, 3257–3268.

(36) Wieczorek, W.; Florjanczyk, Z.; Stevens, J. R. Composite Polyether Based Solid Electrolytes. *Electrochim. Acta* **1995**, *40*, 2251–2258.

(37) Wieczorek, W.; Stevens, J. R.; Florjańczyk, Z. Composite Polyether Based Solid Electrolytes. The Lewis Acid-Base Approach. *Solid State Ionics* **1996**, *85*, 67–72.

(38) Croce, F.; Curini, R.; Martinelli, A.; Persi, L.; Ronci, F.; Scrosati, B.; Caminiti, R. Physical and Chemical Properties of Nanocomposite Polymer Electrolytes. *J. Phys. Chem. B* **1999**, *103*, 10632–10638.

(39) Croce, F.; Persi, L. L.; Scrosati, B.; Serraino-Fiory, F.; Plichta, E.; Hendrickson, M. A. Role of the Ceramic Fillers in Enhancing the Transport Properties of Composite Polymer Electrolytes. *Electrochim. Acta* **2001**, *46*, 2457–2461.

(40) Huggins, R. A. Simple Method to Determine Electronic and Ionic Components of the Conductivity in Mixed Conductors A Review. *Ionics (Kiel).* **2002**, *8*, 300–313.

(41) Yao, X.; Huang, B.; Yin, J.; Peng, G.; Huang, Z.; Gao, C.; Liu, D.; Xu, X. All-Solid-State Lithium Batteries with Inorganic Solid Electrolytes: Review of Fundamental Science. *Chin. Phys. B* **2016**, *25*, 18802.

(42) Bachman, J. C.; Muy, S.; Grimaud, A.; Chang, H.-H.; Pour, N.; Lux, S. F.; Paschos, O.; Maglia, F.; Lupart, S.; Lamp, P.; *et al.* Inorganic Solid-State Electrolytes for Lithium Batteries: Mechanisms and Properties Governing Ion Conduction. *Chem. Rev.* **2016**, *116*, 140–162.

(43) Chen-Yang, Y. W.; Chen, H. C.; Lin, F. J.; Chen, C. C. Polyacrylonitrile Electrolytes: 1. A Novel High-Conductivity Composite Polymer Electrolyte Based on PAN, $LiClO_4$ and α-Al_2O_3. *Solid State Ionics* **2002**, *150*, 327–335.

(44) Yang, C. R.; Perng, J. T.; Wang, Y. Y.; Wan, C. C. Conductive Behaviour of Lithium Ions in Polyacrylonitrile. *J. Power Sources* **1996**, *62*, 89–93.

(45) Liu, W.; Liu, N.; Sun, J.; Hsu, P.-C.; Li, Y.; Lee, H.-W.; Cui, Y. Ionic Conductivity Enhancement of Polymer Electrolytes with Ceramic Nanowire

Fillers. *Nano Lett.* **2015**, *15*, 2740–2745.

(46) Cheng, L.; Crumlin, E. J.; Chen, W.; Qiao, R.; Hou, H.; Franz Lux, S.; Zorba, V.; Russo, R.; Kostecki, R.; Liu, Z.; *et al.* The Origin of High Electrolyte-Electrode Interfacial Resistances in Lithium Cells Containing Garnet Type Solid Electrolytes. *Phys. Chem. Chem. Phys.* **2014**, *16*, 18294–18300.

(47) Cheng, L.; Chen, W.; Kunz, M.; Persson, K.; Tamura, N.; Chen, G.; Doeff, M. Effect of Surface Microstructure on Electrochemical Performance of Garnet Solid Electrolytes. *ACS Appl. Mater. Interfaces* **2015**, *7*, 2073–2081.

(48) Chen, R.-J.; Huang, M.; Huang, W.-Z.; Shen, Y.; Lin, Y.-H.; Nan, C.-W. Sol–gel Derived Li–La–Zr–O Thin Films as Solid Electrolytes for Lithium-Ion Batteries. *J. Mater. Chem. A* **2014**, *2*, 13277–13282.

(49) Zheng, J.; Tang, M.; Hu, Y.-Y. Lithium Ion Pathway within $Li_7La_3Zr_2O_{12}$ - Polyethylene Oxide Composite Electrolytes. *Angew. Chem.* **2016**, *128*, 12726–12730.

(50) Richards, W. D.; Miara, L. J.; Wang, Y.; Kim, J. C.; Ceder, G. Interface Stability in Solid-State Batteries. *Chem. Mater.* **2016**, *28*, 266–273.

(51) Yu, S.; Schmidt, R. D.; Garcia-Mendez, R.; Herbert, E.; Dudney, N. J.; Wolfenstine, J. B.; Sakamoto, J.; Siegel, D. J. Elastic Properties of the Solid Electrolyte $Li_7La_3Zr_2O_{12}$ (LLZO). *Chem. Mater.* **2016**, *28*, 197–206.

(52) Gauthier, M.; Carney, T. J.; Grimaud, A.; Giordano, L.; Pour, N.; Chang, H.-H.; Fenning, D. P.; Lux, S. F.; Paschos, O.; Bauer, C.; *et al.* The Electrode-Electrolyte Interface in Li-Ion Batteries: Current Understanding and New Insights. *J. Phys. Chem. Lett.* **2015**, *6*, 4653–4672.

(53) Anikeeva, P. O.; Halpert, J. E.; Bawendi, M. G.; Bulović, V. Quantum Dot Light-Emitting Devices with Electroluminescence Tunable over the Entire Visible Spectrum. *Nano Lett.* **2009**, *9*, 2532–2536.

(54) Shirasaki, Y.; Supran, G. J.; Bawendi, M. G.; Bulović, V. Emergence of Colloidal Quantum-Dot Light-Emitting Technologies. *Nat. Photonics* **2012**, *7*, 13–23.

(55) Huang, X.; El-Sayed, M. A. Gold Nanoparticles: Optical Properties and Implementations in Cancer Diagnosis and Photothermal Therapy. *J. Adv. Res.* **2010**, *1*, 13–28.

(56) Guo, D.; Xie, G.; Luo, J. Mechanical Properties of Nanoparticles: Basics and Applications. *J. Phys. D. Appl. Phys.* **2014**, *47*, 13001.

(57) Aricò, A. S.; Bruce, P.; Scrosati, B.; Tarascon, J.-M.; van Schalkwijk, W. Nanostructured Materials for Advanced Energy Conversion and Storage Devices. *Nat. Mater.* **2005**, *4*, 366–377.

(58) Chiang, Y.-M.; Lavik, E. B.; Kosacki, I.; Tuller, H. L.; Ying, J. Y. Nonstoichiometry and Electrical Conductivity of Nanocrystalline CeO_{2-x}. *J. Electroceramics* **1997**, *1*, 7–14.

(59) Kim, S.; Fleig, J.; Maier, J. Space Charge Conduction: Simple Analytical Solutions for Ionic and Mixed Conductors and Application to Nanocrystalline Ceria. *Phys. Chem. Chem. Phys.* **2003**, *5*, 2268–2273.

(60) Tenhaeff, W. E.; Rangasamy, E.; Wang, Y.; Sokolov, A. P.; Wolfenstine, J.; Sakamoto, J.; Dudney, N. J. Resolving the Grain Boundary and Lattice Impedance of Hot-Pressed $Li_7La_3Zr_2O_{12}$ Garnet Electrolytes. *ChemElectroChem* **2014**, *1*, 375–378.

(61) Sakamoto, J.; Rangasamy, E.; Kim, H.; Kim, Y.; Wolfenstine, J. Synthesis of Nano-Scale Fast Ion Conducting Cubic $Li_7La_3Zr_2O_{12}$. *Nanotechnology* **2013**, *24*, 424005.

(62) Chan, C. K.; Peng, H.; Twesten, R. D.; Jarausch, K.; Zhang, X. F.; Cui, Y. Fast, Completely Reversible Li Insertion in Vanadium Pentoxide Nanoribbons. *Nano Lett.* **2007**, *7*, 490–495.

(63) Chan, C. K.; Peng, H.; Liu, G.; McIlwrath, K.; Zhang, X. F.; Huggins, R. A.; Cui, Y. High-Performance Lithium Battery Anodes Using Silicon Nanowires. *Nat. Nanotechnol.* **2008**, *3*, 31–35.

(64) Chan, C. K.; Zhang, X. F.; Cui, Y. High Capacity Li Ion Battery Anodes Using Ge Nanowires. *Nano Lett.* **2008**, *8*, 307–309.

(65) Chan, C. K.; Patel, R. N.; O'Connell, M. J.; Korgel, B. A.; Cui, Y. Solution-Grown Silicon Nanowires for Lithium-Ion Battery Anodes. *ACS Nano* **2010**, *4*, 1443–1450.

(66) Fu, K. (Kelvin); Gong, Y.; Dai, J.; Gong, A.; Han, X.; Yao, Y.; Wang, C.; Wang, Y.; Chen, Y.; Yan, C.; *et al.* Flexible, Solid-State, Ion-Conducting Membrane with 3D Garnet Nanofiber Networks for Lithium Batteries. *P. Natl. Acad. Sci. USA* **2016**, *113*, 7094–7099.

(67) *Impedance Spectroscopy Theory, Experiment, and Applications*; Barsoukov, E.; MacDonald, J. R., Eds.; 2nd ed.; John Wiley & Sons, Inc.: Hoboken, NJ, 2005.

(68) Van Dijk, T.; Burggraaf, A. J. Grain Boundary Effects on Ionic Conductivity in Ceramic $Gd_xZr_{1-x}O_{2-(x/2)}$ Solid Solutions. *Phys. Status Solidi* **1981**, *63*, 229–240.

(69) Verkerk, M. J.; Middelhuis, B. J.; Burggraaf, A. J. Effect of Grain Boundaries on the Conductivity of High-Purity ZrO_2-Y_2O_3 Ceramics. *Solid State Ionics* **1982**, *6*, 159–170.

(70) Haile, S. M.; West, D. L.; Campbell, J. The Role of Microstructure and Processing on the Proton Conducting Properties of Gadolinium-Doped Barium Cerate. *J.*

Mater. Res. **1998**, *13*, 1576–1595.

(71) KINGERY, W. D. Plausible Concepts Necessary and Sufficient for Interpretation of Ceramic Grain-Boundary Phenomena: I, Grain-Boundary Characteristics, Structure, and Electrostatic Potential. *J. Am. Ceram. Soc.* **1974**, *57*, 1–8.

(72) KINGERY, W. D. Plausible Concepts Necessary and Sufficient for Interpretation of Ceramic Grain-Boundary Phenomena: II, Solute Segregation, Grain-Boundary Diffusion, and General Discussion*. *J. Am. Ceram. Soc.* **1974**, *57*, 74–83.

(73) Bauerle, J. E. Study of Solid Electrolyte Polarization by a Complex Admittance Method. *J. Phys. Chem. Solids* **1969**, *30*, 2657–2670.

(74) Armstrong, R. D.; Dickinson, T.; Willis, P. M. The A.C. Impedance of Powdered and Sintered Solid Ionic Conductors. *J. Electroanal. Chem. Interfacial Electrochem.* **1974**, *53*, 389–405.

(75) Ho, C.; Raistrick, I. D.; Huggins, R. A. Application of A-C Techniques to the Study of Lithium Diffusion in Tungsten Trioxide Thin Films. *J. Electrochem. Soc.* **1980**, *127*, 343.

(76) Li, D.; Xia, Y. Electrospinning of Nanofibers: Reinventing the Wheel? *Adv. Mater.* **2004**, *16*, 1151–1170.

(77) Boys, C. V. On the Production, Properties, and Some Suggested Uses of the Finest Threads. *Proc. Phys. Soc. London* **1887**, *9*, 8–19.

(78) Taylor, G. Disintegration of Water Drops in an Electric Field. *Proc. Roy. Soc. Lond. A* **1964**, *280*, 383–397.

(79) Taylor, G. The Force Exerted by an Electric Field on a Long Cylindrical Conductor. *Proc. Roy. Soc. Lond. A* **1966**, *291*, 145–158.

(80) Taylor, G. Electrically Driven Jets. *Proc. Roy. Soc. Lond. A* **1969**, *313*, 453–475.

(81) Li, D.; Xia, Y. Fabrication of Titania Nanofibers by Electrospinning. *Nano Lett.* **2003**, *3*, 555–560.

(82) Stramare, S.; Thangadurai, V.; Weppner, W. Lithium Lanthanum Titanates: A Review. *Chem. Mater.* **2003**, *15*, 3974–3990.

(83) Inaguma, Y.; Chen, L.; Itoh, M.; Nakamura, T.; Uchida, T.; Ikuta, H.; Wakihara, M. High Ionic Conductivity in Lithium Lanthanum Titanate. *Solid State Commun.* **1993**, *86*, 689–693.

(84) Weppner, W.; Huggins, R. A. Determination of the Kinetic Parameters of Mixed-Conducting Electrodes and Application to the System Li3Sb. *J. Electrochem. Soc.* **1977**, *124*, 1569–1578.

(85) Dokko, K.; Akutagawa, N.; Isshiki, Y.; Hoshina, K.; Kanamura, K. Preparation of

Three Dimensionally Ordered Macroporous LiLaTiO by Colloidal Crystal Templating Process. *Solid State Ionics* **2005**, *176*, 2345–2348.

(86) Wöhrle, T.; Gómez-Romero, P.; Fries, T.; West, K.; Palacín, M. R.; Casañ-Pastor, N. Sol-Gel Synthesis of the Lithium-Ion Conducting Perovskite $La_{0.57}Li_{0.3}TiO_3$ Effect of Synthesis and Thermal Treatments on the Structure and Conducting Properties. *Ionics (Kiel).* **1996**, *2*, 442–445.

(87) Fourquet, J. L.; Duroy, H.; Crosnier-Lopez, M. P. Structural and Microstructural Studies of the Series $La_{2/3-x}Li_{3x}\square_{1/3-2x}TiO_3$. *J. Solid State Chem.* **1996**, *127*, 283–294.

(88) Ibarra, J.; Várez, A.; León, C.; Santamaría, J.; Torres-Martínez, L. M.; Sanz, J. Influence of Composition on the Structure and Conductivity of the Fast Ionic Conductors $La_{2/3-x}Li_{3x}TiO_3$ ($0.03 \leq x \leq 0.167$). *Solid State Ionics* **2000**, *134*, 219–228.

(89) Bohnke, C.; Regrag, B.; Le Berre, F.; Fourquet, J.-L.; Randrianantoandro, N. Comparison of pH Sensitivity of Lithium Lanthanum Titanate Obtained by Sol-Gel Synthesis and Solid State Chemistry. *Solid State Ionics* **2005**, *176*, 73–80.

(90) Kitaoka, K.; Kozuka, H.; Hashimoto, T.; Yoko, T. Preparation of $La_{0.5}Li_{0.5}TiO_3$ Perovskite Thin Films by the Sol-Gel Method. *J. Mater. Sci.* **1997**, *32*, 2063–2070.

(91) Bohnke, O.; Emery, J.; Fourquet, J.-L. Anomalies in Li^+ Ion Dynamics Observed by Impedance Spectroscopy and ^7Li NMR in the Perovskite Fast Ion Conductor $(Li_{3x}La_{2/3-x}\square_{1/3-2x})TiO_3$. *Solid State Ionics* **2003**, *158*, 119–132.

(92) Ban, C. W.; Choi, G. M. The Effect of Sintering on the Grain Boundary Conductivity of Lithium Lanthanum Titanates. *Solid State Ionics* **2001**, *140*, 285–292.

(93) Yang, K.-Y.; Wang, J.-W.; Fung, K.-Z. Roles of Lithium Ions and La/Li-Site Vacancies in Sinterability and Total Ionic Conduction Properties of Polycrystalline $Li_{3x}La_{2/3-x}TiO_3$ Solid Electrolytes ($0.21 \leq 3x \leq 0.50$). *J. Alloys Compd.* **2008**, *458*, 415–424.

(94) Inaguma, Y.; Chen, L.; Itoh, M.; Nakamura, T. Candidate Compounds with Perovskite Structure for High Lithium Ionic Conductivity. *Solid State Ionics* **1994**, *70–71*, 196–202.

(95) Kawai, H.; Kuwano, J. Lithium Ion Conductivity of A-Site Deficient Perovskite Solid Solution $La_{0.67-x}Li_{3x}TiO_3$. *J. Electrochem. Soc.* **1994**, *141*, 78–79.

(96) Harada, Y.; Ishigaki, T.; Kawai, H.; Kuwano, J. Lithium Ion Conductivity of Polycrystalline Perovskite $La_{0.67-x}Li_{3x}TiO_3$ with Ordered and Disordered Arrangements of the A-Site Ions. *Solid State Ionics* **1998**, *108*, 407–413.

(97) Birke, P.; Scharner, S.; Huggins, R. A.; Weppner, W. Electrolytic Stability Limit

and Rapid Lithium Insertion in the Fast-Ion-Conducting $Li_{0.29}La_{0.57}TiO_3$ Perovskite-Type Compound. *J. Electrochem. Soc.* **1997**, *144*, 167–169.

(98) Wolfenstine, J.; Allen, J. L.; Read, J.; Sakamoto, J.; Gonalez-Doncel, G. Hot-Pressed $Li_{0.33}La_{0.57}TiO_3$. *J. Power Sources* **2010**, *195*, 4124–4128.

(99) Milian Pila, C. R.; Otero, T. M.; Pérez Cappe, E.; Alves, O. L.; Aranda, P.; Frutis, M. A.; Laffita, Y. M. Influence of Citrate/nitrate Ratio on the Preparation of $Li_{0.5}La_{0.5}TiO_3$ Nanopowder by Combustion Method. *Ceram. Int.* **2014**, *40*, 249–256.

(100) Geng, H. X.; Mei, A.; Dong, C.; Lin, Y. H.; Nan, C. W. Investigation of Structure and Electrical Properties of $Li_{0.5}La_{0.5}TiO_3$ Ceramics via Microwave Sintering. *J. Alloys Compd.* **2009**, *481*, 555–558.

(101) Mayo, M. J. Processing of Nanocrystalline Ceramics from Ultrafine Particles. *Int. Mater. Rev.* **1996**, *41*, 85–115.

(102) Groza, J. R.; Dowding, R. J. Nanoparticulate Materials Densification. *NanoStructured Mater.* **1996**, *7*, 749–768.

(103) Fang, Z. Z.; Wang, H. Densification and Grain Growth during Sintering of Nanosized Particles. *Int. Mater. Rev.* **2008**, *53*, 326–352.

(104) Lu, K. Sintering of Nanoceramics. *Int. Mater. Rev.* **2008**, *53*, 21–38.

(105) Hou, L.; Hou, Y.-D.; Song, X.-M.; Zhu, M.-K.; Wang, H.; Yan, H. Sol-Gel-Hydrothermal Synthesis and Sintering of $K_{0.5}Bi_{0.5}TiO_3$ Nanowires. *Mater. Res. Bull.* **2006**, *41*, 1330–1336.

(106) Hou, Y.-D.; Hou, L.; Zhang, T.-T.; Zhu, M.-K.; Wang, H.; Van, H. $(Na_{0.8}K_{0.2})_{0.5}Bi_{0.5}TiO_3$ Nanowires: Low-Temperature Sol–Gel–Hydrothermal Synthesis and Densification. In *Progress in Nanotechnology*; John Wiley & Sons, Inc.: Hoboken, NJ, USA, 2009; pp. 305–310.

(107) Wolfenstine, J.; Rangasamy, E.; Allen, J. L.; Sakamoto, J. High Conductivity of Dense Tetragonal $Li_7La_3Zr_2O_{12}$. *J. Power Sources* **2012**, *208*, 193–196.

(108) Hou, Y.-D.; Hou, L.; Zhao, J.-L.; Zhu, M.-K.; Yan, H. Lead-Free Bi-Based Complex Perovskite Nanowires: Sol-Gel-Hydrothermal Processing and the Densification Behavior. *J. Electroceramics* **2011**, *26*, 37–43.

(109) Thangadurai, V.; Kaack, H.; Weppner, W. J. F. Novel Fast Lithium Ion Conduction in Garnet-Type $Li_5La_3M_2O_{12}$ (M=Nb, Ta). *J. Am. Ceram. Soc.* **2003**, *86*, 437–440.

(110) Murugan, R.; Thangadurai, V.; Weppner, W. Fast Lithium Ion Conduction in Garnet-Type $Li_7La_3Zr_2O_{12}$. *Angew. Chem. Int. Ed.* **2007**, *46*, 7778–7781.

(111) Cussen, E. J. Structure and Ionic Conductivity in Lithium Garnets. *J. Mater. Chem.* **2010**, *20*, 5167–5173.

(112) Thangadurai, V.; Adams, S.; Weppner, W. Crystal Structure Revision and Identification of Li^+-Ion Migration Pathways in the Garnet-like $Li_5La_3M_2O_{12}$ (M = Nb, Ta) Oxides. *Chem. Mater.* **2004**, *16*, 2998–3006.

(113) Geiger, C. A.; Alekseev, E.; Lazic, B.; Fisch, M.; Armbruster, T.; Langner, R.; Fechtelkord, M.; Kim, N.; Pettke, T.; Weppner, W. Crystal Chemistry and Stability of "$Li_7La_3Zr_2O_{12}$" garnet: A Fast Lithium-Ion Conductor. *Inorg. Chem.* **2011**, *50*, 1089–1097.

(114) Matsui, M.; Takahashi, K.; Sakamoto, K.; Hirano, A.; Takeda, Y.; Yamamoto, O.; Imanishi, N. Phase Stability of a Garnet-Type Lithium Ion Conductor $Li_7La_3Zr_2O_{12}$. *Dalt. Trans.* **2014**, *43*, 1019–1024.

(115) Logéat, A.; Köhler, T.; Eisele, U.; Stiaszny, B.; Harzer, A.; Tovar, M.; Senyshyn, A.; Ehrenberg, H.; Kozinsky, B. From Order to Disorder: The Structure of Lithium-Conducting Garnets $Li_{7-x}La_3Ta_xZr_{2-x}O_{12}$ (x=0–2). *Solid State Ionics* **2012**, *206*, 33–38.

(116) Ohta, S.; Kobayashi, T.; Asaoka, T. High Lithium Ionic Conductivity in the Garnet-Type Oxide $Li_{7-X}La_3(Zr_{2-X}, Nb_X)O_{12}$ (X = 0-2). *J. Power Sources* **2011**, *196*, 3342–3345.

(117) Bernstein, N.; Johannes, M. D.; Hoang, K. Origin of the Structural Phase Transition in $Li_7La_3Zr_2O_{12}$. *Phys. Rev. Lett.* **2012**, *109*, 205702.

(118) Rangasamy, E.; Wolfenstine, J.; Sakamoto, J. The Role of Al and Li Concentration on the Formation of Cubic Garnet Solid Electrolyte of Nominal Composition $Li_7La_3Zr_2O_{12}$. *Solid State Ionics* **2012**, *206*, 28–32.

(119) Buschmann, H.; Berendts, S.; Mogwitz, B.; Janek, J. Lithium Metal Electrode Kinetics and Ionic Conductivity of the Solid Lithium Ion Conductors "$Li_7La_3Zr_2O_{12}$" and $Li_{7-x}La_3Zr_{2-x}Ta_xO_{12}$ with Garnet-Type Structure. *J. Power Sources* **2012**, *206*, 236–244.

(120) Wang, Y.; Lai, W. High Ionic Conductivity Lithium Garnet Oxides of $Li_{7-x}La_3Zr_{2-x}Ta_xO_{12}$ Compositions. *Electrochem. Solid-State Lett.* **2012**, *15*, A68–A71.

(121) Awaka, J.; Kijima, N.; Hayakawa, H.; Akimoto, J. Synthesis and Structure Analysis of Tetragonal $Li_7La_3Zr_2O_{12}$ with the Garnet-Related Type Structure. *J. Solid State Chem.* **2009**, *182*, 2046–2052.

(122) Cussen, E. J. The Structure of Lithium Garnets: Cation Disorder and Clustering in a New Family of Fast Li^+ Conductors. *Chem. Commun.* **2006**, 412–413.

(123) Percival, J.; Kendrick, E.; Smith, R. I.; Slater, P. R. Cation Ordering in Li

Containing Garnets: Synthesis and Structural Characterisation of the Tetragonal System, $Li_7La_3Sn_2O_{12}$. *Dalt. Trans.* **2009**, 5177–5181.

(124) Jalem, R.; Yamamoto, Y.; Shiiba, H.; Nakayama, M.; Munakata, H.; Kasuga, T.; Kanamura, K. Concerted Migration Mechanism in the Li Ion Dynamics of Garnet-Type $Li_7La_3Zr_2O_{12}$. *Chem. Mater.* **2013**, *25*, 425–430.

(125) Meier, K.; Laino, T.; Curioni, A. Solid-State Electrolytes: Revealing the Mechanisms of Li-Ion Conduction in Tetragonal and Cubic LLZO by First-Principles Calculations. *J. Phys. Chem. C* **2014**, *118*, 6668–6679.

(126) Kokal, I.; Somer, M.; Notten, P. H. L.; Hintzen, H. T. Sol–gel Synthesis and Lithium Ion Conductivity of $Li_7La_3Zr_2O_{12}$ with Garnet-Related Type Structure. *Solid State Ionics* **2011**, *185*, 42–46.

(127) Janani, N.; Ramakumar, S.; Dhivya, L.; Deviannapoorani, C.; Saranya, K.; Murugan, R. Synthesis of Cubic $Li_7La_3Zr_2O_{12}$ by Modified Sol-Gel Process. *Ionics (Kiel).* **2011**, *17*, 575–580.

(128) Toda, S.; Ishiguro, K.; Shimonishi, Y.; Hirano, a.; Takeda, Y.; Yamamoto, O.; Imanishi, N. Low Temperature Cubic Garnet-Type CO_2-Doped $Li_7La_3Zr_2O_{12}$. *Solid State Ionics* **2013**, *233*, 102–106.

(129) Larraz, G.; Orera, A.; Sanjuán, M. L. Cubic Phases of Garnet-Type $Li_7La_3Zr_2O_{12}$: The Role of Hydration. *J. Mater. Chem. A* **2013**, *1*, 11419–11428.

(130) Davies, E.; Lowe, A.; Sterns, M.; Fujihara, K.; Ramakrishna, S. Phase Morphology in Electrospun Zirconia Microfibers. *J. Am. Ceram. Soc.* **2008**, *91*, 1115–1120.

(131) Xie, H.; Li, Y.; Goodenough, J. B. Low-Temperature Synthesis of $Li_7La_3Zr_2O_{12}$ with Cubic Garnet-Type Structure. *Mater. Res. Bull.* **2012**, *47*, 1229–1232.

(132) Thompson, T.; Wolfenstine, J.; Allen, J. L.; Johannes, M.; Huq, A.; David, I. N.; Sakamoto, J. Tetragonal *vs.* Cubic Phase Stability in Al-Free Ta Doped $Li_7La_3Zr_2O_{12}$ (LLZO). *J. Mater. Chem. A* **2014**, *2*, 13431–13436.

(133) Filipovich, V. N.; Kalinina, A. M. Critical Amorphization Radius of Crystals. *Struct. Glas.* **1965**, *5*, 34.

(134) Garvie, R. C. Stabilization of the Tetragonal Structure in Zirconia Microcrystals. *J. Phys. Chem.* **1978**, *82*, 218–224.

(135) Hanaor, D. A. H.; Sorrell, C. C. Review of the Anatase to Rutile Phase Transformation. *J. Mater. Sci.* **2011**, *46*, 855–874.

(136) Gribb, A. A.; Banfield, J. F. Particle Size Effects on Transformation Kinetics and Phase Stability in Nanocrystalline TiO_2. *Am. Mineral.* **1997**, *82*, 717–728.

(137) Hu, Y.; Tsai, H.-L.; Huang, C.-L. Phase Transformation of Precipitated TiO_2 Nanoparticles. *Mater. Sci. Eng. A* **2003**, *344*, 209–214.

(138) Zhang, H.; Banfield, J. F. Thermodynamic Analysis of Phase Stability of Nanocrystalline Titania. *J. Mater. Chem.* **1998**, *8*, 2073–2076.

(139) Garvie, R. C. The Occurrence of Metastable Tetragonal Zirconia as a Crystallite Size Effect. *J. Phys. Chem.* **1964**, *69*, 1238–1243.

(140) Chraska, T.; King, A. H.; Berndt, C. C. On the Size-Dependent Phase Transformation in Nanoparticulate Zirconia. *Mater. Sci. Eng. A* **2000**, *A286*, 169–178.

(141) Baldinozzi, G.; Simeone, D.; Gosset, D.; Dutheil, M. Neutron Diffraction Study of the Size-Induced Tetragonal to Monoclinic Phase Transition in Zirconia Nanocrystals. *Phys. Rev. Lett.* **2003**, *90*, 216103.

(142) Hubaud, A. A.; Schroeder, D. J.; Key, B.; Ingram, B. J.; Dogan, F.; Vaughey, J. T. Low Temperature Stabilization of Cubic $(Li_{7-x}Al_{x/3})La_3Zr_2O_{12}$: Role of Aluminum during Formation. *J. Mater. Chem. A* **2013**, *1*, 8813–8818.

(143) Kaeriyama, A.; Munakata, H.; Kajihara, K.; Kanamura, K.; Sato, Y.; Yoshida, T. Evaluation of Electrochemical Characteristics of $Li_7La_3Zr_2O_{12}$ Solid Electrolyte. *ECS Trans.* **2009**, *16*, 175–180.

(144) Shimonishi, Y.; Toda, A.; Zhang, T.; Hirano, A.; Imanishi, N.; Yamamoto, O.; Takeda, Y. Synthesis of Garnet-Type $Li_{7-x}La_3Zr_2O_{12-1/2x}$ and Its Stability in Aqueous Solutions. *Solid State Ionics* **2011**, *183*, 48–53.

(145) Teng, S.; Tan, J.; Tiwari, A. Recent Developments in Garnet Based Solid State Electrolytes for Thin Film Batteries. *Curr. Opin. Solid State Mater. Sci.* **2014**, *18*, 29–38.

(146) Chen, I.-W.; Wang, X.-H. Sintering Dense Nanocrystalline Ceramics without Final-Stage Grain Growth. *Nature* **2000**, *404*, 168–171.

(147) Zhang, G.; Kirk, B.; Jauregui, L. A.; Yang, H.; Xu, X.; Chen, Y. P.; Wu, Y. Rational Synthesis of Ultrathin N-Type Bi_2Te_3 Nanowires with Enhanced Thermoelectric Properties. *Nano Lett.* **2012**, *12*, 56–60.

(148) Seabaugh, M. M.; Kerscht, I. H.; Messing, G. L. Texture Development by Templated Grain Growth in Liquid-Phase-Sintered Alpha-Alumina. *J. Am. Ceram. Soc.* **1997**, *80*, 1181–1188.

(149) Kim, I.-D.; Rothschild, A.; Lee, B. H.; Kim, D. Y.; Jo, S. M.; Tuller, H. L. Ultrasensitive Chemiresistors Based on Electrospun TiO_2 Nanofibers. *Nano Lett.* **2006**, *6*, 2009–2013.

(150) Ohta, S.; Kobayashi, T.; Seki, J.; Asaoka, T. Electrochemical Performance of an

All-Solid-State Lithium Ion Battery with Garnet-Type Oxide Electrolyte. *J. Power Sources* **2012**, *202*, 332–335.

(151) McCloskey, B. D. Attainable Gravimetric and Volumetric Energy Density of Li-S and Li Ion Battery Cells with Solid Separator-Protected Li Metal Anodes. *J. Phys. Chem. Lett.* **2015**, *6*, 4581–4588.

(152) Girishkumar, G.; McCloskey, B.; Luntz, A. C.; Swanson, S.; Wilcke, W. Lithium-Air Battery: Promise and Challenges. *J. Phys. Chem. Lett.* **2010**, *1*, 2193–2203.

(153) Przyluski, J.; Siekierski, M.; Wieczorek, W. Effective Medium Theory in Studies of Conductivity of Composite Polymeric Electrolytes. *Electrochim. Acta* **1995**, *40*, 2101–2108.

(154) Jiang, S.; Wagner, J. B. A Theoretical Model for Composite electrolytes—I. Space Charge Layer as a Cause for Charge-Carrier Enhancement. *J. Phys. Chem. Solids* **1995**, *56*, 1101–1111.

(155) Kim, J.-W.; Ji, K.-S.; Lee, J.-P.; Park, J.-W. Electrochemical Characteristics of Two Types of PEO-Based Composite Electrolyte with Functional SiO_2. *J. Power Sources* **2003**, *119–121*, 415–421.

(156) Yang, T.; Li, Y.; Chan, C. K. Enhanced Lithium Ion Conductivity in Lithium Lanthanum Titanate Solid Electrolyte Nanowires Prepared by Electrospinning. *J. Power Sources* **2015**, *287*, 164–169.

(157) Yang, T.; Gordon, Z. D.; Li, Y.; Chan, C. K. Nanostructured Garnet-Type Solid Electrolytes for Lithium Batteries: Electrospinning Synthesis of $Li_7La_3Zr_2O_{12}$ Nanowires and Particle Size-Dependent Phase Transformation. *J. Phys. Chem. C* **2015**, *119*, 14947–14953.

(158) Gordon, Z. D.; Yang, T.; Gomes Morgado, G. B.; Chan, C. K. Preparation of Nano- and Microstructured Garnet $Li_7La_3Zr_2O_{12}$ Solid Electrolytes for Li-Ion Batteries *via* Cellulose Templating. *ACS Sustain. Chem. Eng.* **2016**.

(159) Allen, J. L.; Wolfenstine, J.; Rangasamy, E.; Sakamoto, J. Effect of Substitution (Ta, Al, Ga) on the Conductivity of $Li_7La_3Zr_2O_{12}$. *J. Power Sources* **2012**, *206*, 315–319.

(160) Adams, S.; Rao, R. P. Ion Transport and Phase Transition in $Li_{7-x}La_3(Zr_{2-x}M_x)O_{12}$ ($M = Ta^{5+}$, Nb^{5+}, $X = 0$, 0.25). *J. Mater. Chem.* **2012**, *22*, 1426.

(161) Miara, L. J.; Ong, S. P.; Mo, Y.; Richards, W. D.; Park, Y.; Lee, J.-M.; Lee, H. S.; Ceder, G. Effect of Rb and Ta Doping on the Ionic Conductivity and Stability of the Garnet $Li_{7+2x-y}(La_{3-x}Rb_x)(Zr_{2-y}Ta_y)O_{12}$ ($0 \leq x \leq 0.375$, $0 \leq y \leq 1$) Superionic Conductor: A First Principles Investigation. *Chem. Mater.* **2013**, *25*, 3048–3055.

(162) Buschmann, H.; Dölle, J.; Berendts, S.; Kuhn, A.; Bottke, P.; Wilkening, M.; Heitjans, P.; Senyshyn, A.; Ehrenberg, H.; Lotnyk, A.; *et al.* Structure and

Dynamics of the Fast Lithium Ion conductor "$Li_7La_3Zr_2O_{12}$." *Phys. Chem. Chem. Phys.* **2011**, *13*, 19378–19392.

(163) Zhang, Y.; Chen, F.; Tu, R.; Shen, Q.; Zhang, X.; Zhang, L. Effect of Lithium Ion Concentration on the Microstructure Evolution and Its Association with the Ionic Conductivity of Cubic Garnet-Type Nominal $Li_7Al_{0.25}La_3Zr_2O_{12}$ Solid Electrolytes. *Solid State Ionics* **2015**, 8–15.

(164) Qian, X.; Gu, N.; Cheng, Z.; Yang, X.; Wang, E. Impedance Study of $(PEO)_{10}LiClO_4$-Al_2O_3 Composite Polymer Electrolyte with Blocking Electrodes. *Electrochim. Acta* **2001**, *46*, 1829–1836.

(165) Wang, Y.-J.; Pan, Y.; Kim, D. Conductivity Studies on Ceramic $Li_{1.3}Al_{0.3}Ti_{1.7}(PO_4)_3$-Filled PEO-Based Solid Composite Polymer Electrolytes. *J. Power Sources* **2006**, *159*, 690–701.

(166) Huang, B.; Wang, Z.; Li, G.; Huang, H.; Xue, R.; Chen, L.; Wang, F. Lithium Ion Conduction in Polymer Electrolytes Based on PAN. *Solid State Ionics* **1996**, *85*, 79–84.

(167) Huang, B.; Wang, Z.; Chen, L.; Xue, R.; Wang, F. The Mechanism of Lithium Ion Transport in Polyacrylonitrile-Based Polymer Electrolytes. *Solid State Ionics* **1996**, *91*, 279–284.

(168) Golodnitsky, D.; Strauss, E.; Peled, E.; Greenbaum, S. Review—On Order and Disorder in Polymer Electrolytes. *J. Electrochem. Soc.* **2015**, *162*, A2551–A2566.

(169) Rettenwander, D.; Welzl, A.; Cheng, L.; Fleig, J.; Musso, M.; Suard, E.; Doeff, M. M.; Redhammer, G. J.; Amthauer, G. Synthesis, Crystal Chemistry, and Electrochemical Properties of $Li_{7-2x}La_3Zr_{2-x}Mo_xO_{12}$ (X = 0.1–0.4): Stabilization of the Cubic Garnet Polymorph *via* Substitution of Zr^{4+} by Mo^{6+}. *Inorg. Chem.* **2015**, *54*, 10440–10449.

(170) Rettenwander, D.; Redhammer, G.; Preishuber-Pflügl, F.; Cheng, L.; Miara, L.; Wagner, R.; Welzl, A.; Suard, E.; Doeff, M. M.; Wilkening, M.; *et al.* Structural and Electrochemical Consequences of Al and Ga Cosubstitution in $Li_7La_3Zr_2O_{12}$ Solid Electrolytes. *Chem. Mater.* **2016**, acs.chemmater.6b00579.

(171) Robertson, J. High Dielectric Constant Oxides. *Eur. Phys. J. Appl. Phys.* **2004**, *28*, 265–291.

(172) Miara, L. J.; Richards, W. D.; Wang, Y. E.; Ceder, G. First-Principles Studies on Cation Dopants and Electrolyte|cathode Interphases for Lithium Garnets. *Chem. Mater.* **2015**, *27*, 4040–4047.

(173) Wang, Y.; Lai, W. Phase Transition in Lithium Garnet Oxide Ionic Conductors $Li_7La_3Zr_2O_{12}$: The Role of Ta Substitution and H_2O/CO_2 Exposure. *J. Power Sources* **2015**, *275*, 612–620.

(174) Zhang, J.; Zhao, N.; Zhang, M.; Li, Y.; Chu, P. K.; Guo, X.; Di, Z.; Wang, X.; Li, H. Flexible and Ion-Conducting Membrane Electrolytes for Solid-State Lithium Batteries: Dispersion of Garnet Nanoparticles in Insulating Polyethylene Oxide. *Nano Energy* **2016**, *28*, 447–454.

(175) Pan, Q.; Smith, D. M.; Qi, H.; Wang, S.; Li, C. Y. Hybrid Electrolytes with Controlled Network Structures for Lithium Metal Batteries. *Adv. Mater.* **2015**, *27*, 5995–6001.

(176) Agrawal, A.; Choudhury, S.; Archer, L. A. A Highly Conductive, Non-Flammable Polymer–nanoparticle Hybrid Electrolyte. *RSC Adv.* **2015**, *5*, 20800–20809.

APPENDIX A

PERMISSIONS FROM ALL CO-AUTHORS

All co-authors have granted their permissions to use the copyrighted materials.

APPENDIX B

LIST OF PUBLICATIONS

Chapter II includes:

(1) Ting Yang, Ying Li and Candace K. Chan. "Enhanced Lithium Ion Conductivity in Lithium Lanthanum Titanate Solid Electrolyte Nanowires Prepared by Electrospinning" *Journal of Power Sources* **2015**, 287, 164-169

Chapter III includes:

(2) Ting Yang, Zachary D. Gordon, Ying Li and Candace K. Chan. "Nanostructured Garnet-Type Solid Electrolyte for Lithium Batteries: Electrospinning Synthesis of $Li_7La_3Zr_2O_{12}$ Nanowires and Particle Size-Dependent Phase Transformation" *The Journal of Physical Chemistry C* **2015**, 119, 14947-14953

Chapter IV includes:

(3) Ting Yang, Jin Zheng, Yan-Yan Hu, Qian Cheng and Candace K. Chan. "Composite Polymer Electrolytes with $Li_7La_3Zr_2O_{12}$ Garnet-Type Nanowires as Ceramic Fillers: Mechanism of Conductivity Enhancement and Role of Doping and Morphology" (Submitted)

Other publications generated during my graduate study:

(4) Ting Yang, Z. D. Gordon, and C. K. Chan. "Synthesis of Hyperbranched Perovskite Nanostructures" *Crystal Growth & Design* **2013**, 13, 3901-3907

(5) Q. Cheng, Ting Yang, M. Li and C. K. Chan. "Exfoliation of $LiNi_{1/3}Mn_{1/3}Co_{1/3}O_2$ into Nanosheets using Electrochemical Oxidation and Reassembly with Dialysis or Flocculation" *Langmuir* (Accepted)

(6) Zachary D. Gordon, Ting Yang, Guilherme Bruno Gomes Morgado and Candace K. Chan. "Preparation of Nano- and Microstructured Garnet $Li_7La_3Zr_2O_{12}$ Solid Electrolytes for Li-ion Batteries via Cellulose Templating". *ACS Sustainable Chemistry & Engineering* **2016**, 4, 6391-6398

(7) T. Grewe, Ting Yang, H. Tüysüz and C. K. Chan. "Hyperbranched Potassium Lanthanum Titanate Perovskite Photocatalysts for Hydrogen Generation" *Journal of Materials Chemistry A* **2016**, 4, 2837-2841

(8) Q. Cheng, Ting Yang, Y. Li, M. Li and C. K. Chan. "Oxidation-Reduction Assisted Exfoliation of $LiCoO_2$ into Nanosheets and Reassembly into Functional Li-ion Battery Cathodes" *Journal of Materials Chemistry A* **2016**, 4, 6902-6910

(9) R. Zhao, Ting Yang, M. A. Miller and C. K. Chan. "Electrochemical Properties of Nanostructured Copper Hydroxysulfate Mineral Brochantite upon Reaction with Lithium" *Nano Letters* **2013**, 13, 6055-606

(10) J. Wang, R. Krishna, Ting Yang and S. Deng. "Nitrogen-rich Microporous Carbons for Highly Selective Separation of Light Hydrocarbons" *Journal of Materials Chemistry A* **2016**, 4, 13957-13966

(11) J. Wang, J. Yang, R. Krishna, Ting Yang and S. Deng. "A Versatile Synthesis of Metal-Organic Framework-Derived Porous Carbons for CO_2 Capture and Gas Separation" *Journal of Materials Chemistry A* **2016**, 4, 19095-19106